Light in Strongly Scattering and Amplifying Random Media

Academisch Proefschrift

ter verkrijging van de graad van doctor
aan de Universiteit van Amsterdam,
op gezag van de Rector Magnificus
prof.dr P.W.M. de Meijer
ten overstaan van een door het
college van dekanen ingestelde commissie
in het openbaar te verdedigen
in de Aula der Universiteit
op dinsdag 21 november 1995 te 12:00 uur

door

Diederik Sybolt Wiersma

geboren te Utrecht

Promotor: prof. dr. A. Lagendijk
Copromotor: dr. M.P. van Albada

Overige leden commissie:
prof. dr. A. Aspect
prof. dr. D. Frenkel
prof. dr. K.J.F. Gaemers
prof. dr. J.F. v.d. Veen
prof. dr. J.T.M. Walraven

Faculteit der Wiskunde, Informatica, Natuurkunde en Sterrenkunde

The work described in this thesis is part of the research program
of the 'Stichting Fundamenteel Onderzoek van de Materie'
(Foundation for Fundamental Research on Matter)
and was made possible by financial support from the
'Nederlandse Organisatie voor Wetenschappelijk Onderzoek'
(Netherlands Organization for the Advancement of Research).
The research has been performed at the
FOM-Institute for Atomic and Molecular Physics
Kruislaan 407
1098 SJ Amsterdam
where a number of copies of this thesis is available.

Look, the sun was sleeping in the clouds this morning
up those mountains you can feel the glow
children playing in the valley, flying
in the winds they know that meet below
as their heart was beating fast this morning.

Contents

Chapter 1

Introduction

1.1 Light scattering

An object is visible because it scatters, reflects or absorbs light. In the first two cases an interaction takes place between light waves and matter in which the propagation direction of the waves is changed. In this interaction the light waves do not lose energy. Reflection is very similar to scattering: one can describe reflection as a special case of scattering in which incoming and outgoing angle are equal. Apart from being scattered, light can also be absorbed by an object. In that case, the object dissipates electromagnetic energy. An object that scatters equally efficient at all wavelengths and does not absorb, looks white. An object that absorbs strongly at all wavelengths, looks black. The color of an object can arise both from a wavelength-dependent scattering efficiency or a wavelength-dependent absorption.

1.1.1 Single scattering

The scattering properties of a single small particle (e.g. a water droplet), are complicated. An incoming ('applied') electromagnetic field on the particle induces in the particle an electric polarization. This polarization generates a new electromagnetic field in and around the particle. This new total electromagnetic field influences again the polarization of the particle, etc. The total outgoing electromagnetic field is the result of a complicated recursive process.

For particles which are very small compared to the wavelength of the light, the angular dependence of the scattered intensity is relatively simple. In this regime the light is scattered completely isotropically for a polarization perpendicular to the plane of scattering, and the scattered intensity

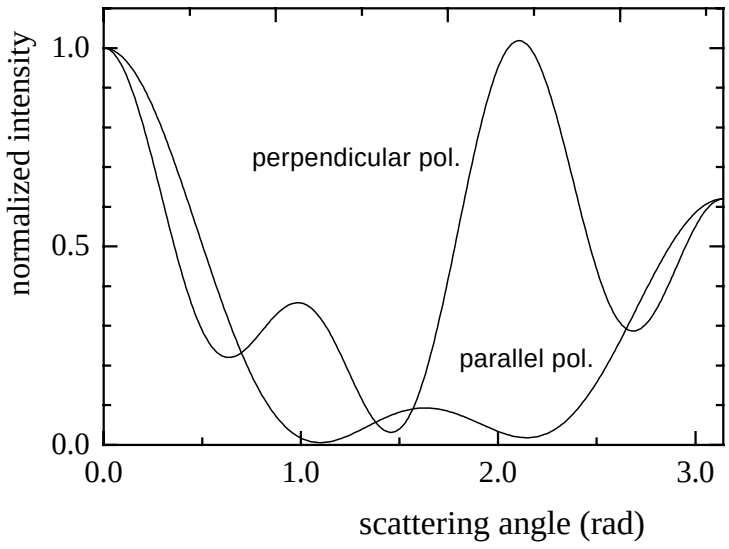

Figure 1.1: *Angular dependence of the scattered intensity, both for a polarization parallel and perpendicular to the plane of scattering, from a spherical particle (radius 199 nm, refractive index 2.8, wavelength 633 nm), calculated using Mie-theory [2,3]. The intensity for both polarizations is normalized to the scattered intensity at zero degree (forward scattering).*

has a squared cosine dependence on the scattering angle for a polarization in the plane of scattering, with zero intensity in the 90 degrees scattering direction. This is called Rayleigh scattering. For particles which have a diameter of the order of the wavelength, the angular dependence of the scattered intensity is quite complex, but can be calculated explicitly for spherical particles [1,2] (see Fig. 1.1).

The total flux which is scattered or absorbed by a particle is conveniently described by a scattering or absorption cross section. A cross section denotes a (virtual) area of the incoming beam at the position of the particle, through which the incoming flux is precisely equal to the specific flux of interest. For instance, the total scattered flux $F_s(\omega)$ is given by:

$$F_s(\omega) = \sigma_s(\omega)\, I_{in}(\omega), \tag{1.1}$$

where I_{in} is the incoming intensity and $\sigma_s(\omega)$ the scattering cross section,

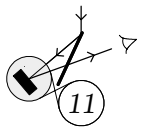

with ω the angular frequency of the light. Likewise, the absorption cross section $\sigma_{abs}(\omega)$ is defined as the area corresponding to the total absorbed flux. The extinction of a light beam is caused by both scattering and absorption. The extinction cross section is therefore defined as the sum of the absorption and scattering cross section:

$$\sigma_e(\omega) = \sigma_s(\omega) + \sigma_{abs}(\omega). \tag{1.2}$$

Generally, all cross sections depend on the frequency of the light.

For Rayleigh scattering, the total scattered flux decreases rapidly with increasing wavelength, that is, the scattering cross section is proportional to the fourth power of the frequency [2]:

$$\sigma_s = \frac{2}{3}\,\frac{\omega^4}{c_0^4}\,\frac{|\,\alpha\,|^2}{4\pi}, \tag{1.3}$$

with α the polarizability of the particle and c_0 the vacuum speed of light. This accounts for the fact that the sky is blue: the blue components of the sun light are scattered about five times more efficiently than the red components.

If light is scattered by a collection of particles, one can not simply add the scattered intensities from the individual particles. Even if a wave is scattered on average only once because the collection of particles is optically thin, co-operative effects can occur. The total scattered intensity is determined by the square of the absolute value of the total electric field:

$$I(t,\boldsymbol{r}) = \frac{c_0\,n}{2}\;|\,\mathbf{E}_1(t,\boldsymbol{r}) + \mathbf{E}_2(t,\boldsymbol{r}) + \mathbf{E}_3(t,\boldsymbol{r}) + \,\cdots|^2, \tag{1.4}$$

where $\mathbf{E}_i(t,\boldsymbol{r})$ are contributions to the total electric field from different scattering events. Here n is the effective refractive index of the total system. Because the summation is performed before taking the absolute value and the square, interference effects between the different fields are taken into account. An example of such an interference effect is the appearance of clouds in the sky when water vapor condenses [4]. Let us consider the scattering properties of one water droplet in a cloud. Apparently, a water droplet scatters light much more efficiently than the same amount of water vapor before it condenses. This can be explained as follows. If one brings N atoms together within a volume smaller than a cubic wavelength, the

scattered fields of these atoms will all be in phase. The resulting scattered intensity will therefore by N^2 and not N times the scattered intensity of one atom. This is an example of a *collective* effect of the scatterers (atoms) in the water droplet.

1.1.2 Multiple scattering

In the above example we considered the scattering by one water droplet. We call this single scattering. If we consider the scattering properties of an (optically thick) cloud, we are dealing with multiple light scattering. In this multiple scattering regime, light is often assumed to propagate diffusively. Interference effects are assumed to be scrambled, due to the many random scattering events, and the position and time-dependent intensity is described by a diffusion equation.

In some cases, interference in a disordered medium can not be neglected, even for very high orders of scattering. An example is the interference between waves that have propagated along the same path but in the opposite directions. Because these waves have travelled over exactly the same distance, their original phase relation is conserved, even if the path is formed by a very large number of scattering events. If the waves were originally in phase, they will interfere constructively when they meet again. This effect leads to for instance coherent backscattering, which is a general phenomenon for waves that are backscattered from a random medium. Due to constructive interference between waves that have propagated along the same path in the opposite direction, the backscattered intensity in the exact backscattering direction is twice as high as in other directions. Coherent backscattering is explained in detail in the next chapter. It is an example of an interference effect for light that is scattered (theoretically up to infinitely) many times.

An important concept in multiple scattering theory is the mean free path. A mean free path is a characteristic length scale describing the scattering process. For instance, the scattering mean free path is defined as the average distance between two successive scattering events. For a random distribution of small particles, any mean free path $\ell_\times$ can in principle be written in terms of a cross section $\sigma_\times$:

$$\ell_\times = \frac{1}{n\sigma_\times}, \tag{1.5}$$

with n the density of the scattering particles. For instance, the scattering mean free path ℓ_s is given by: $\ell_s = (n\sigma_s)^{-1}$.

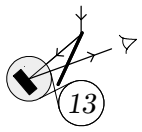

The transport mean free path ℓ_t is defined as the average distance the light travels in the sample before its propagation direction is randomized. For isotropic scattering, ℓ_t is equal to ℓ_s. For anisotropic scattering, the transport mean free path is given by:

$$\ell_t = \frac{1}{1 - \langle \cos\theta \rangle} \frac{1}{n\sigma_s}, \tag{1.6}$$

where $\langle \cos\theta \rangle$ is the average cosine of the scattering angle for each scattering event. The cross section corresponding to the transport mean free path is called the cross section for radiation pressure σ_t, which describes the average momentum transfer to the scatterer. So for the transport mean free path we can write: $\ell_t = (n\sigma_t)^{-1}$. Because the transport mean free path is often the relevant length scale to describe the propagation of light in disordered systems, we will drop the index t and just use ℓ to denote the transport mean free path.

The characteristic length scales relevant for absorption are the inelastic mean free path ℓ_i and the absorption mean free path ℓ_{abs}. The inelastic mean free path ℓ_i is defined as the travelled length over which the intensity is reduced by a factor e^{-1} due to absorption. The absorption mean free path ℓ_{abs} is defined as the (rms) average distance between begin and end points for paths of length ℓ_i:

$$\ell_{abs} = \sqrt{\tfrac{1}{3}\ell\ell_i}. \tag{1.7}$$

Any mean free path can generally be written as the reciprocal of a coefficient κ. Throughout this thesis a consistent notation will be used in which always: $\kappa_\times \equiv \ell_\times^{-1}$. For instance the extinction coefficient is given by $\kappa_e \equiv \ell_e^{-1}$, where $\ell_e = (n\sigma_e)^{-1}$.

1.1.3 Light versus electrons

There are interesting similarities between the propagation of light in a disordered dielectric and electrons in e.g. a disordered semiconductor or metal [5,6]. The stationary wave equation for the electric field is very similar to the stationary Schrödinger equation. The stationary Schrödinger equation reads:

$$\frac{\hbar^2}{2m}\nabla^2\psi(\boldsymbol{r}) + E\psi(\boldsymbol{r}) = V(\boldsymbol{r})\psi(\boldsymbol{r}), \tag{1.8}$$

for a stationary state with energy E for a particle of mass m in a potential $V(\boldsymbol{r})$. The stationary wave equation for one of the field components $\mathrm{E}(\boldsymbol{r})$ of the electric field can be written as (see also section 2.3):

$$-\nabla\times\nabla\times\mathrm{E}(\boldsymbol{r})+\frac{\omega^2}{c_0^2}\mathrm{E}(\boldsymbol{r})=V(\boldsymbol{r},\omega)\mathrm{E}(\boldsymbol{r}), \tag{1.9}$$

where the 'potential' for light is given by:

$$V(\boldsymbol{r},\omega)=-\frac{\omega^2}{c_0^2}\left[\epsilon(\boldsymbol{r})-1\right], \tag{1.10}$$

with $\epsilon(\boldsymbol{r})$ the (position-dependent) dielectric constant of the medium. For a collection of particles with constant refractive index in a homogeneous medium, $\epsilon(\boldsymbol{r})$ is constant both inside and outside the particles, and the double curl of $\mathrm{E}(\boldsymbol{r})$ can be replaced by $-\nabla^2\mathrm{E}(\boldsymbol{r})$. In the dynamical properties of light and electrons, important differences occur [7,8], which is however beyond the scope of this thesis.

Both for light and electrons in disordered systems, interference effects can occur. An example of such an interference effect for electrons is Anderson localization. For electrons in disordered (semi-)conductors, the diffusion is found to disappear completely if the electron scattering mean free path becomes smaller than some critical value [9,10]. This phenomenon can be described as an interference effect between counter propagating waves [10,11]. Due to constructive interference inside the sample between waves that have propagated along the same path in opposite directions, the return probability for these waves increases. If the scattering is strong enough, the diffusion disappears and the waves become localized. In this description of localization, recurrent scattering events are important [11,12]. These are events, in which a wave is scattered by a specific scatterer, scattered by at least one other scatterer, and then returns to this specific scatterer.

The parameter that describes the scattering strength is the scattering mean free path scaled by the wavelength λ of the light: $k\ell_s \equiv (2\pi/\lambda)\,\ell_s$. The transition to the localized regime occurs for:

$$k\ell_s \leq 1, \tag{1.11}$$

which is known as the Ioffe-Regel criterion [13]. Physically this criterion states that localization occurs if the scattering mean free path becomes

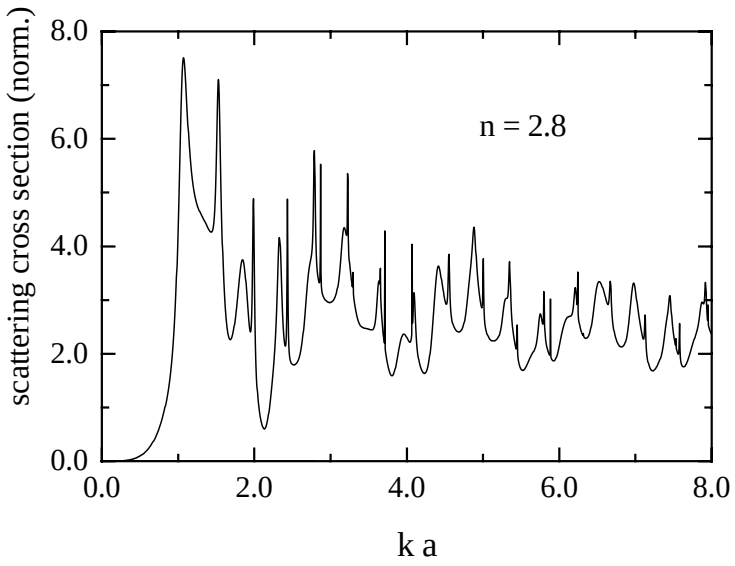

Figure 1.2: *Scattering cross section normalized to the geometrical cross section, for a sphere with refractive index $n = 2.8$, versus ka, where k is the wavenumber of the light and a is the diameter of the sphere. The calculation is performed using Mie-theory [2,3].*

comparable to the effective wavelength, so that a freely propagating wave can not even build up over one oscillation of the electric field.

The analogy between light and electrons, leads to the question whether a phenomenon similar to Anderson localization of electrons also exists for light waves [14]. So far, no experimental evidence for the optical counterpart of Anderson localization in three dimensions has been found. An important difference between light and electrons in the stationary case, lies in the frequency dependence of the potential. This ω^2 dependence of the potential leads in the Rayleigh scattering regime, i.e. in the limit $\omega \to 0$, to the ω^4 dependence of the scattering cross section [see Eq. (1.3)]. Consequently, the scattering mean free path increases with ω^{-4} at small frequencies ($k\ell_s$ becomes proportional to ω^{-3}), and the Ioffe-Regel criterion for light can not be fulfilled by simply lowering the frequency as it is possible for electrons. This is an important reason why Anderson localization of light is more difficult to achieve than Anderson localization of electrons.

For light, the strongest scattering (corresponding to the smallest values of $k\ell_s$) is obtained for wavelengths in the order of the diameter a of the

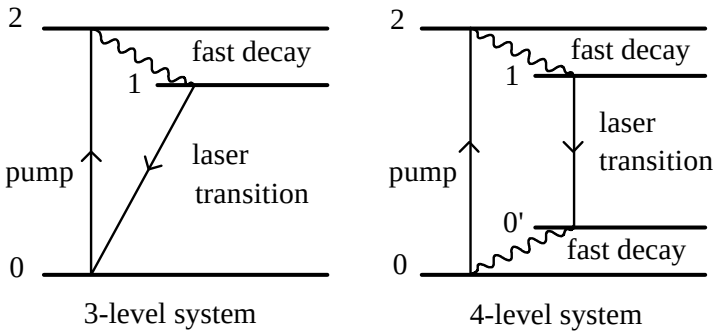

Figure 1.3: *Principle of a three and four level laser system*

scatterers. The (complex) single scattering properties of a particle in this regime are described by Mie-theory [1,2]. The wavelength dependence of the scattering cross section is complex, and shows resonances for certain values of ka (see Fig. 1.2). However, in going from red to blue in the visible spectrum, there is not such a strong overall trend as there is for Rayleigh scatterers. This explains why the sky becomes gray when it contains a lot of (relatively large) dust particles or fog.

1.2 Lasers

The field in optics in which scattering is usually avoided as much as possible, is the field of laser physics. The requirements for a laser contradict the presence of (multiple) scattering: the output of a laser should have a very high degree of unidirectionality, and the emission must be both spatially and temporally coherent.

Laser is an acronym for Light Amplification by Stimulated Emission of Radiation. Commonly the word laser is used to denote a laser oscillator. The essential elements of a laser oscillator are the following [15]: (a) a medium like a collection of atoms, molecules, or ions, or a semiconducting crystal, in which suitable optical transitions are possible, (b) an excitation or pumping mechanism, and (c) an optical feedback mechanism to allow the generated light to pass several times through the same region of the excited medium.

Most laser materials can be described as a three or four level system (see Fig. 1.3). The laser material is excited (either optically or electronically) from its ground state (0) to some excited state (2) with a very short

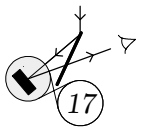

lifetime. Then the system falls rapidly back to some metastable state (1) with a lifetime ranging from a few nanoseconds to several milliseconds. The lifetime of this state is referred to as the excited state lifetime τ_e. In a three level system, the transition from this metastable state to the ground state is the laser transition. In a four level system, the laser transition is a transition from the metastable state to a state (0') which decays rapidly to the ground state (0).

The (optical) decay of the excited metastable state occurs either by spontaneous or by stimulated emission. In a spontaneous emission process, the radiated light is isotropic and its spectrum is determined by the broadening of the metastable and ground state. In a stimulated emission process, the decay is initiated by an incoming wave. In that case, the emitted light has the same wavelength, phase, and propagation direction as the incoming light. If the ground state is populated, the reversed process will also take place and the incoming light is absorbed. The dynamics of the system are described by a set of rate equations. For a three level system we have:

$$\frac{d\,N_0(\boldsymbol{r},t)}{dt} = -cN_0(\boldsymbol{r},t)[\sigma_{02}W_G(\boldsymbol{r},t) + \sigma_{01}W_R(\boldsymbol{r},t)] + \sigma_{10}cN_1(\boldsymbol{r},t)W_R(\boldsymbol{r},t) + \frac{1}{\tau_e}N_1(\boldsymbol{r},t), \tag{1.12}$$

and

$$\frac{d\,N_1(\boldsymbol{r},t)}{dt} = -\frac{d\,N_0(\boldsymbol{r},t)}{dt} \tag{1.13}$$

where c is the speed of light, N_1 and N_0 are the populations of respectively the metastable state and the ground state, σ_{02}, σ_{01}, and σ_{10} are the cross sections for respectively absorption at the pump wavelength [(0) $\rightarrow$ (2)], absorption at the emission wavelength [(0) $\rightarrow$ (1)] and stimulated emission [(1) $\rightarrow$ (0)]. Here $W_G(\boldsymbol{r},t)$ and $W_R(\boldsymbol{r},t)$ are the energy densities of respectively the pump light and the emitted light. The population of the third level can be neglected due to its very short lifetime. (All population transferred from (0) to (2) decays almost instantly to (1).) If the energy levels are equally degenerate, the absorption cross section for a transition equals the emission cross section: $\sigma_{10} = \sigma_{01}$ [16]. The amplification of light at the emission wavelength, is then determined by:

$$\frac{d\,W_R(\boldsymbol{r},t)}{dz} = (N_1 - N_0)\sigma_{01}W_R(\boldsymbol{r},t). \tag{1.14}$$

We see that to obtain amplification, the population in the metastable state must be larger than in the ground state. This situation is called inversion. To obtain this situation in a four level system is much easier, because the ground state (0') of the laser transition is nearly unpopulated.

To obtain a laser oscillator, one requires a feedback mechanism that allows the light to pass several times through the excited laser material. This is usually achieved with an optical cavity. In the simplest geometry, this cavity exists of two parallel mirrors, of which one is partially transmitting. The properties of the laser emission depend strongly on this cavity. Usually, the oscillator starts from (broad banded) spontaneous emission. Subsequently only those wavelengths that 'fit' in the cavity are amplified, that is, the wavelength must be equal to the cavity length divided by an integer. The spectral width of the emission is determined by the quality of the cavity and the gain, and can be extremely small. Naturally, also the direction of the laser output is determined by the cavity.

To obtain a high quality coherent laser oscillator, scattering is avoided as much as possible. The question arises, what would happen if one combines optical amplification with disorder. One could for instance study the emission from an excited laser material (not placed between cavity mirrors) in which one introduces a large amount of scattering. Due to the presence of relatively strong scattering, the residence time of light in the medium (and thereby the energy density of the light) increases, which will affect the spectral properties of the emission. Is it possible to obtain a laser oscillator as described above, in a medium in which the light is multiply scattered? In such a system, an optical feedback mechanism would be provided by random scattering. Also, it can be interesting to study the effect of gain on known multiple scattering interference phenomena like coherent backscattering. Due to the presence of gain, the contribution from long light paths will become more important. Also, due to the divergens of the intensity at infinite path lengths, the scattering properties of an amplifying random medium will depend critically on the sample geometry and size.

1.3 This thesis

In chapter 2 of this thesis, an introduction is given to multiple scattering theory for light. We will introduce diffusion theory for light in a disordered dielectric, and calculate explicitly the diffusion propagator for a slab geometry. Also we will explain the Green's function perturbation theory, commonly used to treat multiple light scattering. We will calculate explicitly coherent backscattering from a disordered slab in the diffusion ap-

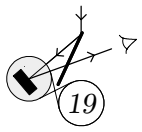

proximation. Throughout this thesis we will refer to the various concepts introduced in chapter 2.

In chapter 3, we will go into the experimental aspects of coherent backscattering. We will describe a new technique to record coherent backscattering cones and show some results in the weak scattering regime.

This technique is applied in chapter 4, to find experimental evidence for recurrent scattering of light in the strong scattering regime, close to where Anderson localization of light could be expected. Also we will present a calculation on the enhancement factor in coherent backscattering in the strong scattering regime, which supports the interpretation of our experimental results.

In chapter 5, we will go into the various aspects of the combination of optical amplification with multiple scattering. We will demonstrate how an amplifying random medium can be realized, and investigate the characteristics of the emission from such a medium from a theoretical point of view.

In chapter 6, we will describe scattering experiments from amplifying random media, of which coherent backscattering is of particular interest. Also a calculation is presented on coherent backscattering from amplifying disordered structures.

References and notes

[1] G. Mie, Ann. Physik **25**, 337 (1908).

[2] H.C. van de Hulst, *Light Scattering by Small Particles*, (Dover, New York, 1981).

[3] G.F. Bohren and D.R. Huffman, *Absorption and Scattering of Light by Small Particles* (Wiley, New York, 1983).

[4] R.P. Feynman, *Lectures on Physics* vol. 1, (Addison-Wesley, Menlo Park, California, 1977).

[5] *Analogies in Optics and Micro Electronics*, edited by W. van Haeringen and D. Lenstra (Kluwer, Dordrecht, 1990).

[6] P. Sheng, *Introduction to Wave Scattering, Localization, and Mesoscopic Phenomena* (Academic Press, San Diego, 1995).

[7] M.P. van Albada, B.A. van Tiggelen, A. Lagendijk, and A. Tip, Phys. Rev. Lett. **66**, 3132 (1991).

[8] A. Lagendijk and B.A. van Tiggelen, to be published in Physics reports (1995).

[9] P.W. Anderson, Phys. Rev. **109**, 1492 (1958); *Anderson Localization*, edited by T. Ando and H. Fukuyama, in *Springer proceedings in physics* **28** (Springer, Berlin, 1988).

[10] P.A. Lee and T.V. Ramakrishnan, Rev. of Modern Phys. **57**, 287 (1985).

[11] B.L. Altshuler, A.G. Aronov, D.E. Khmel'nitskii, and A.I. Larkin, in *Quantum Theory of Solids*, edited by I.M. Lifshits (MIR Publishers, Moskva, 1983).

[12] D. Vollhardt and P. Wölfle, in *Electronic Phase Transitions*, *Modern Problems in Condensed Matter Sciences* **32**, edited by W. Hanke and Yu. V. Kopaev (North-Holland, Amsterdam, 1992).

[13] A.F. Ioffe and A.R. Regel, Progr. Semiconductors **4**, 237 (1960); N.F. Mott, *Metal-Insulator Transitions* (Taylor and Francis, London, 1974).

[14] *Scattering and Localization of Classical Waves in Random Media* in *World Scientific Series on Directions in Condensed Matter Physics* **8**, edited by P. Sheng (World Scientific, Singapore, 1990).

[15] A.E. Siegman, *Lasers* (University Science Books, Mill Valley, California, 1986).

[16] Usually the three or four levels picture used to describe a laser material is a simplification of a much more complicated system consisting of many energy levels. In that case it not generally true that the emission and absorption cross sections are equal.

Chapter 2

Multiple scattering theory

2.1 Introduction

The propagation of light in a any medium is generally described by Maxwell's equations for the electric and magnetic field. To calculate the electric field in a disordered dielectric like white paint or a colloidal suspension, one is faced with solving a wave equation with a randomly varying refractive index. In section 2.3, it will be shown how Green's function theory is often used to treat this problem. A Green's function $G(\boldsymbol{r}_1, \boldsymbol{r}_2)$ that describes the propagation of the electric field in a random medium is introduced, as well as the four point vertex $\Gamma(\boldsymbol{r}_1, \boldsymbol{r}_2; \boldsymbol{r}_3, \boldsymbol{r}_4)$ that describes the propagation of the intensity. These concepts are introduced without going into great detail. For a thorough treatment of multiple light scattering we refer to the literature on this subject [1–4]. In section 2.4, it will be shown how the backscattered intensity from a disordered medium can be calculated explicitly in the diffusion approximation. Because the diffusion approximation forms an important concept in multiple scattering theory, we start with introducing the diffusion equation for light in disordered media.

2.2 Diffusion of light

In the diffusion approximation, the propagation of the intensity is described as a random walk with a characteristic mean free path ℓ. Only the intensity and not the electric field itself is considered, so the wave character of the light is not taken into account. Usually also the vector nature of light is disregarded. In reality, there are two polarization channels over which the light is distributed in the scattering process. In chapter 3 we will show that

good agreement is found between scalar diffusion theory and experimental data for light backscattered from a disordered sample. In the diffusion approximation, the intensity $I(\boldsymbol{r},t)$ is determined by a diffusion equation:

$$\frac{\partial I(\boldsymbol{r},t)}{\partial t} = D\nabla^2 I(\boldsymbol{r},t) - \frac{v}{\ell_i} I(\boldsymbol{r},t), \tag{2.1}$$

where D is the diffusion constant given by $D = \frac{1}{3}\ell v$ with ℓ the transport mean free path, v is the transport velocity for the light inside the medium, and ℓ_i is the inelastic mean free path.

2.2.1 Stationary solution for a slab

Most of the samples that are studied experimentally have a slab geometry. In the this subsection, the stationary solution to the diffusion equation is calculated for such a slab geometry. Starting point is Eq. (2.1). In the stationary case, the time derivative on the left hand side is zero. We can account for an incoming intensity by adding a source function $S(\boldsymbol{r})$ on the right hand side. This yields:

$$0 = \tfrac{1}{3}\ell^2\nabla^2 I(\boldsymbol{r}) - \ell\kappa_i I(\boldsymbol{r}) + S(\boldsymbol{r}), \tag{2.2}$$

Defining the intensity propagator $F(\boldsymbol{r}_1,\boldsymbol{r}_2)$ as the solution of:

$$\tfrac{1}{3}\ell^2\,\nabla^2 F(\boldsymbol{r}_1,\boldsymbol{r}_2) - \ell\kappa_i\, F(\boldsymbol{r}_1,\boldsymbol{r}_2) = -\delta(\boldsymbol{r}_1-\boldsymbol{r}_2), \tag{2.3}$$

one can write the intensity as:

$$I(\boldsymbol{r}_1) = \int d\boldsymbol{r}_2\, F(\boldsymbol{r}_1,\boldsymbol{r}_2) S(\boldsymbol{r}_2), \tag{2.4}$$

where the integral is taken over the volume of the scattering medium. The intensity propagator $F(\boldsymbol{r}_1,\boldsymbol{r}_2)$ describes the propagation of the intensity in a disordered slab in the diffusion approximation. By introducing $F(\boldsymbol{r}_1,\boldsymbol{r}_2)$, the problem of solving the stationary diffusion equation has been reduced to finding the solution of Eq. (2.3), which is independent of $S(\boldsymbol{r})$.

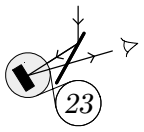

It is convenient to choose the orientation of the slab such that its interface is perpendicular to the z-axis. Then the system is translationally invariant over x and y, and one can use the Fourier transform:

$$F(\boldsymbol{q}_\perp, z_1, z_2) = \int d\boldsymbol{r}_\perp F(\boldsymbol{r}_1, \boldsymbol{r}_2) e^{i\boldsymbol{r}_\perp \cdot \boldsymbol{q}_\perp}, \tag{2.5}$$

where $\boldsymbol{r}_\perp = \boldsymbol{r}_{1\perp} - \boldsymbol{r}_{2\perp}$ is perpendicular to z. After Fourier transforming Eq. (2.3), one obtains:

$$\tfrac{1}{3}\ell^2 \left(\frac{\partial^2}{\partial z_1^2} - q_\perp^2 \right) F(\boldsymbol{q}_\perp, z_1, z_2) - \ell \kappa_i F(\boldsymbol{q}_\perp, z_1, z_2) = -\delta(z_1 - z_2). \tag{2.6}$$

From radiative transfer theory [5], it is known that the diffuse intensity at the front and rear interface ($z = 0$ and $z = L$) of the sample is not zero, but that the appropriate boundary condition for a slab is found by taking the intensity zero at a distance z_0 from the interface. The value of z_0 depends on the refractive index contrast between the sample and its surrounding medium [6]. For an index matched sample interface its value is: $z_0 \approx 0.7104\,\ell$ [5]. Solving Eq. (2.6) with this boundary condition one finds:

$$F(\boldsymbol{q}_\perp, z_1, z_2) = F(\boldsymbol{q}_\perp, z_s, z_d) = \frac{3\cosh[\alpha(L - z_s)] - 3\cosh[\alpha(L + 2z_0 - |z_d|)]}{2\ell^2\,\alpha \sinh[\alpha(L + 2z_0)]}, \tag{2.7}$$

where $z_s \equiv z_1 + z_2$, $z_d \equiv z_1 - z_2$, L is the slab thickness, and $\alpha \equiv \sqrt{\ell_{abs}^{-2} + q_\perp^2}$ with ℓ_{abs} the absorption length in the medium. One can identify $\boldsymbol{q}_\perp$ with $\boldsymbol{k}_{1\perp} + \boldsymbol{k}_{2\perp}$, where $\boldsymbol{k}_{2\perp}$ and $\boldsymbol{k}_{1\perp}$ are the perpendicular components of respectively the incoming and outgoing wavevector. With the intensity propagator $F(\boldsymbol{q}_\perp, z_1, z_2)$, one can calculate the diffuse intensity in a disordered slab from any source $S(\boldsymbol{r})$. For an incoming plane wave from $z = -\infty$, the source function is $S(z) = S_0 \exp(-z\kappa_e)$, where κ_e is the extinction rate given by $\kappa_e \equiv \ell_e^{-1} = \ell_s^{-1} + \ell_i^{-1}$. In section 2.4, we will show how one can use the intensity propagator $F(\boldsymbol{r}_1, \boldsymbol{r}_2)$ to calculate coherent backscattering in the diffusion approximation.

2.3 Multiple scattering of waves

In this section, the formalism is introduced which is commonly used to describe multiple scattering of light waves. Starting point is the set of Maxwell's equations for the electric and magnetic field. Green's function theory is used to derive perturbation expansions both for the electric field and the intensity. Also the (Feynman) diagrams are introduced that can be used to simplify the notation for the electric field and the intensity.

2.3.1 Electric field

Starting from Maxwell's equations, the electric field can be shown to fulfill the time-dependent wave equation [7]:

$$\nabla^2 \mathbf{E}(\boldsymbol{r},t) + \boldsymbol{\nabla} \frac{\mathbf{E}(\boldsymbol{r},t) \cdot \boldsymbol{\nabla}\epsilon(\boldsymbol{r})}{\epsilon(\boldsymbol{r})} - \frac{\epsilon(\boldsymbol{r})}{c_0^2} \frac{\partial^2 \mathbf{E}(\boldsymbol{r},t)}{\partial t^2} = 0. \tag{2.8}$$

The second term in this equation, containing the gradient of $\epsilon(\boldsymbol{r})$, is zero in regions of space where $\epsilon(\boldsymbol{r})$ is constant. We will regard a collection of particles with a constant refractive index in a surrounding medium with another constant refractive index, so $\epsilon(\boldsymbol{r})$ is constant inside and outside the particles. In that case, the second term in Eq. (2.8) determines the boundary condition for the electric field at the particle boundary, and is zero elsewhere. By using a Fourier transformation with respect to time, the explicit time dependence in Eq. (2.8) can be removed, and all harmonics of the resulting Fourier representation will follow the time-independent Helmholtz equation:

$$\nabla^2 E(\boldsymbol{r}) + (\omega/c_0)^2 \epsilon(\boldsymbol{r}) E(\boldsymbol{r}) = 0, \tag{2.9}$$

where $E(\boldsymbol{r})$ denotes one of the field components of the electric field, inside or outside the scatterers. The same equation holds for the magnetic field components. Here $\epsilon(\boldsymbol{r})$ is the (random) place-dependent dielectric constant of the system, ω the frequency of the electric field, and c_0 the vacuum speed of light. The wave equation can be written as:

$$\nabla^2 E(\boldsymbol{r}) + (\omega/c_0)^2 E(\boldsymbol{r}) = V(\boldsymbol{r}) E(\boldsymbol{r}), \tag{2.10}$$

where $V(\boldsymbol{r})$ is the scattering potential defined as $V(\boldsymbol{r}) \equiv -(\omega/c_0)^2 [\epsilon(\boldsymbol{r}) - 1]$. For a collection of point like scatterers with polarizability α_0, in

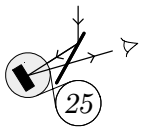

a surrounding medium with dielectric constant 1, the scattering potential is given by:

$$V(\boldsymbol{r}) = -\alpha_0(\omega/c_0)^2 \sum_i \delta(\boldsymbol{r} - \boldsymbol{r}_i), \tag{2.11}$$

with $\boldsymbol{r}_i$ the positions of the scatterers. For a point like scatterer with dielectric constant ϵ_1 and radius a in vacuum, the polarizability is given by $\alpha_0 = a^3(\epsilon_1 - 1)/(\epsilon_1 + 2)$. Introducing the Green's function $G_0(\boldsymbol{r}_1, \boldsymbol{r}_2)$ as the solution of:

$$\nabla^2 G_0(\boldsymbol{r}_1, \boldsymbol{r}_2) + (\omega/c_0)^2 G_0(\boldsymbol{r}_1, \boldsymbol{r}_2) = -\delta(\boldsymbol{r}_1 - \boldsymbol{r}_2), \tag{2.12}$$

one can write the solution to Eq. (2.10) formally as:

$$E(\boldsymbol{r}_1) = E_{in}(\boldsymbol{r}_1) - \int d\boldsymbol{r}_2\, G_0(\boldsymbol{r}_1, \boldsymbol{r}_2) V(\boldsymbol{r}_2) E(\boldsymbol{r}_2), \tag{2.13}$$

where $E_{in}(\boldsymbol{r}_1)$ is a solution of the homogeneous wave equation obtained by taking $V(\boldsymbol{r}) = 0$ in Eq. (2.10). $E_{in}(\boldsymbol{r}_1)$ represents the incoming coherent wave. $G_0(\boldsymbol{r}_1, \boldsymbol{r}_2)$ is also referred to as the bare Green's function and describes the propagation of the field in a medium without scatterers. It is given by:

$$G_0(\boldsymbol{r}_1, \boldsymbol{r}_2) = \frac{e^{-ik\,|\boldsymbol{r}_1 - \boldsymbol{r}_2\,|}}{4\pi\,|\boldsymbol{r}_1 - \boldsymbol{r}_2\,|}, \tag{2.14}$$

with $k = \omega/c_0$. By iterating the recursion relation Eq. (2.13), one obtains the following perturbation series for the electric field:

$$\begin{aligned} E(\boldsymbol{r}_1) = E_{in}(\boldsymbol{r}_1) &- \int d\boldsymbol{r}_2\; G_0(\boldsymbol{r}_1, \boldsymbol{r}_2) V(\boldsymbol{r}_2) E_{in}(\boldsymbol{r}_2) \\ &+ \iint d\boldsymbol{r}_2 d\boldsymbol{r}_3\; G_0(\boldsymbol{r}_1, \boldsymbol{r}_2) V(\boldsymbol{r}_2) G_0(\boldsymbol{r}_2, \boldsymbol{r}_3) V(\boldsymbol{r}_3) E_{in}(\boldsymbol{r}_3) \\ &- \iiint d\boldsymbol{r}_2 \,..\, d\boldsymbol{r}_4\, G_0(\boldsymbol{r}_1, \boldsymbol{r}_2) V(\boldsymbol{r}_2) G_0(\boldsymbol{r}_2, \boldsymbol{r}_3) V(\boldsymbol{r}_3) G_0(\boldsymbol{r}_3, \boldsymbol{r}_4) V(\boldsymbol{r}_4) E_{in}(\boldsymbol{r}_4) + \cdots, \end{aligned} \tag{2.15}$$

where all integrals are taken over the volume of the sample. The above expression depends on E_{in}. To describe the propagation of the field in the

medium independently of E_{in}, we use the total Green's function $G(\boldsymbol{r}_1, \boldsymbol{r}_2)$ which is defined as the solution of:

$$\nabla^2 G(\boldsymbol{r}_1, \boldsymbol{r}_2) + (\omega/c_0)^2 \epsilon(\boldsymbol{r}) G(\boldsymbol{r}_1, \boldsymbol{r}_2) = -\delta(\boldsymbol{r}_1 - \boldsymbol{r}_2). \tag{2.16}$$

The Green's function $G(\boldsymbol{r}_1, \boldsymbol{r}_2)$ describes the field at any point $\boldsymbol{r}_1$ in the medium, due to a source at $\boldsymbol{r}_2$. The perturbation series for $G(\boldsymbol{r}_1, \boldsymbol{r}_2)$ is:

$$\begin{aligned} G(\boldsymbol{r}_1, \boldsymbol{r}_2) = G_0(\boldsymbol{r}_1, \boldsymbol{r}_2) - \int d\boldsymbol{r}_a G_0(\boldsymbol{r}_1, \boldsymbol{r}_a) V(\boldsymbol{r}_a) G_0(\boldsymbol{r}_a, \boldsymbol{r}_2) \\ + \iint d\boldsymbol{r}_a d\boldsymbol{r}_b G_0(\boldsymbol{r}_1, \boldsymbol{r}_a) V(\boldsymbol{r}_a) G_0(\boldsymbol{r}_a, \boldsymbol{r}_b) V(\boldsymbol{r}_b) G_0(\boldsymbol{r}_b, \boldsymbol{r}_2) - \cdots\cdots. \end{aligned} \tag{2.17}$$

Note that $V(\boldsymbol{r})$ (given by Eq. (2.11)) contains contributions from all scatterers. The first terms of Eq. (2.18) describes propagation without scattering, the second term equals the sum of all single scattering contributions, the third term the sum of all double scattering contributions, id. To simplify the notation one can use (Feynman) diagrams. The diagrammatic representation of the above series is:

$G =$

(2.18)

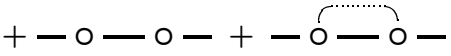

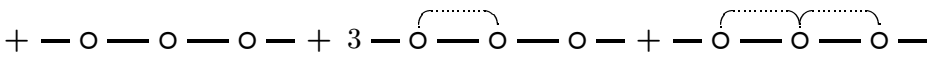

Lines represent the bare Green's function $G_0(\boldsymbol{r}_1, \boldsymbol{r}_2)$, and circles represent the scattering potential of an individual scatterer: $-\alpha_0(\omega/c_0)^2\delta(\boldsymbol{r} - \boldsymbol{r}_i)$. Dashed lines connect identical scatterers. For clarity, terms are organized in such a way, that every row in Eq. (2.18) corresponds to the same order of scattering. The drawing convention used in this thesis is summarized in

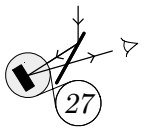

appendix B. The above series can be simplified by introducing the single particle t-matrix $t(\boldsymbol{r}_1, \boldsymbol{r}_2; \omega)$ (diagrammatic representation: $\times$), defined as the sum of all repeated scattering from one scatterer:

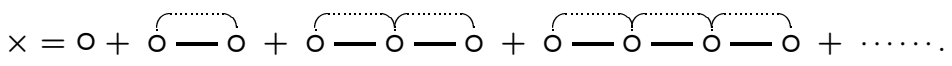

The total Green's function of the system then reads:

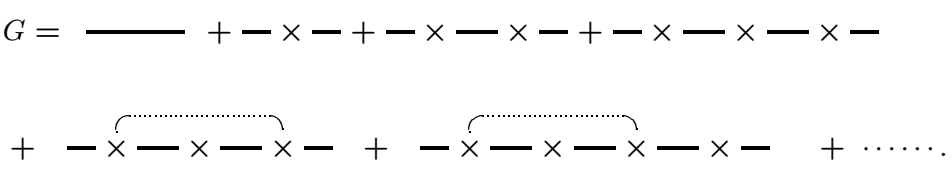

(2.19)

The perturbation series for the t-matrix is called the Born series. The physical interpretation of this series is that the incoming field induces an electric polarization (first term). This polarization changes the field around the scatterer, which influences again the polarization (second terms), etc. The t-matrix for a point scatterer located at $\boldsymbol{r}_i$ is to first order: $t(\boldsymbol{r}_1, \boldsymbol{r}_2; \omega) = -\alpha_0(\omega/c_0)^2 \delta(\boldsymbol{r}_2 - \boldsymbol{r}_i)\delta(\boldsymbol{r}_1 - \boldsymbol{r}_i)$. Real physical scatterers have a finite size. If their diameter is of the order of the wavelength or larger, they have resonances which are not taken into account in the first order Born approximation. If we want to incorporate these resonances and still use point scatterers, we need higher order terms of the Born series. Unfortunately, to higher order the Born series diverges due to the divergence of $G_0(\boldsymbol{r}_1, \boldsymbol{r}_2)$ for $\boldsymbol{r}_1 = \boldsymbol{r}_2$. The problem can be solved by introducing a cut-off length a for $\boldsymbol{r}_1 - \boldsymbol{r}_2$ of the order of the size of the real physical scatterers. Then the Born series converges and one finds the t-matrix [8]:

$$t(\boldsymbol{r}_1, \boldsymbol{r}_2; \omega) = t(\omega)\delta(\boldsymbol{r}_2 - \boldsymbol{r}_i)\delta(\boldsymbol{r}_1 - \boldsymbol{r}_i), \tag{2.20}$$

with

$$t(\omega) = -\frac{\alpha_0(\omega/c_0)^2}{1 - \omega^2/\omega_0^2 - i\alpha_0(\omega/c_0)^3}. \tag{2.21}$$

This t-matrix has one resonance, namely for $\omega = \omega_0 \equiv c_0\sqrt{a/\alpha_0}$. The local

electric polarization $P(\omega, \boldsymbol{r})$ induced by the total electric field is given by:

$$P(\omega, \boldsymbol{r}) = [\epsilon(\boldsymbol{r}) - 1]E(\omega, \boldsymbol{r}). \tag{2.22}$$

Using the definition of the t-matrix, one can write this polarization (for a system of one scatterer) in terms of the incoming field $E_{in}(\omega, \boldsymbol{r})$ as:

$$P(\omega, \boldsymbol{r}) = -\frac{c_0^2}{\omega^2} V(\omega, \boldsymbol{r}) E(\omega, \boldsymbol{r}) = -\frac{c_0^2}{\omega^2}\, t(\omega) E_{in}(\omega, \boldsymbol{r}). \tag{2.23}$$

This means that the t-matrix can be written as a polarizability $\alpha(\omega)$ of the scatterer, induced by the incoming field $E_{in}(\omega, \boldsymbol{r})$:

$$\alpha(\omega) = -\frac{c_0^2}{\omega^2}\, t(\omega)\,. \tag{2.24}$$

The scattering cross section and extinction cross section in terms of the t-matrix are given by: $\sigma_s = (4\pi)^{-1}|t(\omega)|^2$ and $\sigma_e = -(c_0/\omega)\,\mathrm{Im}[t(\omega)]$. For non absorbing particles the extinction cross section is equal to the scattering cross section, which yields the following condition for the t-matrix:

$$\frac{1}{4\pi}\, |t(\omega)|^2 = -\frac{c_0}{\omega}\, \mathrm{Im}[t(\omega)]. \tag{2.25}$$

The above relation is known as the optical theorem.

The terms in the perturbation series of Eq. (2.19) with dashed lines connecting identical scatterers, are called recurrent scattering events. These are events in which a wave is scattered by a specific scatterer, scattered by at least one other scatterer and then returns to this specific scatterer. For relatively weak scattering, recurrent scattering events can be neglected. This approximation is called the 'self-avoiding multiple scattering approximation' (SAMS). In chapter 4 we will discuss the breakdown of this approximation at very strong scattering. There we will show how recurrent events can influence the backscattered intensity from a strongly scattering sample.

The total Green's function $G(\boldsymbol{r}_1, \boldsymbol{r}_2)$ depends on the positions of the scatterers. A useful quantity is the averaged or 'dressed' Green's function $G(\boldsymbol{r}_1 – \boldsymbol{r}_2)$, which is obtained by averaging $G(\boldsymbol{r}_1, \boldsymbol{r}_2)$ over the positions of the

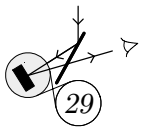

scatterers. In the SAMS approximation $G(\boldsymbol{r}_1 - \boldsymbol{r}_2)$ can be calculated from Eq. (2.19), by Fourier transforming to momentum space. In momentum space the summation can be performed and after transforming back to real space one finds:

$$G(\boldsymbol{r}_1 - \boldsymbol{r}_2) \equiv \langle G(\boldsymbol{r}_1, \boldsymbol{r}_2) \rangle = \frac{e^{-iK\ |\boldsymbol{r}_1 - \boldsymbol{r}_2|}}{4\pi\ |\boldsymbol{r}_1 - \boldsymbol{r}_2|}, \tag{2.26}$$

where $K = \sqrt{(\omega/c_0)^2 + nt}$ is the (complex) effective k-vector for the light inside the sample, with n the density of scatterers.

2.3.2 Intensity

The intensity is defined as the energy that crosses a unit area per unit of time. It is given by the magnitude of the cycle average of the Poynting vector $\mathbf{E} \times \mathbf{B}$, which can be written as:

$$I(\boldsymbol{r}) = \frac{c_0\, n}{2}\ |\,\mathbf{E}(\boldsymbol{r})\,|^2, \tag{2.27}$$

with c_0 the vacuum speed of light, and n the refractive index of the medium. In terms of the total Green's function $G(\boldsymbol{r}_1, \boldsymbol{r}_2)$, the intensity is given by:

$$I(\boldsymbol{r}) \equiv \frac{c_0\, n}{2}\, E(\boldsymbol{r}) E^*(\boldsymbol{r}) = \frac{c_0\, n}{2} \iint d\boldsymbol{r}_1 d\boldsymbol{r}_2 G(\boldsymbol{r}\,, \boldsymbol{r}_1) G^*(\boldsymbol{r}\,, \boldsymbol{r}_2) E_{in}(\boldsymbol{r}_1) E^*_{in}(\boldsymbol{r}_2), \tag{2.28}$$

where $G(\boldsymbol{r}_1, \boldsymbol{r}_2)$ is the unaveraged Green's function given by Eq. (2.19). The product $G\,G^*$ describes the intensity at any point in the system due to the product of incoming waves $E_{in} E^*_{in}$. The diagrammatic expansion of $G\,G^*$ is:

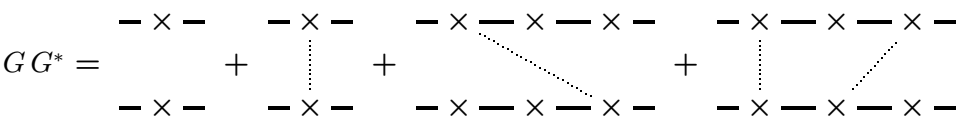

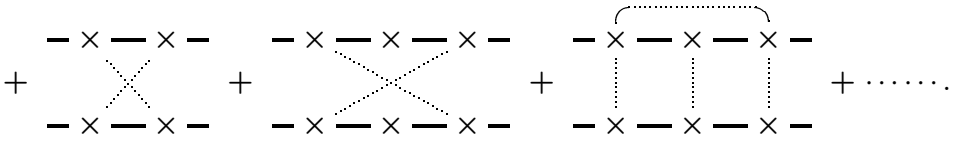

(2.29)

The upper line corresponds to $G(\boldsymbol{r}_1, \boldsymbol{r}_2)$ and the lower line to the complex conjugate $G^*(\boldsymbol{r}_3, \boldsymbol{r}_4)$. Dashed lines again connect identical scatterers. The six terms given in Eq. (2.29) are only some examples of the various terms contributing to $G\,G^*$.

An important simplification is obtained if $G\,G^*$ is averaged over the positions of the scatterers. Then the bare Green's functions together with all t-matrices not connected by dashed lines, can be replaced by the dressed Green's function. This yields:

$\langle G\,G^* \rangle =$ (2.30)

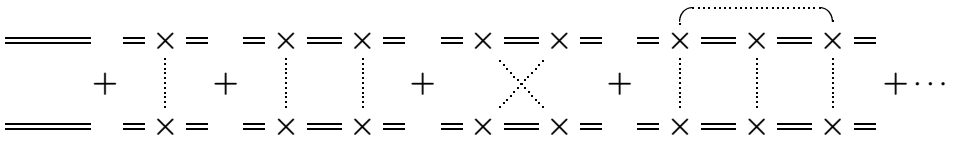

where double lines represent the dressed Green's function $G(\boldsymbol{r}_1 - \boldsymbol{r}_2)$.

Usually, $\langle G\,G^* \rangle$ is stripped from its incoming and outgoing Green's functions. This yields the total vertex $\Gamma(\boldsymbol{r}_1, \boldsymbol{r}_2; \boldsymbol{r}_3, \boldsymbol{r}_4)$ defined by:

$$\begin{aligned} \langle G(\boldsymbol{r}_1, \boldsymbol{r}_2) G^*(\boldsymbol{r}_3, \boldsymbol{r}_4) \rangle &= G(\boldsymbol{r}_1 - \boldsymbol{r}_2) G^*(\boldsymbol{r}_3 - \boldsymbol{r}_4) \\ &+ G(\boldsymbol{r}_1 - \boldsymbol{r}_5) G^*(\boldsymbol{r}_3 - \boldsymbol{r}_7) \langle \Gamma(\boldsymbol{r}_5, \boldsymbol{r}_6; \boldsymbol{r}_7, \boldsymbol{r}_8) \rangle G(\boldsymbol{r}_6 - \boldsymbol{r}_2) G^*(\boldsymbol{r}_8 - \boldsymbol{r}_4), \end{aligned} \tag{2.31}$$

where an integration is performed over repeated spatial coordinates. The perturbation series for $\Gamma(\boldsymbol{r}_1, \boldsymbol{r}_2; \boldsymbol{r}_3, \boldsymbol{r}_4)$ is given by:

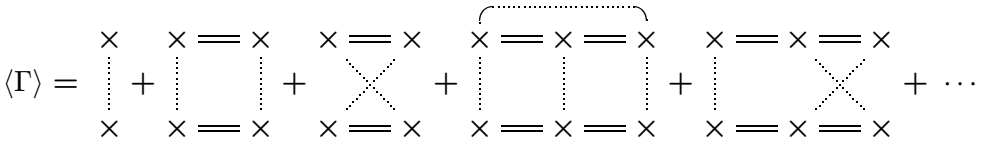

(2.32)

In the SAMS approximation recurrent scattering events like the fourth term in Eq. (2.32) are neglected.

The total vertex $\Gamma(\boldsymbol{r}_1, \boldsymbol{r}_2; \boldsymbol{r}_3, \boldsymbol{r}_4)$ can be decomposed into the set of reducible diagrams $R(\boldsymbol{r}_1, \boldsymbol{r}_2; \boldsymbol{r}_3, \boldsymbol{r}_4)$ and the set of irreducible diagrams $U(\boldsymbol{r}_1, \boldsymbol{r}_2; \boldsymbol{r}_3, \boldsymbol{r}_4)$. A diagram is irreducible if it can not be split in two separate diagrams without breaking a dashed line. The following recursion relation holds for the total vertex in terms of the irreducible vertex:

$$\begin{aligned}\langle\Gamma(\boldsymbol{r}_1, \boldsymbol{r}_2; \boldsymbol{r}_3, \boldsymbol{r}_4)\rangle &= \langle U(\boldsymbol{r}_1, \boldsymbol{r}_2; \boldsymbol{r}_3, \boldsymbol{r}_4)\rangle \\ &+ \langle U(\boldsymbol{r}_1, \boldsymbol{r}_5; \boldsymbol{r}_3, \boldsymbol{r}_6)\rangle G(\boldsymbol{r}_5 - \boldsymbol{r}_7) G^*(\boldsymbol{r}_6 - \boldsymbol{r}_8) \langle\Gamma(\boldsymbol{r}_7, \boldsymbol{r}_2; \boldsymbol{r}_8, \boldsymbol{r}_4)\rangle.\end{aligned} \tag{2.33}$$

All reducible diagrams in Γ can be found by iterating this recursion relation, starting from the zeroth order solution $\Gamma = U$.

2.4 Backscattered intensity

In this section, the backscattered intensity from a disordered medium is calculated explicitly in the SAMS approximation. The backscattered intensity is usually described in terms of a bistatic coefficient γ defined as the observed scattered flux per solid angle and per unit of observed area of the sample at normalized incident flux. In terms of the average scattered intensity $\langle I(\boldsymbol{r})\rangle$ and incident intensity I_0, the bistatic coefficient can be written as:

$$\gamma = \frac{4\pi r^2}{A} \frac{\langle I(\boldsymbol{r})\rangle}{I_0}, \tag{2.34}$$

with A the observed area of the sample and r the distance from observer to sample. Starting from the general expression Eq. (2.28) for the intensity

and after averaging over the positions of the scatterers using the definition of the total vertex, one obtains for the scattered intensity:

$$\langle I(\boldsymbol{r})\rangle = \frac{c_0\, n}{2}\int d\boldsymbol{r}_1..d\boldsymbol{r}_4\, G(\boldsymbol{r}-\boldsymbol{r}_1)G^*(\boldsymbol{r}-\boldsymbol{r}_3)\langle\Gamma(\boldsymbol{r}_1,\boldsymbol{r}_2;\boldsymbol{r}_3,\boldsymbol{r}_4)\rangle\langle E_{in}(\boldsymbol{r}_2)E^*_{in}(\boldsymbol{r}_4)\rangle. \tag{2.35}$$

The dressed Green's function $G(\boldsymbol{r}-\boldsymbol{r}_1)$ and the complex conjugate $G^*(\boldsymbol{r}-\boldsymbol{r}_3)$ describe the propagation of the scattered intensity towards the point of observation and are given by Eq. (2.26). For backscattering, $G(\boldsymbol{r}-\boldsymbol{r}_1)$ can be approximated by:

$$G(\boldsymbol{r}-\boldsymbol{r}_1) \simeq -\frac{e^{ikr}}{4\pi r}e^{-i\boldsymbol{k}_s\cdot\boldsymbol{r}_1 - \frac{1}{2}\kappa_e z_1\mu_s^{-1}}, \tag{2.36}$$

with $\boldsymbol{r}_1$ inside the slab and $\boldsymbol{r}$ far outside the slab, where we have used that:

$$iK\,|\boldsymbol{r}-\boldsymbol{r}_1| \approx iK\left(r - \frac{\boldsymbol{r}\cdot\boldsymbol{r}_1}{r}\right) \approx ikr - i\mathbf{K}\cdot\boldsymbol{r}_1, \tag{2.37}$$

with $\mathbf{K} = \boldsymbol{k}_s + \frac{1}{2}i\kappa_e\mu_s^{-1}\hat{\boldsymbol{z}}$. Here $k = \omega/c_0$, $\boldsymbol{k}_s$ is the outgoing wavevector, κ_e is the extinction coefficient, and $\mu_s = \cos\theta$, with θ the angle between $\boldsymbol{k}_s$ and $\hat{z}$. For the incoming wave $E_{in}(\boldsymbol{r}\,)$ we take a normalized plane wave perpendicular to the sample surface, which is damped inside the sample by κ_e:

$$E_{in}(\boldsymbol{r}\,) = E_0\, e^{(ik - \frac{1}{2}\kappa_e)z}\,. \tag{2.38}$$

For backscattering in the SAMS approximation, the relevant contributions to the total vertex are the so called 'ladder' diagrams L like the first and second term in Eq. (2.32) and 'most-crossed' diagrams C like the third term [9]:

$$\langle\Gamma(\boldsymbol{r}_1,\boldsymbol{r}_2;\boldsymbol{r}_3,\boldsymbol{r}_4)\rangle = \langle L(\boldsymbol{r}_1,\boldsymbol{r}_2;\boldsymbol{r}_3,\boldsymbol{r}_4)\rangle + \langle C(\boldsymbol{r}_1,\boldsymbol{r}_2;\boldsymbol{r}_3,\boldsymbol{r}_4)\rangle, \tag{2.39}$$

with

$\langle L\rangle =$ 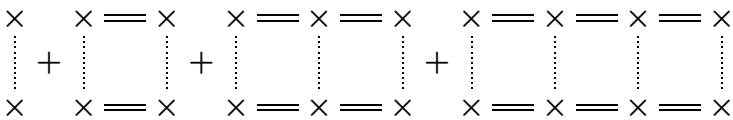 (2.40)

and

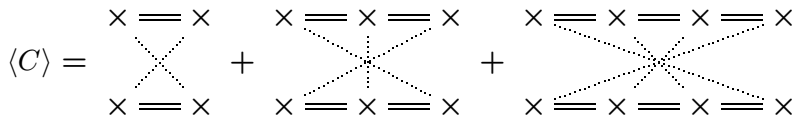

(2.41)

The sum of all combinations of ladder and most-crossed diagrams, like the last term in Eq. (2.32), can be neglected after averaging over the positions of the scatterers.

The ladder diagrams describe incoherent transport of the intensity while the most-crossed diagrams describe an interference phenomenon called coherent backscattering, which is explained in the next section. For point scatterers, the two incoming coordinates of the ladder diagrams as well as the two outgoing coordinates have to be equal. Therefore one can write the ladder series in the form:

$$\langle L(\boldsymbol{r}_1,\boldsymbol{r}_2;\boldsymbol{r}_3,\boldsymbol{r}_4)\rangle = n\,|t|^2\,\delta(\boldsymbol{r}_1-\boldsymbol{r}_3)\delta(\boldsymbol{r}_2-\boldsymbol{r}_4)\delta(\boldsymbol{r}_1-\boldsymbol{r}_2) + F(\boldsymbol{r}_1,\boldsymbol{r}_2)\delta(\boldsymbol{r}_1-\boldsymbol{r}_3)\delta(\boldsymbol{r}_2-\boldsymbol{r}_4), \tag{2.42}$$

where $F(\boldsymbol{r}_1,\boldsymbol{r}_2)$ is an intensity propagator that because of Eq. (2.34) satisfies the integral equation:

$$F(\boldsymbol{r}_1,\boldsymbol{r}_2) = n^2\,|t|^4|G(\boldsymbol{r}_1-\boldsymbol{r}_2)|^2 + n\,|t|^2\int d\boldsymbol{r}_2\;|G(\boldsymbol{r}_1-\boldsymbol{r}_3)|^2\,F(\boldsymbol{r}_3,\boldsymbol{r}_2). \tag{2.43}$$

Note that the first term in Eq. (2.43) describes single scattering.

The most-crossed series can easily be found from the ladder series by reversing the bottom line in the diagrammatic expansion (i.e. by reversing the sequence of scattering events for the complex conjugate Green's function):

$$\langle C(\boldsymbol{r}_1,\boldsymbol{r}_2;\boldsymbol{r}_3,\boldsymbol{r}_4)\rangle = F(\boldsymbol{r}_1,\boldsymbol{r}_2)\delta(\boldsymbol{r}_1-\boldsymbol{r}_4)\delta(\boldsymbol{r}_2-\boldsymbol{r}_3). \tag{2.44}$$

This means that one can find both $\langle L\rangle$ and $\langle C\rangle$ from the same intensity propagator $F(\boldsymbol{r}_1,\boldsymbol{r}_2)$.

This provides us with all the ingredients necessary to calculate the bistatic coefficient for a semi infinite slab in the xy-plane, illuminated by a plane wave from $z = -\infty$. It is convenient to separate the total bistatic coefficient γ_t into the contribution from most-crossed diagrams γ_c and from ladder diagrams, with the latter further separated into the single scattering contribution γ_s and multiple scattering contribution γ_ℓ:

$$\gamma_t = \gamma_s + \gamma_\ell + \gamma_c. \tag{2.45}$$

Using the above expressions for $\langle L \rangle$ and $\langle C \rangle$ in Eq. (2.35), one obtains the following integrals for the bistatic coefficients in backscattering:

$$\gamma_\ell(\boldsymbol{k}_s) = \frac{1}{4\pi A} \int d\boldsymbol{r}_1 ... d\boldsymbol{r}_4 e^{i\boldsymbol{k}_s \cdot (\boldsymbol{r}_1 - \boldsymbol{r}_3)} e^{-\frac{1}{2}\kappa_e \mu_s^{-1}(z_1 + z_3)} \tag{2.46}$$
$$\times F(\boldsymbol{r}_1, \boldsymbol{r}_2)\delta(\boldsymbol{r}_1 - \boldsymbol{r}_3)\delta(\boldsymbol{r}_2 - \boldsymbol{r}_4) e^{ik(z_2 - z_4)} e^{-\frac{1}{2}\kappa_e(z_2 + z_4)},$$

$$\gamma_c(\boldsymbol{k}_s) = \frac{1}{4\pi A} \int d\boldsymbol{r}_1 ... d\boldsymbol{r}_4 e^{i\boldsymbol{k}_s \cdot (\boldsymbol{r}_1 - \boldsymbol{r}_3)} e^{-\frac{1}{2}\kappa_e \mu_s^{-1}(z_1 + z_3)} \tag{2.47}$$
$$\times F(\boldsymbol{r}_1, \boldsymbol{r}_2)\delta(\boldsymbol{r}_1 - \boldsymbol{r}_4)\delta(\boldsymbol{r}_2 - \boldsymbol{r}_3) e^{ik(z_2 - z_4)} e^{-\frac{1}{2}\kappa_e(z_2 + z_4)},$$

and

$$\gamma_s(\boldsymbol{k}_s) = \frac{1}{4\pi A} \int d\boldsymbol{r}_1 ... d\boldsymbol{r}_4 e^{i\boldsymbol{k}_s \cdot (\boldsymbol{r}_1 - \boldsymbol{r}_3)} e^{-\frac{1}{2}\kappa_e \mu_s^{-1}(z_1 + z_3)} \tag{2.48}$$
$$\times\, n\, |t|^2\, \delta(\boldsymbol{r}_1 - \boldsymbol{r}_3)\delta(\boldsymbol{r}_2 - \boldsymbol{r}_4)\delta(\boldsymbol{r}_1 - \boldsymbol{r}_2) e^{ik(z_2 - z_4)} e^{-\frac{1}{2}\kappa_e(z_2 + z_4)},$$

with $\boldsymbol{k}_s$ the outgoing wavevector.

We have performed thesis integrals explicitly in the diffusion approximation using the diffusion propagator $F(\boldsymbol{r}_1, \boldsymbol{r}_2)$ as calculated in section 2.2 for a slab geometry. The resulting bistatic coefficients are,
for single scattering:

$$\gamma_s(\theta_s) = \frac{\mu_s}{1 + \mu_s} \left[1 - e^{-L\kappa_e(1 + \mu_s^{-1})} \right], \tag{2.49}$$

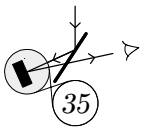

for the multiple scattering ladder diagrams (describing the diffuse background):

$$\gamma_\ell(\theta_s) = \frac{3}{2\ell^3\alpha\sin[\alpha(L+2z_0)]}\,\frac{Z_1(1+e^{-2\,uL}) + Z_2(1-e^{-2\,uL}) + Z_3 e^{-L(v+u)}}{u[(u^2-\alpha^2)^2 + v^2(v^2-2\alpha^2-2u^2)]} \tag{2.50}$$

with

$$Z_1 = u\,(u^2-v^2-\alpha^2)\cos[\alpha(L+2z_0)] + u\,(v^2-u^2-\alpha^2)\cos(\alpha L) \tag{2.51}$$

$$+2uv\alpha\sin[\alpha(L+2z_0)] + uv\alpha\,\frac{v^2-\alpha^2-3u^2}{u^2-\alpha^2}\sin(\alpha\,L),$$

$$Z_2 = v\,(v^2-u^2-\alpha^2)\cos[\alpha(L+2z_0)] + 2u^2\alpha\sin(\alpha\,L) \tag{2.52}$$

$$-\alpha\,(u^2+v^2-\alpha^2)\sin[\alpha(L+2z_0)] + u^2 v\,\frac{u^2-v^2+3\alpha^2}{u^2-\alpha^2}\cos(\alpha\,L),$$

$$Z_3 = 2u\,(u^2-v^2+\alpha^2) + 2u\,(v^2-u^2+\alpha^2)\cos(2z_0\,\alpha) - 4uv\alpha\sin(2z_0\,\alpha), \tag{2.53}$$

and for the most-crossed diagrams (describing interference):

$$\gamma_c(\theta_s) = \frac{3e^{-uL}}{2\ell^3\alpha\sinh[\alpha(L+2z_0)]}\,\frac{1}{(\alpha^2+\eta^2+u^2)^2-(2\alpha\eta)^2}\;\times \tag{2.54}$$

$$\begin{aligned}
&\big[-2(\alpha^2+\eta^2+u^2)\cosh(2\alpha z_0)\cos(L\eta) - 4\alpha\eta\sinh(2\alpha z_0)\sin(L\eta)\\
&\quad +2\frac{\alpha}{u}(-\alpha^2+\eta^2-u^2)\sinh(\alpha(L+2z_0))\sinh(uL)\\
&\quad -2(\alpha^2-\eta^2-u^2)\cos(L\eta) + 2(\alpha^2+\eta^2+u^2)\cosh(\alpha(L+2z_0))\cosh(uL)\\
&\quad +4\alpha u\sinh(\alpha L)\sinh(uL) - 2(-\alpha^2+\eta^2+u^2)\cosh(\alpha L)\cosh(uL)\big]\,.
\end{aligned}$$

In these expressions, the angular dependence is determined by the following parameters: $\eta \equiv k(1-\mu_s)$, $u \equiv \frac{1}{2}\kappa_e(1+\mu_s^{-1})$, $v \equiv \frac{1}{2}\kappa_e(1-\mu_s^{-1})$, and $\alpha \equiv \sqrt{\ell_{abs}^{-2}+q_\perp^2}$ with $q_\perp = k\sin\theta$. As mentioned before, $\mu_s = \cos\theta$,

with θ the angle between the outgoing wavevector $\boldsymbol{k}_s$ and $\hat{z}$, L is the sample thickness, $z_0 = 0.7104\ell$, and κ_e is the extinction coefficient given by $\kappa_e = \ell_s^{-1} + \ell_i^{-1}$. In the limit $L \to \infty$ (i.e. for a semi-infinite slab), the expression for γ_c reduces to:

$$\gamma_c(\theta_s) = \frac{3}{2\ell^3 \alpha u} \frac{\alpha + u(1 - e^{-2\alpha z_0})}{(u+\alpha)^2 + \eta^2} \tag{2.55}$$

The above solutions for the bistatic coefficients in backscattering in the diffusion approximation were checked against the expressions given in Ref. [10]. Our solutions are written in a different form to be able to compare them with the bistatic coefficients for backscattering from an amplifying medium (see chapter 6).

2.5 Coherent backscattering

The physical interpretation of γ_ℓ and γ_c is the following. γ_ℓ describes the (incoherent) backscattered intensity due to diffusion without interference. Its angular dependence is weak (see dashed line Fig. 2.1): it decreases slowly at larger angles. This angular dependence is due to the fact that under larger outgoing angles, the light travels through a larger part of the sample, having a larger chance to be scattered or absorbed. The intensity described by γ_c originates from interference between reciprocal [11] waves. This interference effect is called coherent backscattering or weak localization [12,13] and is a general phenomenon for waves scattered by random media. Because a random dielectric system obeys reciprocity, any partial wave that propagates over some distance through the sample and then leaves the illuminated area in the backscattering direction will have a counterpropagating counterpart that follows the same path in the opposite direction. These counterpropagating partial waves have travelled over the same distance in the sample and interfere therefore constructively in the backscattering direction. This is what is described by the most-crossed diagrams. The angular dependence of γ_c is strong: it decays rapidly moving away from the exact backscattering direction (see solid line Fig. 2.1). Away from exact backscattering, a phase difference develops between the counterpropagating waves that depends on the relative orientation of the points where the waves leave the sample. For the ensemble of light paths, the relative phases will therefore gradually randomize. After averaging over all light paths, this leads to the cone of enhanced backscattering described by γ_c.

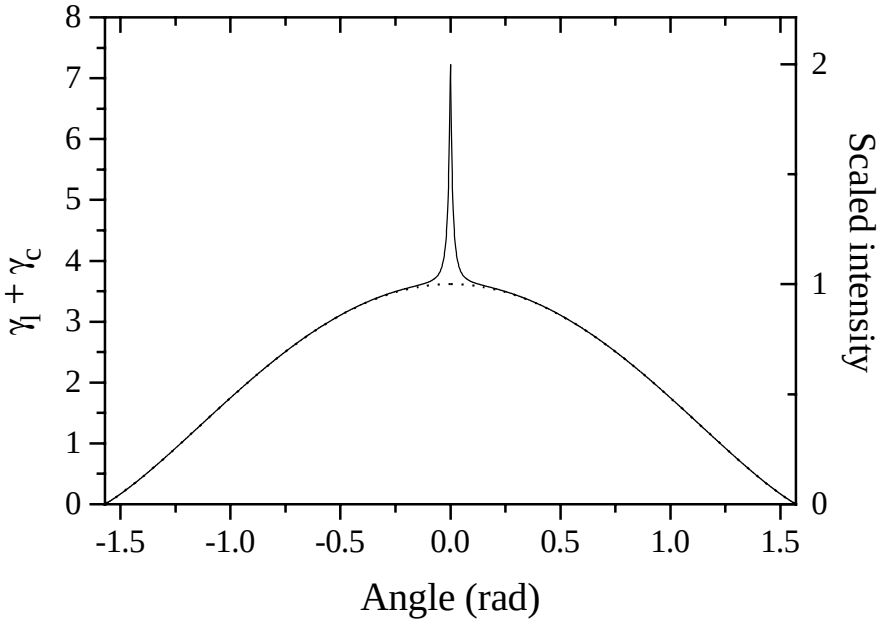

Figure 2.1: *Total bistatic coefficient versus scattering angle, calculated in the diffusion approximation for a non absorbing semi-infinite disordered sample with mean free path $\ell = 5$ μm. Wavelength $\lambda_e = 700$ nm. Scattering angle zero corresponds to exact backscattering. The dashed line is γ_ℓ, describing the diffuse background intensity. Dashed and solid line largely overlap, except in and around exact backscattering where a narrow coherent backscattering cone is present.*

2.5.1 Properties of the backscattering cone

The width of the backscattering cone is determined by the average distance between the first and last scattering event and thereby by the mean free path ℓ. The full width at half maximum is given by [10]:

$$W \simeq \frac{0.7}{2\pi} \frac{n_i}{n_e} \frac{\lambda_i}{\ell} = \frac{0.7}{2\pi} \frac{\lambda_e}{\ell}, \tag{2.56}$$

with ℓ the (transport) mean free path for light in the medium, λ_i and n_i respectively the wavelength of the light and the effective refractive index in the sample, and λ_e and n_e respectively the wavelength of the light and the refractive index in the medium between the sample and the point of

observation (usually air). The ratio n_i/n_e appears in the above equation because the outgoing waves are refracted by the refractive index contrast at the front sample interface. This refractive index contrast also leads to internal reflection in the sample. Internal reflection enlarges the average distance between first and last scattering event because the outgoing waves are partially backreflected in the sample. This leads to a narrowing of the backscattering cone [6]. Internal reflection is not accounted for in Eq. (2.56).

The enhancement factor E of the backscattering cone is defined as the ratio of the total intensity at exact backscattering to the diffuse background intensity at exact backscattering. The diffuse background intensity is the intensity which would be expected from an incoherent addition of the scattered waves. In the SAMS approximation, E is given by:

$$E = \left. \frac{\gamma_c + \gamma_\ell + \gamma_s}{\gamma_\ell + \gamma_s} \right|_{\theta=0}. \tag{2.57}$$

In the exact backscattering direction $\gamma_c = \gamma_\ell$, so if $\gamma_s = 0$, the enhancement factor is two. The single scattering contribution γ_s is zero for spherical symmetric scatterers in the helicity conserving polarization channel of the light. For other polarizations, a single scattering contribution γ_s is present. Because a singly scattered wave does not have a distinct reciprocal counterpart, single scattering does not contribute to the interference. The angular dependence of γ_s depends on the nature of the scatterers, but is generally weak. For point scatterers and scalar waves, it is given by Eq. (2.49). For a treatment of single scattering from atomic and molecular systems in the x-ray regime, we refer to Ref. [14].

The shape of the backscattering cone reflects the path length distribution of the light inside the sample and therefore reveals information about the internal structure of the sample. If the sample consists of a random collection of small particles, the mean free path ℓ is inversely proportional to the density n and scattering cross section σ of the particles. In that case, the width of the cone is a measure for the particle density. For more complex, e.g. sponge like, random structures it is difficult to identify the individual scattering elements, in which case the width of the cone is just a measure for the scattering strength of the material. The shape of the backscattering cone is sensitive to the sample structure at large depth because the top of the cone is determined by very long light paths that have penetrated deep into the sample (features that are due to $> 10^4$ scattering events can be resolved experimentally). In the theoretical case of zero absorption, the top of the backscattering cone is a cusp for a semi-infinite slab:

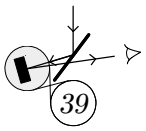

the derivative of Eq. (2.55) to θ is discontinuous at $\theta = 0$. The existence of a cusp is possible, due to the fact that at zero absorption, an infinite number of light paths contribute to the top of the cone. If absorption is present either at large depth or throughout the sample, the contribution from the longer light paths is reduced and consequently the top becomes rounded.

References and notes

[1] S. Chandrasekhar, *Radiative transfer* (Dover, New York, 1960).

[2] A. Ishimaru, *Wave propagation and scattering in random media*, Vol. I and II, (Academic press, New York, 1978).

[3] H.C. van de Hulst, *Multiple Light Scattering*, Vol. I and II, (Dover, New York, 1980).

[4] U. Frish, *Wave propagation in random media*, in *Probabilistic methods in applied mathematics*, edited by A.T. Barucha-Reid, Vol. I, 76 (Academic press, New York, 1968).

[5] H.C. van de Hulst and R. Stark, Astron. Astrophys. **235**, 511 (1990).

[6] A. Lagendijk, B. Vreeker, and P. de Vries, Phys. Lett. A **136**, 81 (1989); J.X. Zhu, D.J. Pine, and D.A. Weitz, Phys. Rev. A **44**, 3948 (1991);

[7] See e.g. J.D. Jackson, *Classical Electrodynamics*, (Wiley, New York, 1975).

[8] Th.M. Nieuwenhuizen, A. Lagendijk, and B.A. van Tiggelen, Phys. Lett. A **169**, 191 (1993).

[9] D. Vollhardt and P. Wölfle, Phys. Rev. B **22**, 4666 (1980).

[10] M.B. van der Mark, M.P. van Albada, and A. Lagendijk, Phys. Rev. B **37**, 3575 (1988) and E. Akkermans, P.E. Wolf, R. Maynard, and G. Maret, J. Phys. France **49** 77 (1988).

[11] Optical measurements on linear physical systems obey the general principal of reciprocity, i.e. their results are invariant with respect to an interchange of source and detector (see e.g. [3]). In the case of a conservative system, reciprocity is equivalent to time–reversal symmetry.

[12] M.P. van Albada and A. Lagendijk, Phys. Rev. Lett. **55**, 2692 (1985).

[13] P.E. Wolf and G. Maret, Phys. Rev. Lett. **55**, 2696 (1985).

[14] M.J.P. Brugmans, *Relaxation kinetics in disordered dense phases*, (PhD thesis, University of Amsterdam, 1995).

Chapter 3

An accurate technique to record coherent backscattering

In this chapter, a new technique is described to record the angular distribution of backscattered light. The technique is accurate over a large scanning range (500 mrad) which includes the exact backscattering direction, and the angular resolution is high (100 μrad). The technique is particularly suitable for the study of coherent backscattering from (very strongly scattering) random media. It allowed us to measure the theoretical value of two of the enhancement factor in coherent backscattering from a weakly scattering sample.

3.1 Introduction

The technique to record backscattered light which is described in this chapter, was developed for the study of coherent backscattering from random media. The experimental study of coherent backscattering puts high demands on the accuracy of a setup. A technique suitable for coherent backscattering experiments can therefore be applied to any situation where the angular distribution of backscattered light must be known accurately, for instance for backscattering experiments from rough surfaces or for the characterization of retro-reflectors.

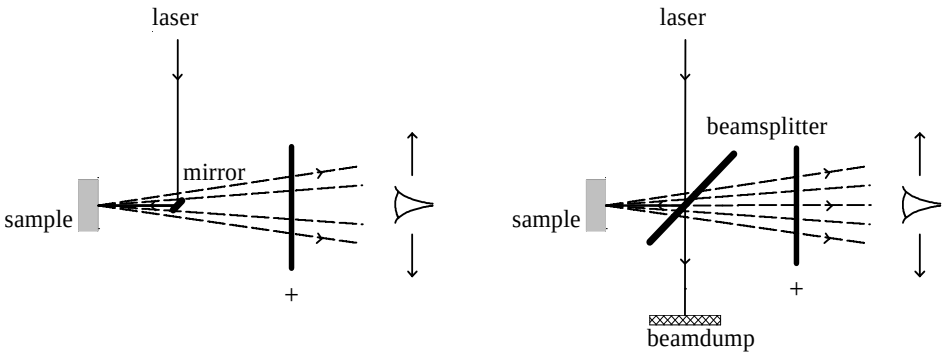

Figure 3.1: *Principle of setups used previously to record coherent backscattering. (a) (left) Simplest scheme. The incoming beam is reflected onto the sample with a small mirror. The backscattered intensity can be recorded over a large angular range but the region close to exact backscattering can not be observed. A positive lens is used to collect the scattered light. The detector is placed in the focal plane of the lens so that one scattering direction corresponds to one position of the detector. (The refraction of the waves by the lens is not shown.) (b) (right) By using a beam splitter, the exact backscattering direction can be observed but one has to correct for the angle-dependent transmission of the optics between sample and detector (beam splitter, positive lens, polarizer, etc.).*

3.1.1 Principle of previous setups

To study coherent backscattering, one must record the angular distribution of the intensity backscattered from a sample which is illuminated by a spatially broad light beam. In the experimental studies that have been published so far, two different schemes were used. In the simplest scheme, the incoming beam was reflected onto the sample by a mirror (see Fig. 3.1a) [1,2]. The scattered light is collected with a positive lens. The detector is placed in the focal plane of the lens so that one scattering direction corresponds to one position of the detector. The use of a mirror allows for a determination of the scattered intensity over a large angular range. However, the mirror masks the scattered light in and near the exact backscattering direction, so with this method the top of the backscattering cone can not be observed. Another approach was to use a beam splitter to reflect the light onto the sample (see Fig. 3.1b) [3–5]. The scattered light is recorded through the beam splitter, so the exact backscattering direction can be

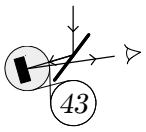

monitored. Again a positive lens is used to collect the scattered light. The disadvantage of this scheme is however, that one has to correct for the angular dependence in the transmission characteristics of the beam splitter, the positive lens, and other detection optics (e.g. a polarizer).

In both schemes it is difficult to shield stray light in a satisfactory manner. The fundamental problem arises from parallax: the screen that is used to shield stray light must be placed at some distance in front of the sample. As the detector moves, the light path from sample to detector changes. Therefore, the field of view of the detector has to be larger than the solid angle under which it sees the illuminated area on the sample. In practice this means that an amount of stray light adds to the detected signal. This yields an extra background in the signal which is even likely to show some angular dependence. As a result the shape and enhancement factor of the backscattering cone can not be recorded accurately.

3.2 Experimental configuration

3.2.1 Principle of the setup

We have developed a new method which we call 'Off-Centered Rotation' (OCR), to solve the experimental problems described above. The outline of the setup is drawn in Fig. 3.2a. The incoming light beam is reflected via a beam splitter onto the sample. The scattered light is collected with a positive lens ($f = 1$m). The head of an optical fiber is placed in the focus of the positive lens. The fiber transports the light to a photo multiplier tube. Detection optics, beam splitter and sample are placed on a rotating frame. The center of rotation C', is the center C of the sample surface mirrored with respect to the plane of the beam splitter. Fig. 3.2b shows the setup after rotation. The incoming beam is directed at C, so after rotation it still arrives at the center of the sample surface C'. With respect to the frame, the incoming direction has changed and the direction of detection is still the same. By rotating the sample around C, the sample surface is kept at a constant angle with respect to the incoming beam. The rotation is obtained by placing the sample on a (rotatable) plateau, which is connected by a twisted band to a disc of the same size that is fixed to the laboratory frame. Thus the incoming direction on the sample is fixed and the angular distribution of the scattered light is recorded. The rotation of the setup is demonstrated around the odd page numbers of this thesis.

The scattered light always follows the same path through the beam splitter and the detection optics. This is the major advantage of our set-

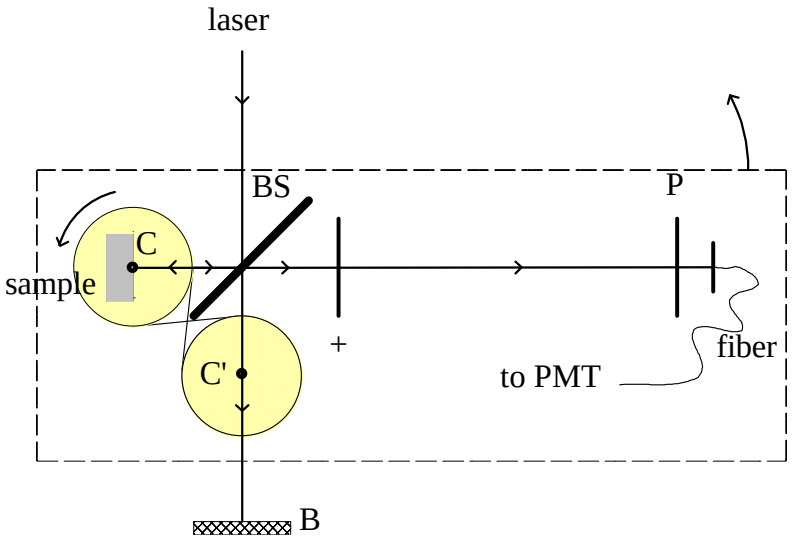

Figure 3.2a: *Outline of the setup to record the angular distribution of a backscattered intensity. The essence of the setup is that all optical components are placed on a frame which rotates around C', which is the mirror image in the beam splitter (BS) of the center C of the front sample surface. In this way, the path from sample to detector of the scattered light is always the same. The sample rotates around C to keep the incoming direction perpendicular to the sample surface. The scattered light is focused by a positive lens (+) on the head of an optical fiber which is placed in the focal plane of the lens. The fiber transports the light to a Photo Multiplier Tube (PMT). The polarizer P is used to select one polarization channel of the scattered light. The laser beam transmitted through the beam splitter is blocked by a beam dump (B), that must be of high quality as backreflections would reach the detector.*

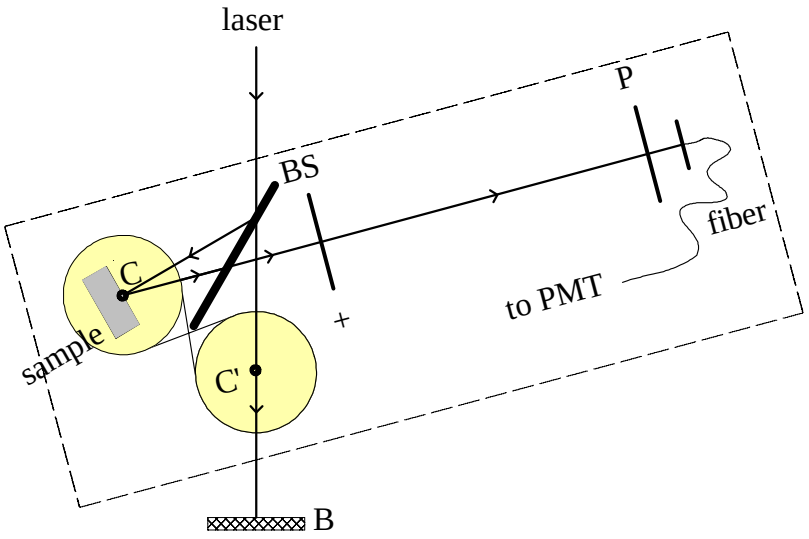

Figure 3.2b: *Same setup after rotation to another detection angle.*

up: it avoids any corrections for angular dependence in the transmission of the components. The one remaining angular dependence in the setup is in the reflection of the incident beam by the beam splitter, but this dependence can in principle be measured to any desired accuracy by replacing the sample with a detector.

In order to observe a coherent backscattering cone it is necessary to average over many configurations of the sample. This eliminates the speckle pattern which is formed if a coherent beam is scattered by a (stationary) random sample [5]. In a fluid sample, Brownian motion of the particles provides the required ensemble averaging. Solid samples are mounted on a small motor which spins them around their axis. An efficient ensemble averaging is obtained if the sample surface is not exactly perpendicular to the axis of rotation, so that the sample 'wiggles'.

3.2.2 Polarization

The polarization of the incoming laser beam is linear, and a polarizer is mounted in front of the optical fiber head. The parallel or perpendicu-

lar polarization channel in the scattered light is selected by means of this polarizer. If experiments with circularly polarized incident light are desired, a quarter-wave plate is mounted in front of the sample to convert the incoming linear polarization to circular polarization. The two circular components of the outgoing scattered light are converted back by this quarter waveplate to mutually perpendicular linear components. The polarizer in front of the fiber is used in that case to select the linear polarization that corresponds to either one of the helicity channels of the scattered light.

A setup with two quarter waveplates, where one is placed in the incident beam and one in front of the detector, in not possible for the following reason. The reflection coefficient of the beam splitter depends both on the angle and on the polarization. An incoming circular polarization would become elliptical after reflection on the beamsplitter, and the ellipticity would be angle-dependent. This is why one waveplate is mounted in front of the sample. The incident and scattered waves will pass this quarter waveplate under necessarily different angles. Since only at perpendicular incidence the relative phase shift corresponds to exactly a quarter of a wave, some mixing of polarizations will occur in directions that are far from exact backscattering. We used a zero order quarter waveplate because its angular tolerance is far greater than that of a multi order one. We found that even at the largest angles studied, the intensity coupled into the opposite polarization channel remained $< 1\%$. In directions far from exact backscattering, our random samples scramble the polarization almost completely. Errors from mixing of polarization due to oblique incidence in the quarter waveplate, will therefore essentially cancel. We estimate the overall error in the measured curves due to oblique incidence in the quarter waveplate to be $< 0.1\%$.

3.2.3 Angular resolution and scanning range

The scanning range of the setup is determined by the size of the beam splitter. We have used a beam splitter of 5 cm diameter and an incoming beam diameter of 5 mm, and obtained a scanning range of about 500 mrad. The angular resolution of the setup was diffraction limited by the diameter d of the incident beam. With $d = 5$ mm and using visible light, this limit is ≈ 100 μrad. The detection optics (50 μm core fiber, with its tip at a 1 m distance from the sample) allows in principle a resolution of 50 μrad.

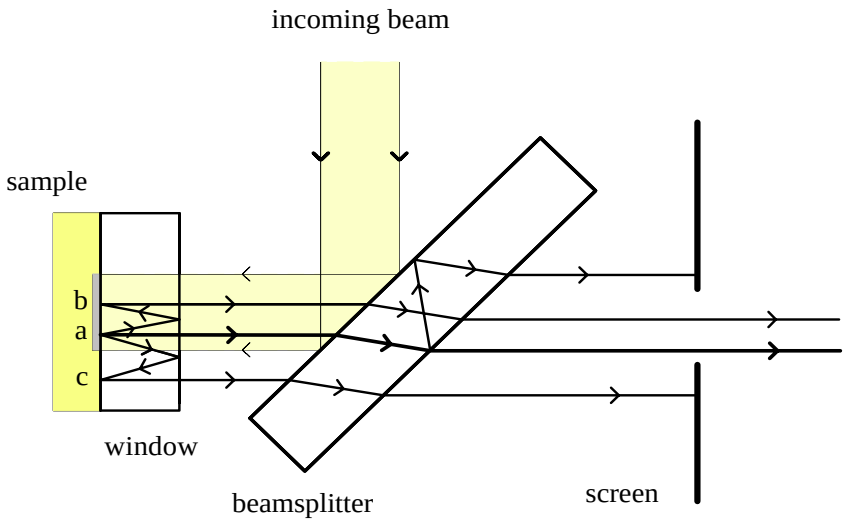

Figure 3.3: *Overview of some important ghost reflections that can give rise to experimental artifacts. The scattered light from the sample at point (a) can be reflected by the front face of the sample window. If the light is reflected to a point (b) inside the illuminated area, the scattered light from (b) will be recorded by the detector. If the light is reflected to a point (c) outside the illuminated area, the scattered light from (c) is blocked by the screen. The screen also blocks the ghost reflections from the rear side of the beam splitter.*

3.2.4 Elimination of important artifacts

Liquid samples are contained in a sample cell. The front window of this sample cell can give rise to artifacts, mainly due to back reflections from its front face. (The back face is largely index matched with the sample.) We have to distinguish between light that is reflected back on the illuminated region of the sample and the light which is reflected outside this area (see Fig. 3.3). In the first case, the light is scattered again by the sample and contributes in backscattering to the backscattering cone. Whether these contributions can be resolved depends on what the limiting factor on the angular resolution of the setup is. If the limiting factor is the size of the illuminated area, these contributions can be resolved. They will affect the observed shape of the backscattering cone. Because the reflection will on average increase the distance between first and last scattering event,

the cone will become narrower. If the angular resolution is lower, these contributions can not be (fully) resolved, and will lead to a lowering of the observed enhancement factor. The light that is reflected by the front window surface to regions outside the illuminated area can not contribute to the backscattering cone because these waves have no counterpropagating counterparts. This light will however contribute to the background and will therefore also lower the observed enhancement factor.

To reduce the above effects, the glass window must be thick (1 cm) and its front side must be anti-reflection coated. Moreover, the second effect can be eliminated by placing a diaphragm between the beam splitter and the positive lens. The aperture of this diaphragm is only slightly larger than the illuminated region on the sample. It is aligned such that only scattered light from the illuminated region can reach the detector. Note that this solution is possible because in our setup the light path from sample to detector is always the same. This property of the setup also allows to shield other sources of stray light in a convenient way without the risk of partly masking the field of view of the detector during part of an angular scan ('clipping').

A glass window can also be used to index match the front interface of a rigid sample, in order to eliminate internal reflection [6]. The same considerations hold as for the front window of a liquid sample cell. Great care has to be taken to ensure a good optical contact between window and sample surface. We obtained good results if we coated the rear side of the glass window with collodium and pressed this side with force on the sample.

The beam splitter is a slightly wedged thick window with a 50 % reflectance coating on the front side and an anti-reflection coating on the back side. All (multiple) reflections that arise from the small remaining reflection of the back surface will be blocked by the diaphragm placed between beam splitter and positive lens if the beam splitter is sufficiently thick (about 1cm). Due to its wedged shape, etalon effects in the beam splitter are also avoided.

3.2.5 Response of the setup

To check the response of the setup over a large angular range, we have recorded the backscattering from a very weakly scattering sample (i.e. a sample with a very large mean free path) (see Fig. 3.4). The backscattering cone of this (teflon) sample is extremely narrow so the major part of the scan yields the (almost angle-independent) diffuse background. The solid line in Fig. 3.4 is the diffuse background in the diffusion approximation [given by Eq. (2.50)]. Agreement between data and theory is very good.

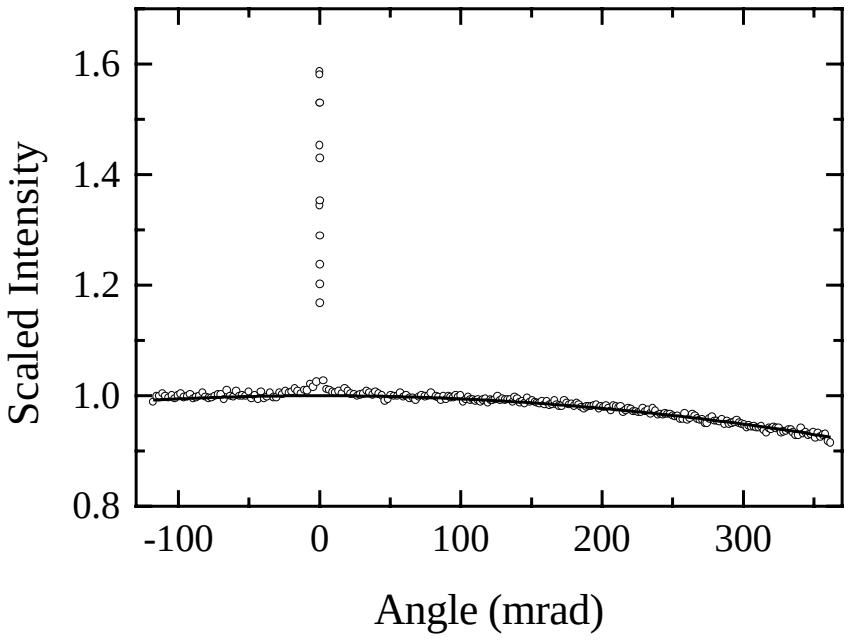

Figure 3.4: *Backscattered intensity plotted against the scattering angle, where zero corresponds to exact backscattering. Sample material Teflon, sample interface index matched. The intensity is scaled such that the diffuse background in the exact backscattering direction is 1. The solid line is the theoretical shape of the diffuse background* γ_ℓ.

3.3 Results

3.3.1 Enhancement factor

As explained in section 2.5, the theoretical enhancement factor in the helicity conserving polarization channel is two for weak scattering (i.e. in the SAMS approximation). The behaviour of the enhancement factor at very strong scattering is discussed in chapter 4. Several experimental studies on the backscattering cone in the weak scattering regime have been published [1–5,7–9] but due to experimental difficulties, the reported enhancement factors have always been considerably lower than the theoretical value of two. The difficulties arise from the fact that the scanning range of the setup must be very large compared to the angular resolution, and all stray light must be completely eliminated. The OCR setup allowed us to measure

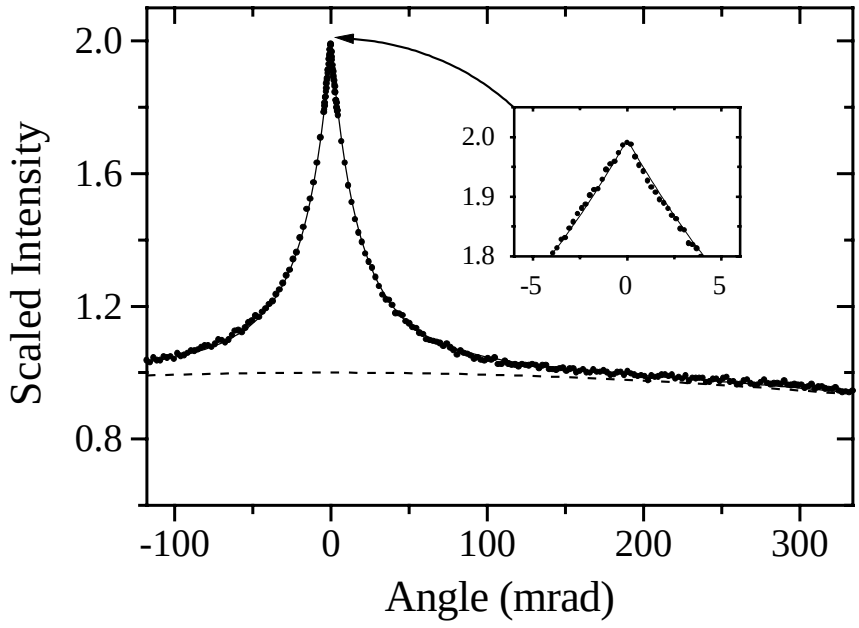

Figure 3.5: *Backscattered intensity plotted against the scattering angle, where zero corresponds to exact backscattering. Sample material ZnO powder, (transport) mean free path $\ell = 1.9 \pm 0.1$ μm. The intensity is scaled such that the diffuse background (dashed line) in the exact backscattering direction is 1. The solid line is the total scattered intensity from Eq. (3.1) in the diffusion approximation. Insert: enlargement of the top of the cone. The enhancement factor is* 1.994 ± 0.012.

enhancement factors of 2.000 ± 0.012 for weakly scattering samples.

In Fig. 3.5, a backscattering cone from a ZnO sample with mean free path $\ell = 1.9$ μm is shown. The light was circularly polarized by using the quaterwaveplate in front of the sample, and the helicity conserving channel was monitored.

The enhancement factor was determined in the following way. The enhancement factor is defined as the ratio of the total intensity to the diffuse background intensity at exact backscattering. It is impossible to measure the diffuse background intensity at exact backscattering directly, however

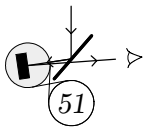

the diffuse background is largely angle-independent over the angular extend of the backscattering cone. One can determine the enhancement factor by comparing the data with a theoretical expression for the total intensity that allows for extra background contributions from experimental artifacts:

$$I(\theta) = a_0[\gamma_c(\theta) + (1+\epsilon)\gamma_\ell(\theta)]. \tag{3.1}$$

Here a_0 is a normalization factor, and $\epsilon \gtrsim 0$ determines the contribution to the background intensity due to artifacts, where it is assumed that these contributions have the same angular dependence as γ_ℓ. The enhancement factor is then given by:

$$E = \left.\frac{\gamma_c + (1+\epsilon)\gamma_\ell}{(1+\epsilon)\gamma_\ell}\right|_{\theta=0} = \frac{2+\epsilon}{1+\epsilon}, \tag{3.2}$$

where ϵ is determined from the data. Note that in order to determine ϵ accurately, the scanning range must be large enough to cover at least the wings of the cone where γ_c is almost zero.

We have determined the enhancement factor for various measurements from samples in the weak scattering regime. The samples are suspensions of TiO_2 in 2-methylpentane 2,4-diol and powders of ZnO or $BaSO_4$. The light was circular polarized and the wavelength was either 514.0 nm or 632.8 nm. The results are shown in Table 3.1. The enhancement factor for all measurements is in the range 2.000 ± 0.012. The mean free path was determined from the width of the cone using equation 2.56.

3.3.2 The shape of the backscattering cone

As can be seen from Fig. 3.5, the shape of the backscattering cone agrees very well with the backscattering cone calculated in the diffusion approximation. The intensity propagator $F(\boldsymbol{r}_1, \boldsymbol{r}_2)$ needed to calculate the backscattering cone can also be found without making the diffusion approximation, either numerically for a finite slab [8,9] or analytically for a semi-infinite slab geometry [10]. This leads to a solution for the backscattering cone that is exact for scalar waves, but which not necessarily describes the backscattering cone for light better than the diffusion approximation. Firstly, light waves are vector waves. Secondly, the exact calculation assumes point scatterers whereas the real physical scatterers are irregularly

Sample	Wavelength nm	ℓ μm	Enh. factor
$BaSO_4$ powder	514.0	2.02	2.011
$BaSO_4$ powder	514.0	1.89	2.000
$BaSO_4$ powder	632.8	2.31	2.012
$BaSO_4$ powder	632.8	2.42	1.993
ZnO powder	514.0	1.89	1.994
ZnO powder	632.8	3.23	1.992
TiO_2 susp. ($\pm$ 1.5 g/ml)	632.8	1.11	2.003
TiO_2 susp. ($\pm$ 1.3 g/ml)	632.8	1.24	2.004

Table 3.1: *Enhancement factor for coherent backscattering cones in the helicity conserving polarization channel for various samples. The (transport) mean free path ℓ was determined from the width of the cone. We estimate the error in the listed enhancement factors to be 0.012.*

shaped and have a diameter of the order of the wavelength. In the diffusion approximation no assumption on the type of scatterers is necessary.

The difference between the backscattering cones in both descriptions is small. The difference occurs in the wings of the cone, which are formed by the lowest order scattering. Diffusion theory underestimates the contribution from the lowest order scattering compared to the exact scalar solution and therefore the wings of the cone in the diffusion approximation decay more rapidly going to large angles.

We have compared the exact solution and the diffusion approximation with our data. The residues from subtracting theory from the experimental cone of Fig. 3.5, are shown in Fig. 3.6. We see from Fig. 3.6 that diffusion theory describes the backscattering cone surprisingly well. If we calculate the total squared error χ^2 defined as:

$$\chi^2 = \sum_i [I_e(\theta_i) - I_t(\theta_i)]^2, \tag{3.3}$$

where $I_e(\theta_i)$ is the measured intensity at angle θ_i and $I_t(\theta_i)$ is the theoretical intensity at this angle, we find: $\chi^2 = 3.8 \cdot 10^{-5}$ for diffusion theory and $\chi^2 = 6.8 \cdot 10^{-4}$ for the exact theory. What remains an open question

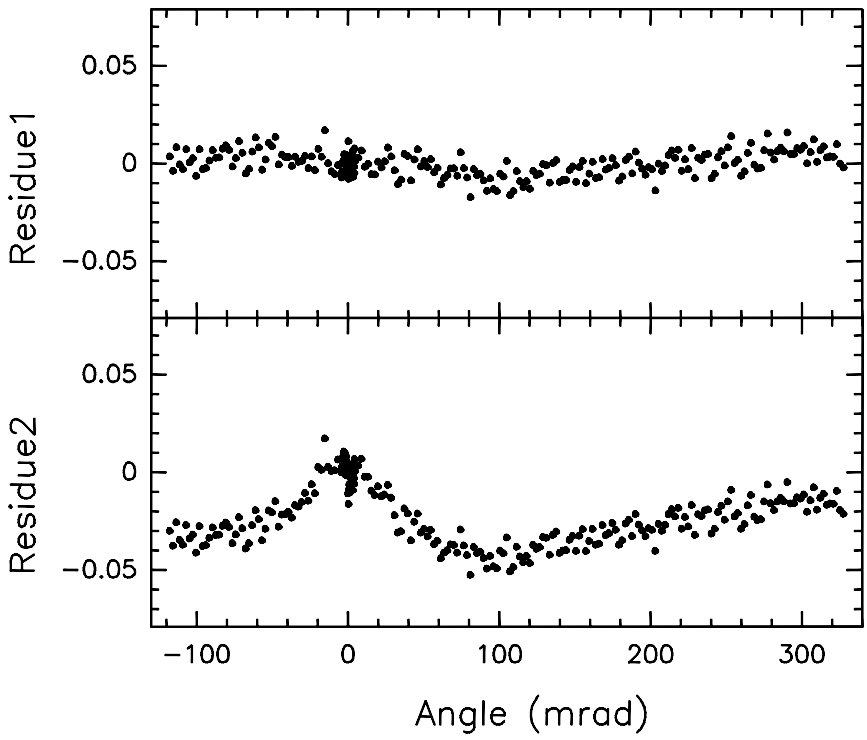

Figure 3.6: *Residues from subtracting theory from the experimental cone of Fig. 3.6 (normalized to the diffuse background at $\theta = 0$). Residue 1: diffusion approximation, Residue 2: exact scalar solution.*

is why the diffusion approximation corresponds better with the data than the exact solution. A possible explanation lies in the polarization character of light which is not taken into account in either theory. For the lower order scattering, less light is scattered in the helicity conserving than in the helicity reversing polarization channel, whereas for the higher orders the polarization is completely scrambled. Therefore, the lower order contributions in the helicity conserving polarization channel are less important than an exact scalar theory predicts. The diffusion approximation underestimates the contribution from the lowest orders compared to the exact solution and this apparantly results in a better description of the backscattering cone.

References and notes

[1] M. Kaveh, M. Rosenbluh, I. Edrei, and I. Freund, Phys. Rev. Lett. **57**, 2049 (1986).

[2] M. Rosenbluh, I. Edrei, M. Kaveh, and I. Freund, Phys. Rev. A **35**, 4458 (1987).

[3] M.P. van Albada and A. Lagendijk, Phys. Rev. Lett. **55**, 2692 (1985).

[4] P.E. Wolf and G. Maret, Phys. Rev. Lett. **55**, 2696 (1985).

[5] S. Etemad, R. Thompson, and M.J. Andrejco, Phys. Rev. Lett. **57**, 575 (1986).

[6] A. Lagendijk, B. Vreeker, and P. de Vries, Phys. Lett. A **136**, 81 (1989); J.X. Zhu, D.J. Pine, and D.A. Weitz, Phys. Rev. A **44**, 3948 (1991); Th.M. Nieuwenhuizen and J.M. Luck, Phys. Rev. E **48**, 569 (1993).

[7] Y. Kuga and A. Ishimaru, J. Opt. Soc. Am. A **8**, 831 (1984).

[8] M.B. van der Mark, M.P. van Albada, and A. Lagendijk, Phys. Rev. B **37**, 3575 (1988).

[9] P.E. Wolf, G. Maret, E. Akkermans, and R. Maynard, J. Phys. France **49**, 63 (1988).

[10] E.E. Gorodnichev, S.L. Dudarev, and D.B. Rogozkin, Phys. Lett. A **144**, 48 (1990).

Chapter 4

Experimental evidence for recurrent multiple scattering

4.1 Introduction

In chapter 2, an introduction is given to the theory which is commonly used to treat multiple light scattering in disordered media. The presented derivations are valid for relatively weakly scattering media, because recurrent scattering is neglected. Recurrent scattering events are events in which a wave is scattered by a specific scatterer, scattered by at least one other scatterer and then returns to this specific scatterer. For relatively weak scattering, recurrent events can be neglected, because the chance of a wave returning to a specific scatterer is very small. This approximation is called the 'self-avoiding multiple scattering' (SAMS) approximation. In most experimental studies that have been published so far, the scattering was weak enough to neglect recurrent scattering.

To explain the relevance of recurrent scattering, a parallel can be drawn to electron scattering. It is known that the propagation of electrons in a disordered structure can change tremendously in the strong scattering regime. Below a critical value of the electron scattering mean free path, the diffusion of the electrons can disappear. This phenomenon is known as Anderson localization [1]. The propagation of light in disordered dielectrics shows interesting similarities to electron transport in disordered (semi-)conductors [2], and it is challenging to find an optical counterpart of Anderson localization. Recurrent scattering plays an important role in the theory of Anderson localization [3,4]. The reduction of the diffusion constant can be explained by constructive interference between waves that

have propagated along the same path in opposite directions. Due to this constructive interference, the probability for a wave to return to a specific scatterer increases and thereby the probability to propagate away from this scatterer decreases. So far however, no experimental evidence was present for the existence of recurrent scattering of light waves in disordered media.

A parameter which is a measure for the scattering strength is $(k\ell_s)^{-1}$, where ℓ_s is the scattering mean free path and k is the wavenumber of the light in the medium. If Anderson localization of light is possible, it is expected to occur at very strong scattering, that is for very small $k\ell_s$. For electrons, a localized state is obtained at $k\ell_s < 1$. This criterion is known as the Ioffe-Regel criterion [5]. For light it is very difficult to obtain samples in the regime $k\ell_s < 1$ (see section 1.1.3). However it is possible to get close to $k\ell_s = 1$, where effects from recurrent scattering might already be visible.

In this chapter, we will study coherent backscattering from strongly scattering media, to find evidence for recurrent scattering of light waves. The relevant parameter in these experiments is the enhancement factor of the backscattering cone, which is the ratio of the total scattered intensity at exact backscattering to the diffuse background. As explained in section 2.5.1, the enhancement factor is two in the weak scattering regime, if the single scattering contribution is eliminated. Single scattering lowers the enhancement factor because it does not contribute an interference term. In a single scattering event, a wave enters and leaves the sample on the same scatterer. If recurrent scattering occurs, we expect the subclass of recurrent events in which first and last scattering occurs on the same scatterer, to behave similar to single scattering (see Fig. 4.1). One can distinguish between these recurrent events and single scattering, by using circularly polarized light and monitoring the helicity conserving polarization channel. Single scattering will not be present in the helicity conserving channel using spherical symmetric scatterers, whereas for recurrent scattering the polarization will be (at least partly) scrambled. This means we have to measure the enhancement factor in the helicity conserving channel as a function of the scattering strength, where deviations from two close to $k\ell_s = 1$ would be a manifestation of recurrent scattering.

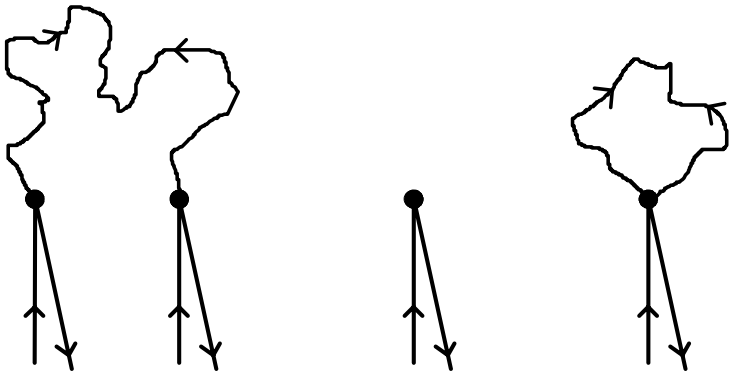

Figure 4.1: *Different light paths that contribute to the scattered intensity. (a) (left) Regular self-avoiding multiple scattering (SAMS). (b) (middle) Single scattering. (c) (right) Recurrent multiple scattering, with first and last scattering event on the same scatterer. Because the two outgoing waves coincide, this event behaves similar to single scattering.*

4.2 Experimental procedure

4.2.1 Preparation of strongly scattering samples

Various experimental parameters can be varied, but it is difficult to reach $k\ell_s = 1$ for optical waves. In the case of electrons, one can simply increase the wavelength to obtain small values of $k\ell_s$. In the optical case this is not possible, because for wavelengths much larger than the size of the scattering elements one enters the Rayleigh scattering regime, in which case the scattering cross section is inversely proportional to λ^4. For optical waves, the strongest scattering is obtained if λ is in the order of the size of the scatterers.

In order to obtain strongly scattering samples, one needs a material with a randomly varying refractive index in which the refractive index contrasts are as high as possible. Also, the absorption coefficient of the material should be very small. The presence of a small amount of absorption kills the contributions from the longest light paths. Most materials that have negligible absorption at visible wavelengths, have a refractive index of $n < 2.0$. An exception is TiO_2 which has a refractive index of $n \simeq 2.8$ and an

absorption coefficient of $\kappa_i \simeq 10$ mm^{-1} at $\lambda_{vac} = 514$ nm. Various powders based on TiO_2 are used as pigments in the paint industry because of their strong scattering properties.

We have used a powder of rutile TiO_2 microparticles that was treated with SiO_2, Al_2O_3, and organical compounds to prevent the particles from clustering [6]. The diameter of the particles in this powder is in the range of 100 nm to 300 nm. The powder was suspended in chloroform and ground in a planetary micro mill for about 1 minute to break possible clusters. We found that milling times longer than 5 minutes are undesirable because after 5 minutes the particles start to cluster, possibly because their coating is removed (see Fig. 4.2). After grinding, the chloroform was left to evaporate. This way, samples could be obtained with $k\ell_s \simeq 6$ at $\lambda_{vac} = 514$ nm.

Other values of $k\ell_s$ were obtained by varying the sample material and wavelength. Apart from TiO_2, also ZnO ($n = 2.0$) and $BaSO_4$ ($n = 1.6$) were used. The latter is available as a diffuse reflectance coating [7]. Apart from the refractive index of the scatterers themselves, the refractive index of the surrounding medium was varied as well, by suspending the TiO_2 particles either in methylpentanediol ($n = 1.43$) or in methanol ($n = 1.33$).

4.2.2 Enhancement factor in coherent backscattering

We have recorded backscattering cones from the various strongly scattering samples, using the 'off-centered rotation' setup described in chapter 3. Great care was taken in recording the backscattering cones accurately as many experimental artifacts also result in an enhancement factor smaller than two. With the setup described in chapter 3, it was possible to determine the enhancement factor in a reliable way and with the desired accuracy.

The procedure of determining the enhancement factor is essentially the same as described in section 3.3.1. We allow for extra contributions to the intensity from recurrent events where we make the realistic assumptions that (a) these contributions have the same angular dependence as γ_ℓ and (b) the shape of the backscattering cone remains the same. So we compare our data to the theoretical intensity given by:

$$I(\theta) = a_0[\gamma_c(\theta) + (1+\epsilon)\gamma_\ell(\theta)], \tag{4.1}$$

where a_0 is a normalization factor and ϵ is the relative contribution of

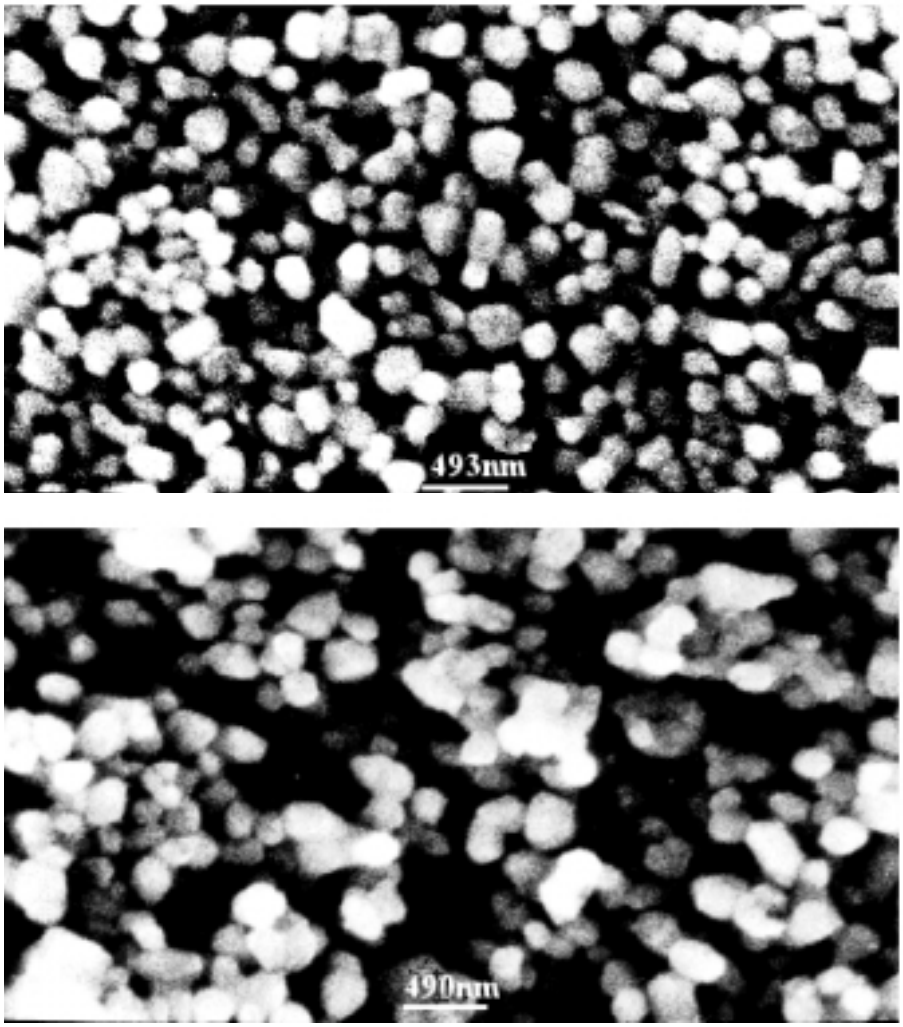

Figure 4.2: *SEM pictures of two TiO_2 powder samples. (a) (above) Sample structure after grinding a suspension rutile TiO_2 powder in chloroform in a planetary micro mill for 1 minute and letting the suspension dry on a piece of cardboard. (b) (below) After grinding for $\gtrsim$ 5 minutes the particles form clusters, possibly because their coating is removed in the grinding process.*

recurrent events. The enhancement factor E in terms of ϵ is then given by:

$$E = \left.\frac{\gamma_c + (1+\epsilon)\gamma_\ell}{(1+\epsilon)\gamma_\ell}\right|_{\theta=0} = \frac{2+\epsilon}{1+\epsilon}. \tag{4.2}$$

For γ_ℓ and γ_c, we take the the bistatic coefficients for weak scattering calculated in the diffusion approximation [Eqs. (2.50) and (2.54)]. As we have shown in section 3.3.2, both the diffuse background and the backscattering cone in the helicity conserving channel are very well described by diffusion theory.

The enhancement factor was determined by fitting the backscattering cone of Eq. (4.1) to the data with ϵ, a_0, and the cone width W [8] the adjustable parameters. We found that this procedure gives reliable values for the enhancement factor provided that the scanning range is so large that the wings of the cone are almost completely covered. It is important to know the intensity in the wings because the ratio of top to wings determines E. We have checked our method of determining E in different ways. To verify whether the results do not critically depend on the precise theoretical cone shape, we have used for γ_c the exact solution for scalar waves [9] instead of the diffusion approximation. In that case, the correspondence between experimental data and theoretical backscattering cone is not as good as when using diffusion theory, but the behaviour of the enhancement factor versus $k\ell_s$ remains the same. We also tried to fit all our results forcing $E = 2$ and keeping the other parameters free. In that case, the mean squared error of the fit remains essentially the same at large W^{-1}, whereas at small W^{-1}, the theoretical cone systematically deviates from the data and the mean squared error becomes larger by a factor $\gtrsim 4$.

4.2.3 Determination of the mean free path

The mean free path can be found in principle from the width of the cone using Eq. (2.56): $W = (0.7/2\pi)(\lambda_e/\ell)$, where λ_e is the wavelength in the medium between the sample and the detector (air). However, this expression does not incorporate effects from internal reflection by the refractive index contrast at the front sample interface. Internal reflection reduces the width of the backscattering cone [10], so if we wish to infer ℓ from the width of the cone, we either have to eliminate internal reflection or we have to estimate how large the effect is and compensate for it. We have pursued both options in our experiments, in order to be able to compare the results. Internal reflection was eliminated for some samples by index

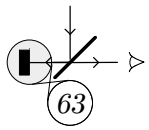

matching the sample interface with a thick (1 cm) glass window. For the non index matched samples we generalize Eq. (2.56) to [10]:

$$W \simeq \xi \frac{0.7}{2\pi} \frac{\lambda_e}{\ell}, \tag{4.3}$$

where ξ must be calculated from the average refractive index of the sample, as is done in the next section.

4.3 Results

An example of two backscattering cones is shown in Fig. 4.3. The broad cone corresponds to a sample with a very small mean free path ($k\ell_s = 5.8 \pm 1.0$), while the narrow cone corresponds to a sample in the weak scattering regime. As we can see from the inset, the enhancement factor in the measurement on the stronger scattering sample, is smaller than two.

We have recorded various backscattering cones from the TiO_2, ZnO and $BaSO_4$ powders and from the suspensions of TiO_2 in methylpentanediol and methanol. Most samples were prepared both with an index matched and with a non index matched interface. The measurements were performed at two wavelengths: 514 nm and 633 nm, and the helicity conserving channel was monitored. For all measurements, the enhancement factor was determined as a function of the inverse cone width W^{-1}, which is plotted in Fig. 4.4. The two classes of measurements, one with an index matched and one with a non index matched sample interface, are shown separately. In both series the enhancement factor is 2.00 ± 0.01 for large W^{-1} and drops below 2.00 for very small W^{-1}, which corresponds to very short mean free paths.

4.3.1 Enhancement factor versus mean free path

As we are interested in the functional dependence of E on the $k\ell_s$, we have to calculate ℓ_s from the cone width W. For the index matched series we can simply use Eq. (4.3) with $\xi = 1$, assuming isotropic scattering ($\ell_s = \ell$) [11]. For the non index matched series, we have to estimate ξ. The reflectivity R of the sample interface depends on the refractive index contrast at the boundary. The bulk refractive index (n_{med}) of a collection of particles with refractive index n_2 in a surrounding medium with refractive index n_1 (where $n_1 < n_2$), is generally much lower than the weighted average of n_1 and n_2 [12]. For the 35 vol% TiO_2-air samples, it is estimated to be 1.35 ± 0.10,

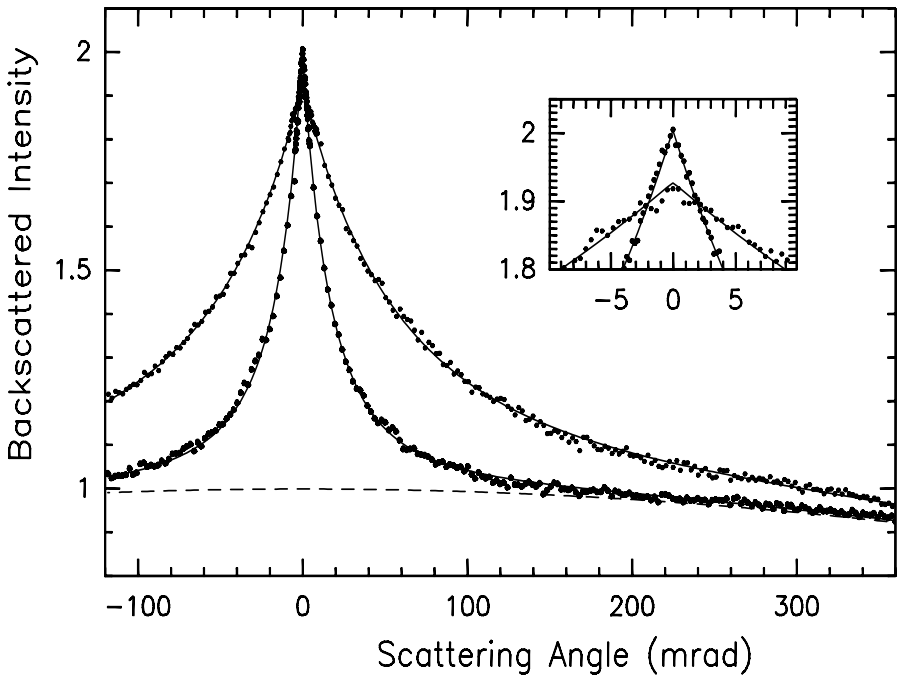

Figure 4.3: *Two measurements of backscattering cones corresponding to a short (broad cone) and long (narrow cone) mean free path. The backscattered intensity is plotted against the scattering angle where zero corresponds to exact backscattering. The solid and dashed line are respectively the cone and diffuse background from diffusion theory. Narrow cone: $BaSO_4$ sample, (scaled) mean free path $k\ell_s = 22.6 \pm 1.0$. Broad cone: TiO_2 sample, $k\ell_s = 5.8 \pm 1.0$. (Both interfaces non index matched.) The inset shows the top of both cones. The enhancement factor of the broad cone clearly deviates from* 2.00.

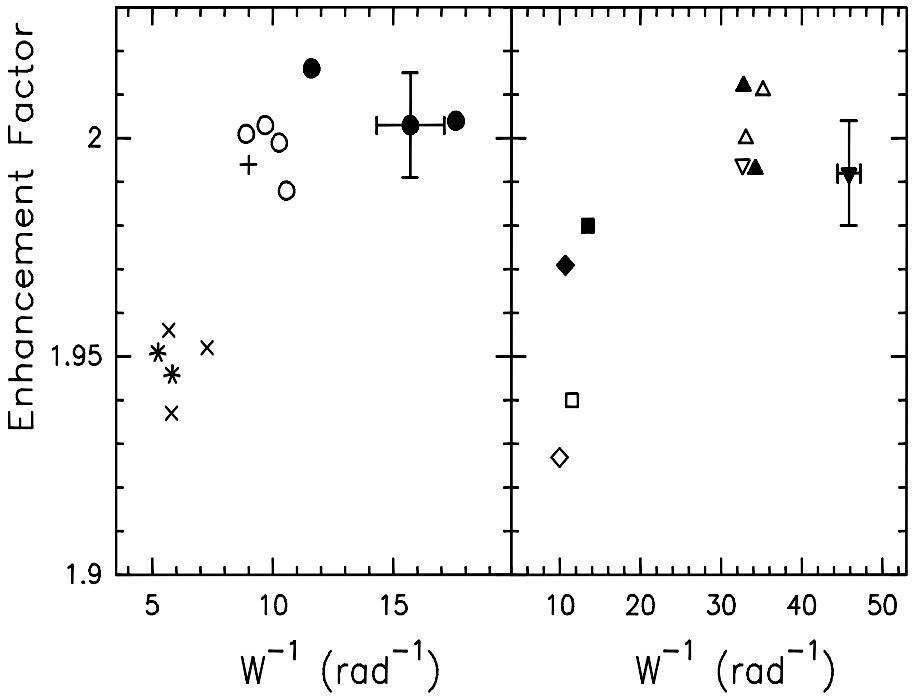

Figure 4.4: *Enhancement factor as a function of W^{-1}, where W is the width (FWHM) of the cone. The left graph: series with index matched sample interface, right graph: series with non index matched interface. For a definition list of used symbols see the caption of Fig. 4.5.*

which results in a reflectivity of $R \simeq 0.45$ [10]. This reflectivity reduces the width of the cone by a factor $\xi = 0.62 \pm 0.07$ [10]. Likewise, we estimate the bulk refractive index of the $BaSO_4$ and the 35 vol% ZnO-air samples at about 1.2, yielding a correction factor $\xi = 0.76 \pm 0.10$.

The above correction for internal reflection is approximate, because both the calculation of ξ from the average refractive index and the calculation of the average refractive index from the sample properties, are difficult. Therefore, the results from the index matched and non index matched series of measurements are shown separately in Fig. 4.4. For both series the same lowering of the enhancement factor is observed, which assures us that this effect is not an artifact induced by internal reflection or other surface effects. Despite the approximate character of the correction for internal reflection, both series of measurements merge perfectly if we

plot the enhancement factor versus $k\ell_s$ (see Fig. 4.5). The enhancement factor is 2.00 ± 0.01 for $k\ell_s \gtrsim 10$ and gradually drops below 2.00 for smaller values of $k\ell_s$.

4.4 Interpretation

In the SAMS approximation the enhancement factor in the helicity conserving channel is exactly two. Therefore a deviation from two at small $k\ell_s$ must arise from recurrent scattering events. We propose two new classes of recurrent events that can reduce the enhancement factor at strong scattering. The first we call the class of 'loop' events (see Fig. 4.6a). These are events that do have a reciprocal counterpart and therefore exhibit an interference term. However, the interference contribution of these events has the same angular dependence as their background contribution, because first and last scattering is on the same scatterer. This interference contribution is therefore observed as background, which lowers the observed enhancement factor. The second class we call the class of recurrent 'folded' events (see Fig. 4.6b). These are recurrent multiple scattering events that are identical to their reciprocal counterpart. Reversing the bottom line in the diagram does not generate a new diagram. These events only contribute to the diffuse background and do not exhibit an interference term. Consequently folded events lower the enhancement factor. It is important to note the difference between folded and loop events. While folded events lower the enhancement factor because they do not contribute to the interference, loop events lower only the *observed* enhancement factor because their interference contribution is observed as background.

4.5 Theory

In general, the total scattered intensity is determined by the total four-point vertex $\Gamma(\boldsymbol{r}_1, \boldsymbol{r}_2; \boldsymbol{r}_3, \boldsymbol{r}_4)$, which is introduced in chapter 2.
In terms of $\Gamma(\boldsymbol{r}_1, \boldsymbol{r}_2; \boldsymbol{r}_3, \boldsymbol{r}_4)$, the scattered intensity is given by:

$$\langle I(\boldsymbol{r})\rangle = \frac{c_0\, n}{2}\int d\boldsymbol{r}_1..d\boldsymbol{r}_4\, G(\boldsymbol{r}-\boldsymbol{r}_1)G^*(\boldsymbol{r}-\boldsymbol{r}_3)\langle\Gamma(\boldsymbol{r}_1, \boldsymbol{r}_2; \boldsymbol{r}_3, \boldsymbol{r}_4)\rangle\langle E_{in}(\boldsymbol{r}_2)E^*_{in}(\boldsymbol{r}_4)\rangle, \tag{4.4}$$

where $E_{in}(\boldsymbol{r}\,)$ is an incoming wave and $G(\boldsymbol{r}-\boldsymbol{r}')$ is a Green's function describing the propagation of the intensity from a point $\boldsymbol{r}'$ in the sample to the observation point $\boldsymbol{r}$. The average denotes an average over different

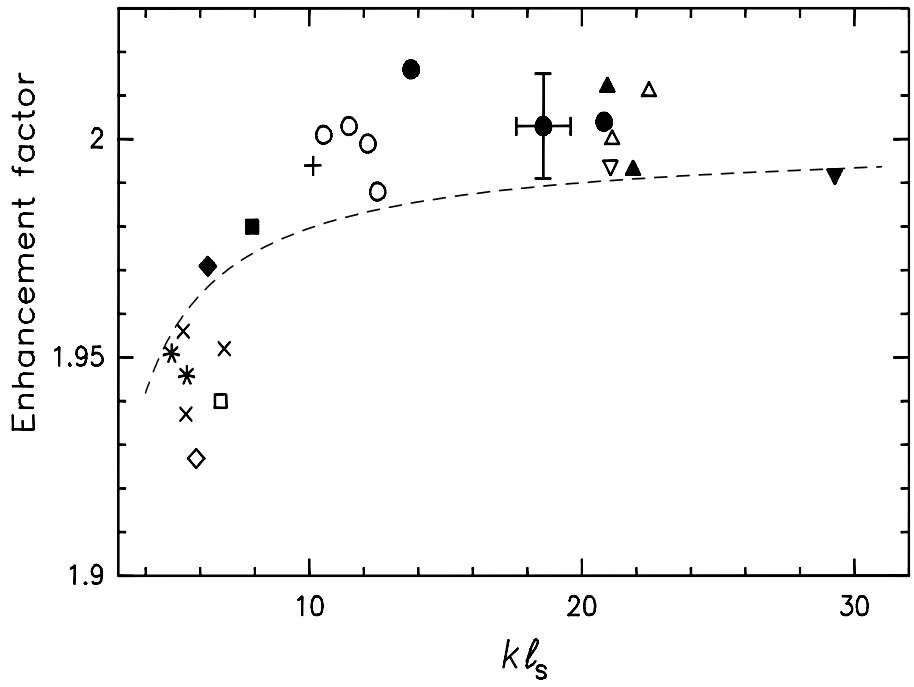

Figure 4.5: *Enhancement factor plotted against $k\ell_s$. Filled symbols correspond to $\lambda_{vac} = 632.8$ nm, whereas others (open and starred) correspond to $\lambda_{vac} = 514.0$ nm. The dashed line is the calculated enhancement factor if recurrent scattering from two vector point scatterers is incorporated.*
Measurements with non index matched interface:
triangle up = $BaSO_4$, triangle down = ZnO, square = TiO_2, diamond = TiO_2 with PMMA.
Measurements with index matched interface:
circle = TiO_2 in 2-methylpentane 2,4-diol, times = TiO_2 (with collodion on glass), star = TiO_2 (thin layer directly on glass), plus = TiO_2 in methanol. The measured enhancement factor is 2.00 ± 0.01 for $k\ell_s \gtrsim 10$ and significantly smaller than 2.00 for smaller values of $k\ell_s$.

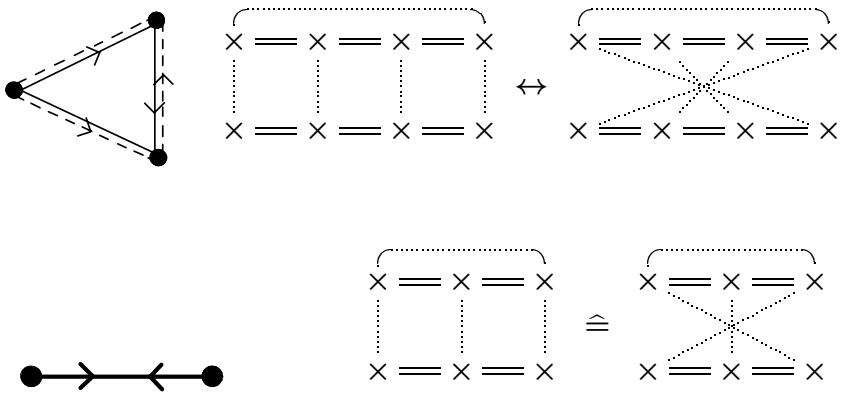

Figure 4.6: *(a) (above) A loop event depicted in real space and an example of a corresponding diagram. The diagram does have a reciprocal counterpart but first and last scatterer are the same. (b) (below) A folded scattering event and an example of a corresponding diagram. Reversing the bottom line does not create a new diagram, which implicates also that first and last scatterer are the same.*

configurations of the medium. The total vertex $\Gamma(\boldsymbol{r}_1, \boldsymbol{r}_2; \boldsymbol{r}_3, \boldsymbol{r}_4)$ contains all information on the scattering properties of the medium. For weak scattering, Γ can be approximated by the sum of ladder and most-crossed diagrams which leads to an enhancement factor of two, if single scattering is eliminated. For strong scattering, recurrent events have to be taken into account. We will calculate explicitly the correction to the enhancement factor to first order in the density, which is due to two particle recurrent scattering events.

As explained in chapter 2, the total vertex can be decomposed into the set of irreducible diagrams $U(\boldsymbol{r}_1, \boldsymbol{r}_2; \boldsymbol{r}_3, \boldsymbol{r}_4)$ and the set of reducible diagrams $\boldsymbol{\mathcal{R}}(\boldsymbol{r}_1, \boldsymbol{r}_2; \boldsymbol{r}_3, \boldsymbol{r}_4)$. In the weak scattering limit, $\boldsymbol{\mathcal{R}}(\boldsymbol{r}_1, \boldsymbol{r}_2; \boldsymbol{r}_3, \boldsymbol{r}_4)$ consists of the 'ladder' diagrams describing long-range diffusion, where long-range means that the distance between first and last scattering event is (much) larger than the scattering mean free path, and $U(\boldsymbol{r}_1, \boldsymbol{r}_2; \boldsymbol{r}_3, \boldsymbol{r}_4)$ consists of all 'most-crossed' diagrams describing the interference leading to coherent backscattering (see section 2.5). $U(\boldsymbol{r}_1, \boldsymbol{r}_2; \boldsymbol{r}_3, \boldsymbol{r}_4)$ also contains single scattering. For strong scattering, the reducible vertex $\boldsymbol{\mathcal{R}}$ is a generalization of the 'ladder' diagrams, describing also long-range diffusion. This implies that $\boldsymbol{\mathcal{R}}$ describes the incoherent background in coherent backscattering.

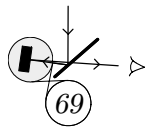

Following Ref. [13], we can distinguish two subclasses of irreducible diagrams. One is the set of irreducible diagrams that can be obtained from $\boldsymbol{\mathcal{R}}$ by reversing the scattering sequence in the bottom line (or top line) of all diagrams in the set $\boldsymbol{\mathcal{R}}$. We call this the set of complementary diagrams $\boldsymbol{\mathcal{C}}(\boldsymbol{r}_1, \boldsymbol{r}_2; \boldsymbol{r}_3, \boldsymbol{r}_4)$:

$$\boldsymbol{\mathcal{C}}(\boldsymbol{r}_1, \boldsymbol{r}_2; \boldsymbol{r}_3, \boldsymbol{r}_4) \equiv \boldsymbol{\mathcal{R}}(\boldsymbol{r}_1, \boldsymbol{r}_2; \boldsymbol{r}_4, \boldsymbol{r}_3). \tag{4.5}$$

The set $\boldsymbol{\mathcal{C}}$ generalizes the set of 'most-crossed' diagrams and describes the interference contribution corresponding to $\boldsymbol{\mathcal{R}}$, which means that $\boldsymbol{\mathcal{C}}$ describes the backscattering cone.

The other subclass of irreducible diagrams is denoted by $\boldsymbol{\mathcal{S}}$, and is simply defined as the total irreducible set minus $\boldsymbol{\mathcal{C}}$. The total vertex is therefore given by:

$$\Gamma = \boldsymbol{\mathcal{R}} + \boldsymbol{\mathcal{C}} + \boldsymbol{\mathcal{S}}. \tag{4.6}$$

The vertex $\boldsymbol{\mathcal{S}}$ is a closed set under the operation carried out in Eq. (4.5). Apart from single scattering, it consists of all (recurrent) diagrams that do not become reducible when reversing the bottom line. Some terms contributing to $\boldsymbol{\mathcal{S}}$ are:

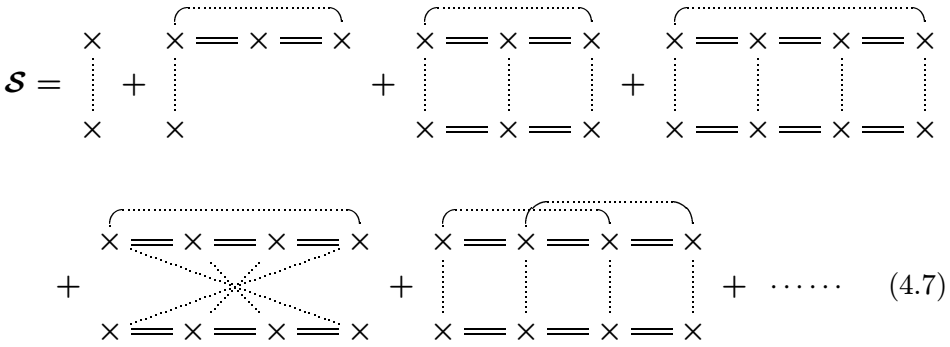

(4.7)

The diagrams in $\boldsymbol{\mathcal{S}}$ are short range on the scale of ℓ_s, that is, the distance between first and last scattering event is much smaller than ℓ_s. The first term in this series is conventional single scattering. The second and third term are 'folded' diagrams as introduced in the previous section, and the fourth and fifth term are 'loop' diagrams. The contribution from terms like the sixth one goes rapidly to zero, if the distance between the particles is increased. The set $\boldsymbol{\mathcal{S}}$ can be interpreted as a generalization of

single scattering. The angular dependence of $\boldsymbol{\mathcal{S}}$ is very weak (like single scattering), so its contribution to the scattered intensity will appear as diffuse background and lower the observed enhancement factor. The observed enhancement factor of the backscattering cone is given by:

$$E = \left. \frac{\gamma_{\mathcal{C}} + \gamma_{\mathcal{R}} + \gamma_{\mathcal{S}}}{\gamma_{\mathcal{R}} + \gamma_{\mathcal{S}}} \right|_{\theta=0}, \tag{4.8}$$

where $\gamma_{\mathcal{S}}$, $\gamma_{\mathcal{C}}$, and $\gamma_{\mathcal{R}}$ are the bistatic coefficients in backscattering corresponding to the vertices $\boldsymbol{\mathcal{S}}$, $\boldsymbol{\mathcal{C}}$, and $\boldsymbol{\mathcal{R}}$. (A bistatic coefficient is defined as the observed scattered flux per solid angle and per unit of observed area of the sample at normalized incident flux.)

4.5.1 Two particle recurrent scattering

We will evaluate Eq. (4.8) for the helicity conserving polarization channel, using vector point scatterers. For an evaluation of the enhancement factor for scalar waves, we refer to Ref. [14]. In the helicity conserving channel at (exact) backscattering, conventional single scattering is zero (for spherical symmetric scatterers) and $\gamma_{\mathcal{S}}$ therefore consists of recurrent scattering only. This means we have to leading order:

$$E = 2 - \left. \frac{\gamma_{\mathcal{S}}}{\gamma_{\mathcal{R}}} \right|_{\theta=0}, \tag{4.9}$$

where $\gamma_{\mathcal{R}}(0) = 1.736$ [15].

To leading order in the density, $\gamma_{\mathcal{S}}$ consists of recurrent scattering between only two scatterers [17]. We will therefore consider a system of two particles and calculate the correction to the total bistatic coefficient of this system due to recurrent scattering, where we average over the positions of both scatterers.

For vector point scatterers, the t-matrix for a *single* particle a, located at $\boldsymbol{r}_a$, is given by [19]:

$$\mathbf{t}_a(\boldsymbol{r}_1, \boldsymbol{r}_2) = \mathbf{t}\, \delta(\boldsymbol{r}_1 - \boldsymbol{r}_a)\delta(\boldsymbol{r}_2 - \boldsymbol{r}_a), \tag{4.10}$$

where $\mathbf{t} = t\, 1$ with:

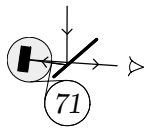

$$t = -\frac{\alpha_0 \, (\omega/c_0)^2}{1 - \omega^2/\omega_0^2 - i\frac{2}{3}\alpha_0(\omega/c_0)^3}. \tag{4.11}$$

Here α_0 is the polarizability of the particle, ω the frequency of the light, and ω_0 the resonance frequency of the scatterer. (Note that this vector t-matrix is a generalization of the scalar t-matrix given in Eq. (2.20).) The scattering cross section for a vector point scatterer, in terms of the t-matrix, is given by: $\sigma_s = \frac{2}{3}(4\pi)^{-1} \, |t(\omega)|^2$.

We define the two particle t-matrix $\mathbf{T}^{(2)}$, as the sum of all possible (amplitude) diagrams for two vector point scatterers:

$\mathbf{T}^{(2)} =$ 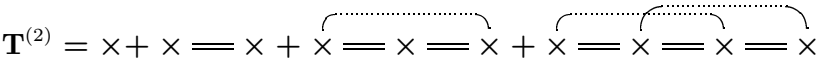 $+ \cdots\cdots,$

(4.12)

where the average over the positions of the scatterers has not yet been performed. In the weak scattering limit, $\mathbf{T}^{(2)}$ is given by the first two terms of this series. In terms of the individual t-matrices $\mathbf{t}_1$ and $\mathbf{t}_2$ of the two scatterers, $\mathbf{T}^{(2)}$ is given by [18]:

$$\mathbf{T}^{(2)}_{ab}(\boldsymbol{r}_1, \boldsymbol{r}_2) = \frac{1}{1 - \mathbf{t}_1\mathbf{t}_2\mathbf{G}^2(\boldsymbol{r}_a - \boldsymbol{r}_b)} \times \tag{4.13}$$

$$\{\mathbf{t}_1\delta(\boldsymbol{r}_1 - \boldsymbol{r}_a)\delta(\boldsymbol{r}_2 - \boldsymbol{r}_a) + \mathbf{t}_2\delta(\boldsymbol{r}_1 - \boldsymbol{r}_b)\delta(\boldsymbol{r}_2 - \boldsymbol{r}_b)$$

$$+ \mathbf{t}_1\mathbf{t}_2\mathbf{G}(\boldsymbol{r}_a - \boldsymbol{r}_b)[\delta(\boldsymbol{r}_1 - \boldsymbol{r}_a)\delta(\boldsymbol{r}_2 - \boldsymbol{r}_b) + \delta(\boldsymbol{r}_1 - \boldsymbol{r}_b)\delta(\boldsymbol{r}_2 - \boldsymbol{r}_a)]\},$$

where $\boldsymbol{r}_a$ and $\boldsymbol{r}_b$ are the positions of the scatterers. The above expression is a closed form for the two particle t-matrix $\mathbf{T}^{(2)}$. The series expansion of the prefactor:

$$\frac{1}{1 - \mathbf{t}_1\mathbf{t}_2\mathbf{G}^2(\boldsymbol{r}_a - \boldsymbol{r}_b)} = 1 + \mathbf{t}_1\mathbf{t}_2\mathbf{G}^2(\boldsymbol{r}_a - \boldsymbol{r}_b) + (\mathbf{t}_1\mathbf{t}_2\mathbf{G}^2(\boldsymbol{r}_a - \boldsymbol{r}_b))^2 + \cdots,$$

generates again the diagrammatic expansion of $\mathbf{T}^{(2)}$ as given by Eq. (4.12). To first order this prefactor is 1. In that case, the first and second term of Eq. (4.13) describe single scattering by either one of the particles and

the third term describes double scattering. The higher order terms of the prefactor generate all recurrent diagrams in Eq. (4.12).

The vector Green's function $\mathbf{G}(\boldsymbol{r}_a - \boldsymbol{r}_b)$, which depends only on the relative positions of both scatterers $\boldsymbol{r} = \boldsymbol{r}_a - \boldsymbol{r}_b$, can be decomposed into a longitudinal part $Q(r)$ and a transverse part $P(r)$:

$$\mathbf{G}(\boldsymbol{r}) = P(kr)\boldsymbol{\Delta}_r + Q(kr)\hat{\boldsymbol{r}}\hat{\boldsymbol{r}}, \tag{4.14}$$

with P and Q given by [18]:

$$P(y) = \frac{k}{4\pi}\left(-1 + \frac{1}{iy} + \frac{1}{y^2}\right)\frac{e^{iy}}{y} \tag{4.15}$$

and

$$Q(y) = -2\frac{k}{4\pi}\left(\frac{1}{iy} + \frac{1}{y^2}\right)\frac{e^{iy}}{y}, \tag{4.16}$$

where $y = k\,r$, and the matrices $\boldsymbol{\Delta}_r$ and $\hat{\boldsymbol{r}}\hat{\boldsymbol{r}}$ are projections respectively to and along the direction of $\boldsymbol{r}$.

To calculate the two particle bistatic coefficient, we need the total two particle vertex $\mathbf{\Gamma}^{(2)}$, which is the square of the two particle t-matrix:

$$\mathbf{\Gamma}^{(2)}_{ab}(\boldsymbol{r}_1, \boldsymbol{r}_2, \boldsymbol{r}_3, \boldsymbol{r}_4) = \mathbf{T}^{(2)}_{ab}(\boldsymbol{r}_1, \boldsymbol{r}_2)\,\mathbf{T}^{(2)*}_{ab}(\boldsymbol{r}_3, \boldsymbol{r}_4). \tag{4.17}$$

With Eq. (4.13), we have a closed expression for $\mathbf{\Gamma}^{(2)}$. Some terms contributing to $\mathbf{\Gamma}^{(2)}$ are:

$\mathbf{\Gamma}^{(2)} =$ 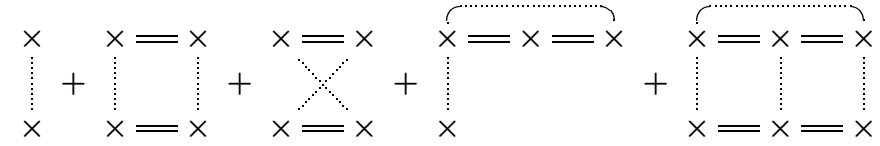 $+ \cdots$

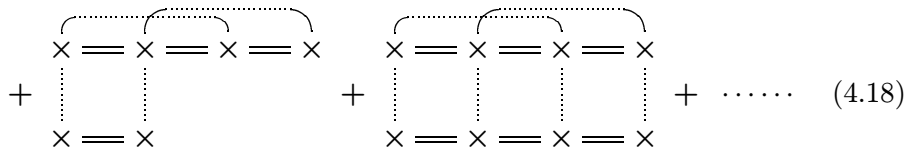

(4.18)

The first term is single scattering. The second and third term are the conventional two particle ladder ($\boldsymbol{\mathcal{R}}^{(2)}$) and most-crossed ($\boldsymbol{\mathcal{C}}^{(2)}$) diagrams. The other terms are the recurrent diagrams in $\boldsymbol{\mathcal{S}}^{(2)}$. The single scattering term is zero at backscattering in the helicity conserving polarization channel. To calculate $\gamma_{\mathcal{S}}$ for a system of N particles, we subtract $\boldsymbol{\mathcal{R}}^{(2)}$ and $\boldsymbol{\mathcal{C}}^{(2)}$ from $\boldsymbol{\Gamma}^{(2)}$ and calculate the two particle recurrent bistatic coefficient. Subsequently, we average over the positions $\boldsymbol{r}_a$ and $\boldsymbol{r}_b$ of the two scatterers and multiply by the total number of possible pairs of scatterers: $\frac{1}{2}N(N-1)$. In backscattering, using the definition of a bistatic coefficient (2.34), this leads to:

$$\gamma_{\mathcal{S}} = \tfrac{1}{2}N(N-1)\frac{4\pi r^2}{A}\iint\frac{d\boldsymbol{r}_a}{V}\frac{d\boldsymbol{r}_b}{V}\iint d\boldsymbol{r}_1..d\boldsymbol{r}_4 \tag{4.19}$$

$$\mathbf{G}(\boldsymbol{r}-\boldsymbol{r}_1)\mathbf{G}^*(\boldsymbol{r}-\boldsymbol{r}_3)\,\boldsymbol{e}_1\boldsymbol{e}_3^*\cdot\boldsymbol{\mathcal{S}}^{(2)}_{ab}(\boldsymbol{r}_1,\boldsymbol{r}_2,\boldsymbol{r}_3,\boldsymbol{r}_4)\cdot\boldsymbol{e}_2\boldsymbol{e}_4^*\,E_{in}(\boldsymbol{r}_2)E^*_{in}(\boldsymbol{r}_4),$$

with $\boldsymbol{\mathcal{S}}^{(2)} = \boldsymbol{\Gamma}^{(2)} - \boldsymbol{\mathcal{R}}^{(2)} - \boldsymbol{\mathcal{C}}^{(2)}$, and A the illuminated area of the sample surface. Here $\boldsymbol{e}_2$ and $\boldsymbol{e}_4$ are the incoming polarization vectors and $\boldsymbol{e}_1$ and $\boldsymbol{e}_3$ the outgoing polarization vectors. For the helicity conserving polarization channel at exact backscattering we have:

$$\boldsymbol{e}_1 = \boldsymbol{e}_2 = \boldsymbol{e}_3 = \boldsymbol{e}_4 := \boldsymbol{e} = \frac{\hat{\boldsymbol{x}} + i\hat{\boldsymbol{y}}}{\sqrt{2}}. \tag{4.20}$$

For the incoming wave, we take a (damped) plane wave along the z-axis:

$$E_{in}(\boldsymbol{r}\,) = e^{(ik\,-\,\frac{1}{2}\kappa_e)\,z}, \tag{4.21}$$

with κ_e the extinction coefficient in the medium. For non absorbing particles we have $\kappa_e = \ell_s^{-1}$. At (exact) backscattering with $\boldsymbol{r}$ far away from

the medium, the longitudinal component of $\mathbf{G}(\boldsymbol{r}-\boldsymbol{r}_1)$ can be neglected so $\mathbf{G}(\boldsymbol{r}-\boldsymbol{r}_1)$ is given by:

$$\mathbf{G}(\boldsymbol{r}-\boldsymbol{r}_1) = G(\boldsymbol{r}-\boldsymbol{r}_1)\,\boldsymbol{\Delta}_r \tag{4.22}$$

where $G(\boldsymbol{r}-\boldsymbol{r}_1)$ can be approximated by (see Eq. (2.36)):

$$G(\boldsymbol{r}-\boldsymbol{r}_1) \simeq -\frac{e^{ikr}}{4\pi r} e^{-ik\hat{\boldsymbol{z}}\cdot\boldsymbol{r}_1 - \frac{1}{2}\kappa_e z_1}. \tag{4.23}$$

Because $\boldsymbol{\mathcal{S}}$ is short range we can put $\boldsymbol{r}_1 \simeq \boldsymbol{r}_2 \simeq \boldsymbol{r}_3 \simeq \boldsymbol{r}_4$. After performing the integration over $\boldsymbol{r}_1..\boldsymbol{r}_4$ we find:

$$\gamma_{\mathcal{S}} = \frac{N^2}{2V^2}\,\frac{1}{4\pi A}\int d\boldsymbol{r}_a e^{-2\kappa_e z_a}\int d(\boldsymbol{r}_a-\boldsymbol{r}_b)\;\boldsymbol{e}\boldsymbol{e}^*\cdot\boldsymbol{\mathcal{S}}^{(2)}(\boldsymbol{r}_a-\boldsymbol{r}_b)\cdot\boldsymbol{e}\boldsymbol{e}^*\,, \tag{4.24}$$

where we have used that $\frac{1}{2}N(N-1) \simeq \frac{1}{2}N^2$ because N is very large. After performing the integral over $\boldsymbol{r}_a$ and taking the limit $N\to\infty$, $V\to\infty$, with $N/V \to n$, we find the bistatic coefficient describing two particle recurrent scattering:

$$\gamma_{\mathcal{S}} = \frac{3\,n}{8\,|\,t\,|^2}\int d\boldsymbol{r}\;\boldsymbol{e}\boldsymbol{e}^*\cdot\boldsymbol{\mathcal{S}}^{(2)}(\boldsymbol{r})\cdot\boldsymbol{e}\boldsymbol{e}^*\,, \tag{4.25}$$

where we have used that $\ell_s = 1/(n\sigma_s) = 6\pi/(n|t|^2)$. If we divide the above expression by $\gamma_{\mathcal{R}}$, we find the first order density correction to the enhancement factor in going to strong scattering, and [according to Eq. (4.9)] the enhancement factor itself becomes:

$$E = 2 - n\;\frac{3}{\gamma_{\mathcal{R}}(0)\;\;8|\,t\,|^2}\int d\boldsymbol{r}\;\boldsymbol{e}\boldsymbol{e}^*\cdot\boldsymbol{\mathcal{S}}^{(2)}(\boldsymbol{r})\;\cdot\boldsymbol{e}\boldsymbol{e}^*. \tag{4.26}$$

The integral over the separation vector $\boldsymbol{r}$ can be performed numerically. Furthermore, because our samples are strongly polydisperse, we average t_1 and t_2 independently over a frequency window which is large compared to the width of the resonance. The enhancement factor calculated with Eq. (4.26), is plotted in Fig. 4.5 as a dashed line. We see that the calculation confirms our interpretation that recurrent scattering manifests itself as a reduction of the enhancement factor for $k\ell_s \lesssim 10$.

References and notes

[1] P.W. Anderson, Phys. Rev. **109**, 1492 (1958); *Anderson Localization*, edited by T. Ando and H. Fukuyama, in *Springer proceedings in physics* **28** (Springer, Berlin, 1988).

[2] *Analogies in Optics and Micro Electronics*, edited by W. van Haeringen and D. Lenstra (Kluwer, Dordrecht, 1990).

[3] D. Vollhardt and P. Wölfle, in *Electronic Phase Transitions*, *Modern Problems in Condensed Matter Sciences* **32**, edited by W. Hanke and Yu. V. Kopaev (North-Holland, Amsterdam, 1992).

[4] B.L. Altshuler, A.G. Aronov, D.E. Khmel'nitskii, and A.I. Larkin, in *Quantum Theory of Solids*, edited by I.M. Lifshitz (MIR Publishers, Moskva, 1983).

[5] A.F. Ioffe and A.R. Regel, Progr. Semiconductors **4**, 237 (1960); N.F. Mott, *Metal-Insulator Transitions* (Taylor and Francis, London, 1974).

[6] The TiO_2 powders were obtained from Sachtleben Chemie, Duisburg, and are of the type *RCL 6G rutil* TiO_2.

[7] Spectraflect^{TM} is a trademark of Labsphere, Inc. North Sutton, United States.

[8] W is the full width at half maximum. If W is varied, the backscattering cone scales linearly along the x-axis.

[9] M.B. van der Mark, M.P. van Albada, and A. Lagendijk, Phys. Rev. B **37**, 3575 (1988); P.E. Wolf, G. Maret, E. Akkermans, and R. Maynard, J. Phys. France **49**, 63 (1988); further developed to handle semi-infinite slabs in: E.E. Gorodnichev, S.L. Dudarev, and D.B. Rogozkin, Phys. Lett. A **144**, 48 (1990).

[10] A. Lagendijk, B. Vreeker, and P. de Vries, Phys. Lett. A **136**, 81 (1989); J.X. Zhu, D.J. Pine, and D.A. Weitz, Phys. Rev. A **44**, 3948 (1991).

[11] In order to be able to compare the data with the calculation on two particle recurrent scattering (presented in section 4.5), we have to assume that $\ell = \ell_s$. The mean free path induced from the cone width is the transport mean free path and not the scattering mean free path. If the particles scatter anisotropically, ℓ will be larger than ℓ_s. In the last section, we will see that despite this assumption, the agreement between data and theory is good.

[12] P.N. den Outer and A. Lagendijk, Opt. Comm. **103**, 169 (1993).

[13] D. Vollhardt and P. Wölfle, Phys. Rev. B **22**, 4666 (1980).

[14] B.A. van Tiggelen, D.S. Wiersma, and A. Lagendijk, Europhys. Lett. **30**, 1 (1995).

[15] The value was derived using $\gamma_{r_0}^{++} + \gamma_{r_0}^{+-} + \gamma_{s_0}^{+-} = 4 \times 1.1471$ by Table 54 of Ref. [16], treating single and double scattering exactly and the rest

in the diffusion approximation (see E. Akkermans and R. Maynard, J. Phys. (Paris) Lett. **46**, 1045 (1985); M.P. van Albada and A. Lagendijk, Phys. Rev. B **36**, 2353 (1987)).
[16] H.C. van de Hulst, *Multiple Light Scattering* (Dover, New York, 1980).
[17] B.A. van Tiggelen and A. Lagendijk, Phys. Rev. **B** 22, 16729 (1994).
[18] B.A. van Tiggelen, A. Lagendijk, and A. Tip, J. Phys. C **2**, 7653 (1990).
[19] H.J. Dorren and A. Tip, J. Math. Phys. **32**, 3060 (1991); Th.M. Nieuwenhuizen, A. Lagendijk, and B.A. van Tiggelen, Phys. Lett. A **169**, 191 (1993).

Chapter 5

Amplifying random media

5.1 Introduction

This chapter is concerned with the experimental considerations on creating disordered media that exhibit optical amplification. We will show how to create a medium in which light waves are both multiply scattered and amplified in between or during the scattering events. Optical amplification is obtained through stimulated emission in a laser material. To introduce scattering in such a material, one can grind a laser crystal like ruby or Ti:sapphire. Another option is to use latex microparticle combined with laser dye, either by suspending the particles in a dye solution or by doping the particles with the dye.

To obtain amplification, the laser material must be brought in inversion. This excitation is called pumping and can for instance be done optically with intense laser light. One encounters several problems however, that do not occur in conventional laser systems. In a conventional laser system, the pump light is absorbed by the laser material, which is thereby brought into the desired excited state. If scattering is introduced in such a laser material, the pump light will be both scattered and absorbed. If the scattering is much stronger than the absorption, most of the pump light is scattered out of the system without being absorbed. We will look into this problem and discuss pumping geometries that can be used to increase the pumping efficiency.

The intensities required to excite a laser material are high, which is a complicating factor in the experiments. With a continuous wave (CW) laser, they can be obtained only if the light is focused to a diameter of a few tens of micro meters, and the resulting excited volume will therefore be very small. If we wish to excite a larger volume, we are forced to use

pulsed pump light. This means that our disordered laser material will not amplify continuously, but only during some limited time window (ranging from 10 ns to several ms), at a certain repetition rate.

In this chapter we will go into the various possibilities of creating amplifying random media, and show some results on powdered laser crystals.

5.1.1 Relevant length scales

In an amplifying random medium, light waves are both multiply scattered and amplified. The relevant length scales that describe the scattering process are the scattering mean free path ℓ_s and transport mean free path ℓ, as they were defined in chapter 2. To describe the amplification process, we define two new length scales: the gain length ℓ_g and amplification length ℓ_{amp}. The gain length is defined as the path length over which the intensity is amplified by a factor e^{+1}. The amplification length is defined as the (rms) average distance between the begin and end points for paths of length ℓ_g:

$$\ell_{amp} \equiv \sqrt{\frac{\ell\,\ell_g}{3}}. \tag{5.1}$$

Without scattering, ℓ_{amp} is equal to ℓ_g. The amplification length ℓ_{amp} and gain length ℓ_g are the analogues of the absorption length ℓ_{abs} and the inelastic length ℓ_i that describe absorption.

For an amplifying medium one can define a critical volume above which the system becomes unstable. The average total amplification for a wave inside the sample increases with the volume of the sample, whereas the loss through the boundaries is proportional to the boundary surface. The critical volume V_{cr} is defined as the volume at which gain equals loss. Above the critical volume, the intensity inside the medium diverges.

We will study samples with a slab geometry. In that case, one can define a critical thickness L_{cr} instead of a critical volume, above which the intensity diverges. The critical thickness is given by (see section 6.3.5):

$$L_{cr} = \pi\ell_{amp} = \pi\sqrt{\frac{\ell\,\ell_g}{3}}. \tag{5.2}$$

Note that L_{cr} is proportional to ℓ_{amp}.

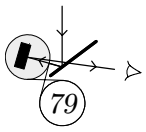

5.2 Realizing disordered media with gain

5.2.1 Choice of the laser material

An important factor in realizing an amplifying random medium is the choice of the laser material. We will consider laser materials which are optically pumped. Most laser material can be described as a three or four level system. The material is excited optically to some high energy level that decays rapidly to a metastable state. The laser transition occurs from this metastable state to the ground state or to a short lived (and thereby nearly unpopulated) state above the ground state. (See also section 1.2.)

The relevant cross sections are the absorption cross section σ_{abs}^{P} of the pump transition and the stimulated emission cross section σ_{em}^{L} of the laser transition. The emission cross section σ_{em}^{L}, determines the maximum gain of the system and should therefore be as large as possible. Amplification is achieved only when the gain at the emission wavelength is larger than the absorption at this wavelength. The advantage of a four level system is that the ground state of the laser transition is almost unpopulated, so the absorption at the emission wavelength in principle can be very small. For an amplifying random medium, it is more important that σ_{abs}^{P} is large than it is for regular laser systems. The absorption cross section determines the inelastic length ℓ_i for the pump light. If ℓ_i is much larger than the transport mean free path ℓ, most pump light is scattered without being absorbed. We come back to this problem in the next section. In Table 5.1, we have listed σ_{abs}^{P} and σ_{em}^{L} for some laser materials. Also listed is the ratio of the absorption coefficient to the maximum gain coefficient at the peak emission wavelength.

Another important parameter is the excited state lifetime τ_e. Because we have to use pulsed pump light, the lifetime of the overall gain in the system will be limited by τ_e. If the excited part of the medium is much smaller than the critical volume V_{cr}, it will be equal to τ_e. Close to the critical volume, the lifetime of the overall gain is much shorter than τ_e, because spontaneously emitted light will be largely amplified, thereby de-exciting the system. We come back to these effects in section 5.3.

From Table 5.1, we see that the lifetime of the excited state for ruby is very large. Unfortunately, this material is a three level system and therefore the absorption at the emission wavelength is large ($\kappa_{abs}/\kappa_g = 0.5$). Laser dye like Rhodamine 6G has the advantage of a very large absorption and emission cross section. However, experiments with dye have to be performed with picosecond time resolution due to the very short lifetime of the excited state. Nd:YAG has a reasonably large emission cross section and

material	λ_{em} (nm)	λ_{abs} (nm)	σ_{em} (m^2)	σ_{abs} (m^2)	τ_e (s)	κ_{abs}/κ_g atλ_{em}^{max}
latex spheres with R6G	570-630	460-540	$2.5{\cdot}10^{-20}$	$1.6{\cdot}10^{-20}$	$5.0{\cdot}10^{-9}$	$6.8{\cdot}10^{-6}$
Ti:Al_2O_3 (Ti:sapphire)	660-1100 $\lambda_{max} \simeq$780	450-580	$3.0{\cdot}10^{-23}$	$3.0{\cdot}10^{-24}$	$3.2{\cdot}10^{-6}$	$2.5{\cdot}10^{-3}$
Cr:Al_2O_3 (ruby)	692.9 and 694.3	380-430; 520-590	$2.5{\cdot}10^{-24}$	$1.2{\cdot}10^{-24}$	$3.0{\cdot}10^{-3}$	0.5
Nd:YAG	1064	visible [1]	$6.5{\cdot}10^{-23}$	$3.6{\cdot}10^{-24}$	$2.3{\cdot}10^{-4}$	$< 10^{-4}$
Nd:Glass	1054	visible [2]	$3.0{\cdot}10^{-24}$	$2.3{\cdot}10^{-24}$	$3.3{\cdot}10^{-4}$	$< 10^{-4}$

Table 5.1: *Maximum emission cross section σ_{em}^L of the laser transition, maximum absorption cross section σ_{abs}^P of the pump transition, and the excited state lifetime τ_e of various laser materials. Also listed are the emission and absorption wavelengths. (Note that if a range is specified, the listed values denote the wavelengths at which the cross sections are 10 % of their maximum value.) All materials are in principle a four level system, apart from ruby which is a three level system. In the last column, the ratio of the absorption coefficient to the maximum gain coefficient at the peak emission wavelength is given. R6G is an abbreviation for Rhodamine 6G.*
[1] Complicated absorption spectrum that covers the visible spectrum, containing many narrow peaks. The listed absorption cross section is the maximum value at $\lambda = 810$ nm.
[2] Same as [1], however the peaks are much broader ($\sim$ 20 nm).

lifetime and is therefore a good option, although the experiments are then to be performed in the infrared. A good alternative is Ti:sapphire because it has a reasonably large emission cross section and excited state lifetime, and its emission wavelengths are in the visible regime. We have performed experiments both with ruby and Ti:sapphire.

5.2.2 Optical excitation

In a disordered laser material, optical excitation is more difficult than in regular lasers, due to scattering of the pump light. We are interested in systems with a transport mean free path as small as possible, say at least smaller than 100 μm. To determine the fraction of pump light which is

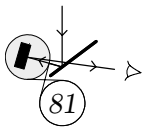

actually used to pump the medium, we have performed Monte-Carlo simulations on powdered laser crystals. The simplest pumping geometry that we used, was a slab in the xy-plane illuminated by a plane wave from $z = -\infty$. The depth dependence of the incoming beam in the slab was an exponentially decaying function: $\exp(\kappa_e z)$. The z-coordinate of each injected photon [1] was monitored while it performed a (3 dimensional) random walk through the slab. Absorption was taken into account by giving the light a probability x_{abs} to be absorbed at every scattering event. The absorption probability is given by:

$$x_{abs} \equiv \frac{n_0(z)}{n} \frac{\ell}{\ell_i}, \tag{5.3}$$

with ℓ and ℓ_i respectively the transport and inelastic mean free path. Here n is the total concentration of ions and $n_0(z)$ is the *local* concentration of ions in the ground state.

The fraction of the light that is absorbed before it leaves the sample again through one of its interfaces, depends strongly on the ratio ℓ_i/ℓ. In Fig. 5.1 we have plotted this fraction versus ℓ_i/ℓ for a slab with a thickness of $20\,\ell$, calculated in Monte-Carlo simulations on different pump geometries. The incident pump energy in the simulation was chosen such that at 100 % efficiency, the sample would just be completely excited. In an experimental situation, the pump energy will usually be of this order. If the incident energy is chosen much larger, the pump efficiency becomes somewhat smaller due to depletion.

For large values of ℓ_i/ℓ, the efficiency decreases with increasing ℓ_i/ℓ. For small values of ℓ_i/ℓ, the pump efficiency is independent of ℓ_i/ℓ. In that case, the first part of the pump pulse is completely absorbed, thereby creating a thin layer that is 100 % excited. Subsequent pump light will be scattered in this layer and absorbed in a next layer. This way a region of 100 % excitation grows, starting from the sample interface. Further decreasing ℓ_i/ℓ does not increase the efficiency of this process.

If the slab is pumped from one side, the excitation level is inhomogeneous. (See also section 5.3.) An (almost) homogeneous excitation can be obtained by pumping the slab from both sides, which also results in a higher pump efficiency for small ℓ_i/ℓ (see Fig. 5.1).

A solution to enlarge the pump efficiency at large values of ℓ_i/ℓ, is to change the pumping geometry such that the scattered light is reinjected into the sample. An example of a very efficient geometry is depicted in Fig. 5.2. The sample is placed on a dichroic mirror, in the focal region of a

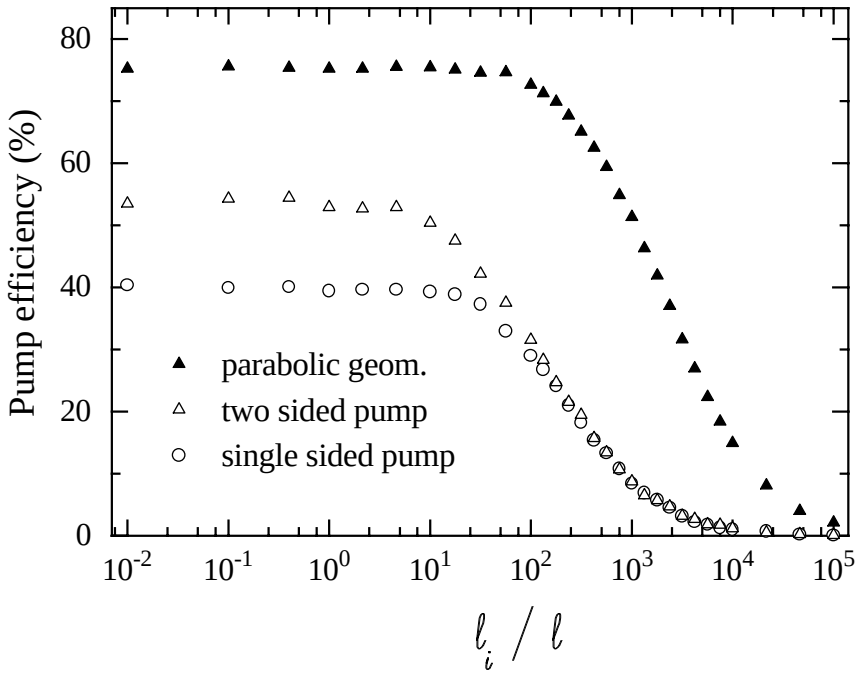

Figure 5.1: *Pump efficiency versus ℓ_i/ℓ for different pump geometries, calculated in a Monte-Carlo simulation. The medium has a slab geometry with optical thickness 20. The efficiency increases by a factor 2 - 5 with the parabolic geometry described in Fig. 5.2.*

parabolic mirror. A small hole in the parabolic mirror allows to illuminate the sample with a (focused) pump beam. The scattered pump light returns to the sample by reflecting on the parabolic and the flat mirror, as shown. By choosing the flat mirror transparent for the probe (emission) wavelength, a probe beam can reach the sample through this mirror. Note that also the probe transmitted through the sample (although directionally scrambled) can be monitored. The results of Monte-Carlo simulations on this pumping geometry are also shown in Fig. 5.1. The reflection coefficient of the flat and parabolic mirror were chosen respectively 99 % and 97 %, which are realistic values. The focal length of the parabolic mirror was $f = 1$ cm. The hole in the parabolic mirror was chosen 1 mm and the sample diameter 5 mm. We see from Fig. 5.1, that such a geometry could increase the pumping efficiency with a factor 2 - 5.

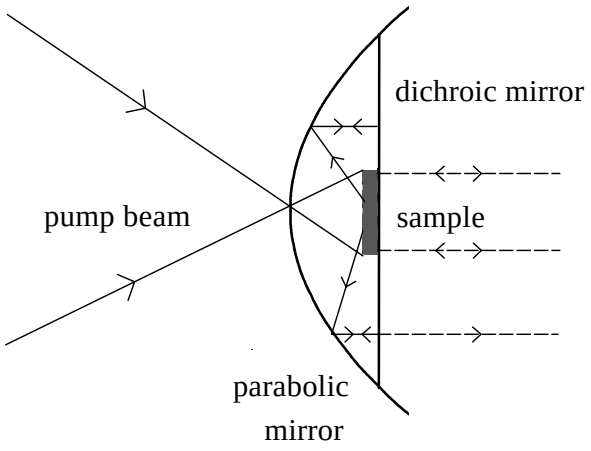

Figure 5.2: *Efficient geometry to pump a disordered laser material. The sample is mounted on a dichroic mirror which is placed in the focal plane of a parabolic mirror. The pump light is incident through a small (e.g. 1 mm) hole in the parabolic mirror. Pump light that is scattered from the sample is backreflected to the sample surface via the parabolic and the dichroic mirror. The dichroic mirror is transparent for the probe (emission) wavelength. Note that the scattered probe light from both front and rear sample surface can be monitored (Dashed lines).*

In Table 5.2, we have listed the value of ℓ_i/ℓ for a few laser materials, assuming a transport mean free path of $\ell = 20$ μm, and the resulting pump efficiencies for single sided pumping. For latex spheres with Rhodamine 6G and highly doped Cr:Al_2O_3, the pump efficiency equals its maximum value for this pump geometry. However, for instance for powdered Ti:sapphire the efficiency is lower than 10 %. Of course the efficiency can be raised by enlarging ℓ (e.g. by suspending the powdered Ti:sapphire in water), however we wish to keep the scattering as strong as possible.

In Table 5.2, we have also listed the pump pulse energy required for an excitation level of 100 %, for a sample of thickness 0.4 mm and diameter 4 mm, which for $\ell = 20$ μm, corresponds to a reasonably large sample of optical thickness 20 and optical diameter 200. The listed pulse energies take into account the pump efficiency for a simple single sided pumping geometry.

material	ion/mol. conc. (10^{25} m^{-3})	ℓ_i (m)	ℓ_i/ℓ	pump eff.	pulse energy (mJ)
latex spheres with R6G	1.3	$5.0{\cdot}10^{-5}$	2.5	40 %	6.0
Ti:Al_2O_3 (0.15%)	4.7	$2.3{\cdot}10^{-2}$	$1.17{\cdot}10^{3}$	7.7 %	351
Cr:Al_2O_3 (0.05%)	1.6	$2.5{\cdot}10^{-2}$	$1.23{\cdot}10^{3}$	7.4 %	122
Cr:Al_2O_3 (2.1%)	67	$5.9{\cdot}10^{-4}$	$2.92{\cdot}10^{1}$	38 %	992
Nd:YAG (1.1%)	14	$2.0{\cdot}10^{-3}$	$1.0{\cdot}10^{2}$	29 %	269
Nd:Glass (5.0%)	48	$0.9{\cdot}10^{-3}$	$4.5{\cdot}10^{1}$	35 %	771

Table 5.2: *Pump efficiency for some laser materials assuming a transport mean free path ℓ = 20 μm. The inelastic mean free path ℓ_i was calculated from the maximum absorption cross section assuming a volume fraction of 30 % powdered laser crystal or 10 % latex spheres with R6G. Also listed is the required pump energy to fully excite a slab of thickness 0.4 mm and diameter 4.0 mm, taking into account the pump efficiency. The higher internal energy density in the scatterers compared to their environment [2,3], is not taken into account. This would yield smaller values of ℓ_i (by a factor of 2 - 4) which would result in more efficient pumping.*

5.2.3 Experimentally realized gain levels

We have performed experiments on ruby and Ti:sapphire because of their reasonably large emission cross section and excited state lifetime. To obtain the required pulse energy to excite these materials, we have used a frequency doubled Q-switched Nd:YAG laser with a pulse duration of 14 ns. The maximum pulse energy incident on the sample was about 200 mJ, which for a beam diameter of 5 mm corresponds to a maximum incident intensity of $7.3{\cdot}10^{11}$ J/m^{2}s. A low intensity probe pulse was incident at a time delay of 14 ns after the pump pulse, on the same side of the sample. (Probe pulse energy 40 μJ, pulse duration 14 ns, and beam diameter 5 mm. Probe and pump beam overlap on the sample surface.) The temporal profile of the transmitted and backscattered intensity was recorded. The overall amplification in transmission and in backscattering was determined by comparing the probe intensity with and without pump light. To avoid artifacts from cumulative heating of the sample after many pump pulses or other long term effects, the repetition rate of the probe was chosen twice as high at

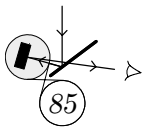

the pump repetition rate, so every second probe shot could serve as a reference measurement without pump light.

In Table 5.3, the results are listed for various ruby and Ti:sapphire samples. The samples have a slab geometry with thickness 1 mm. We found that for dry powdered ruby sample, single shot heating poses a problem. Already at modest pump intensities ($3.6{\cdot}10^{10}$ J/m^{2}s corresponding to 10 mJ in 14 ns on an area of 20 mm^2), dark burns occur on the sample surface after a few pump pulses. By suspending the ruby powder in glycerol, this problem is partly solved, however in that case at high intensities, gas bubbles occur in the sample. The overall gain which is observed with ruby is very small (2-4 %). Furthermore, because ruby is a three level system with a large absorption at the laser wavelength, the observed overall gain is merely reduced absorption. For powdered Ti:sapphire, the problems with heating are much smaller. Only for the dry Ti:sapphire powders at high intensities ($6.0{\cdot}10^{11}$ J/m^{2}s corresponding to 165 mJ in 14 ns on an area of 20 mm^2), we see a small structural change of the sample surface after a few hours. The colour of the sample remains unchanged. The structural change is just a redistribution of the powder in the sample cell. For Ti:sapphire powders in water we encounter no problems from heating of the sample. The obtained overall gain for Ti:sapphire samples is high both in reflection (> 100 %) and in transmission ($\simeq 40$ %). Also listed in Table 5.3, is the calculated gain length and the theoretical shortest gain length in the sample for an excitation level of 100 %. The gain length was calculated from the overall gain in backscattering using equation 6.14.

The above results show that it is possible to realize an amplifying random medium, on which scattering experiments can be performed. Using powdered Ti:sapphire, average gain lengths in the order of 10 mm can be obtained in a large (several mm^3) and reasonably strongly scattering ($\ell \lesssim 20$ μm) medium. Experiments have to be performed however with pulsed light at a low repetition rate.

5.3 Calculations on diffusion with gain

The lifetime of the average gain, is determined by the spontaneous emission rate and the ratio of the size of the excited volume in the sample to the critical volume V_{cr}. If the sample size is close to V_{cr}, spontaneously emitted light will be largely amplified thereby de-exciting the system rapidly. To incorporate this effect in a theoretical description of the system, we have to take into account the time and position dependence of the excitation level and of all relevant intensities.

transmission data						
material	in	L μm	ℓ μm	pump int. J/m^{2}s	overall gain	remarks
ruby	air	200	$\simeq$ 10	$3.6{\cdot}10^{10}$	-	dark burns
ruby	glycerol	100	$\simeq$ 40	$3.6{\cdot}10^{11}$	2-4 %	
ruby	glycerol	100	$\simeq$ 40	$7.3{\cdot}10^{11}$	-	gas bubbles
Ti:sapphire	air	100	$\simeq$ 10	$1.6{\cdot}10^{11}$	16-18 %	
Ti:sapphire	air	100	$\simeq$ 10	$2.5{\cdot}10^{11}$	25-31 %	
Ti:sapphire	air	100	$\simeq$ 10	$3.6{\cdot}10^{11}$	$\simeq$ 30 %	
Ti:sapphire	air	175	$\simeq$ 10	$2.1{\cdot}10^{11}$	$\simeq$ 38 %	
Ti:sapphire	air	175	$\simeq$ 10	$3.0{\cdot}10^{11}$	$\simeq$ 42 %	
Ti:sapphire	air	100	$\simeq$ 10	$6.0{\cdot}10^{11}$	-	struc. change

backscattering data							
material	in	L μm	ℓ μm	pump int. J/m^{2}s	overall gain	ℓ_g mm	ℓ_g^{min} mm
Ti:sapphire	water	1000	40	$6.0{\cdot}10^{11}$	36 %	13.9	2.3
Ti:sapphire	water	1000	40	$6.9{\cdot}10^{11}$	71 %	11.2	2.3
Ti:sapphire	water	1000	28	$6.5{\cdot}10^{11}$	115 %	13.4	2.3
Ti:sapphire	air [1]	1000	18	$6.5{\cdot}10^{11}$	155 %	18.6	2.3
Ti:sapphire	air [1]	1000	18	$6.9{\cdot}10^{11}$	134 %	18.5	2.3

Table 5.3: *Results of transmission and backscattering measurements on the overall gain from powdered ruby (2.1 wt% Cr_2O_3) and powdered Ti:sapphire (0.15 wt% Ti_2O_3). Pump wavelength 532 nm, pulse duration 14 ns. The ruby/air samples get burnt already at modest pump intensities. The ruby/glycerol samples show air bubbles at high intensities. The gain of 2-4 % observed for ruby is in reality reduced absorption. With the Ti:sapphire, a large gain is obtained without damage to the sample. Only at the highest pump intensities, a slight structural change is visible for the Ti:sapphire/air sample.*

[1] The medium consists of wet Ti:sapphire particles surrounded by air, and ℓ is therefore somewhat larger than for a completely dry Ti:sapphire powder.

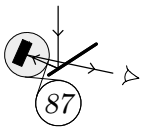

If we assume the propagation of light in the sample to be diffusive, we can describe the time and position-dependent energy density of both the pump and probe light by a diffusion equation with an absorption respectively gain term that depends on the local excitation of the sample. The time and position-dependent excitation level is described by the rate equations of the laser material. Apart from the probe and pump light, we have to account for amplified spontaneous emission (ASE). We denote the energy density of the (green) pump light by $W_G(\boldsymbol{r},t)$, the (red) probe light by $W_R(\boldsymbol{r},t)$, and the amplified spontaneous emission by $W_A(\boldsymbol{r},t)$. For each position and time-dependent energy density, we can write a diffusion equation with the appropriate source terms. Absorption of ASE or probe light is not taken into account. The concentration $N_1(\boldsymbol{r},t)$ of excited laser particles (ions, molecules, ...) is determined by the rate equation of the laser material. We assume a four level laser system as described in the previous section, with a very fast decay rate from level (2) to level (1) and from level (0') to the ground state (0), which means level (2) and level (0') are nearly unpopulated. The excitation level is given by $N_1(\boldsymbol{r},t)/N_t$, with N_t the total concentration of laser particles. We arrive at the following set of coupled differential equations describing our system:

$$\frac{\partial W_G(\boldsymbol{r},t)}{\partial t} = D\nabla^2 W_G(\boldsymbol{r},t) - \sigma_{abs} v[N_t - N_1(\boldsymbol{r},t)]W_G(\boldsymbol{r},t) + \frac{1}{\ell} I_G(\boldsymbol{r},t) \quad (5.4)$$

$$\frac{\partial W_R(\boldsymbol{r},t)}{\partial t} = D\nabla^2 W_R(\boldsymbol{r},t) + \sigma_{em} v N_1(\boldsymbol{r},t)W_R(\boldsymbol{r},t) + \frac{1}{\ell} I_R(\boldsymbol{r},t) \quad (5.5)$$

$$\frac{\partial W_A(\boldsymbol{r},t)}{\partial t} = D\nabla^2 W_A(\boldsymbol{r},t) + \sigma_{em} v N_1(\boldsymbol{r},t)W_A(\boldsymbol{r},t) + \frac{n}{\tau_e} N_1(\boldsymbol{r},t) \quad (5.6)$$

$$\begin{aligned}\frac{\partial N_1(\boldsymbol{r},t)}{\partial t} &= \sigma_{abs} v[N_t - N_1(\boldsymbol{r},t)]W_G(\boldsymbol{r},t) \\ &\quad -\sigma_{em} v N_1(\boldsymbol{r},t)[W_R(\boldsymbol{r},t) + W_A(\boldsymbol{r},t)] - \frac{1}{\tau_e} N_1(\boldsymbol{r},t),\end{aligned}$$

where v is the transport velocity of the light inside the medium, σ_{abs} and σ_{em} are respectively the absorption and emission cross section, and τ_e is the lifetime of the excited state. D is the diffusion constant given by:

$$D = \frac{v\ell}{3}, \quad (5.7)$$

and $I_G(\boldsymbol{r},t)$ and $I_R(\boldsymbol{r},t)$ are the intensities of respectively the incoming pump and probe pulses. For simplicity, we use the same value of the diffu-

sion constant for the pump and probe light, and for the ASE. The probe pulse is incident on the front sample interface. The pump pulse is either incident on both the front and rear interface or on the front interface only. In the latter case we have:

$$I_G(\boldsymbol{r},t) = I_{G0}\sqrt{\frac{b}{\pi}}\exp\left[-\kappa_e z\right]\exp\left[-b\frac{(t-t_G-z/c)^2}{\tau_G^2}\right], \tag{5.8}$$

and

$$I_R(\boldsymbol{r},t) = I_{R0}\sqrt{\frac{b}{\pi}}\exp\left[-\kappa_e z\right]\exp\left[-\frac{(t-t_R-z/c)^2}{\tau_R^2}\right], \tag{5.9}$$

where $b = 4\ln(2)$, $\kappa_e \simeq \ell^{-1}$ is the extinction coefficient, and $c = c_0/n$, with n the effective refractive index of the medium.

Here I_{G0} and I_{R0} are the average intensities of respectively the pump and probe light, τ_G and τ_R are the pulse lengths (FWHM) of respectively the pump and probe pulse, and t_G and t_R are the points in time at which the maximum of respectively the pump and probe pulse is incident on the sample surface. If the pump pulse is incident on both sample interfaces we modify Eq. (5.8) to:

$$I_G(\boldsymbol{r},t) = I_{G0}\sqrt{\frac{b}{\pi}}\,\frac{\exp\left[-\kappa_e z\right]+\exp\left[-\kappa_e(L-z)\right]}{2}\exp\left[-b\frac{(t-t_G-z/c)^2}{\tau_G^2}\right]. \tag{5.10}$$

We consider a slab with thickness L, which leads to the spatial boundary condition:

$$W_G(\boldsymbol{r},t) = W_R(\boldsymbol{r},t) = W_A(\boldsymbol{r},t) = 0, \tag{5.11}$$

for

$$z = -z_0 \quad \text{and} \quad z = L + z_0. \tag{5.12}$$

where $z_0 \simeq 0.71\,\ell$ is the extrapolation length, as defined in section 2.2. The points in time t_G and t_R at which pump and probe pulse are incident are taken positive and large compared to the pulse lengths τ_G and τ_R. Therefore all energy densities are zero before $t = 0$:

$$W_G(\boldsymbol{r},t\le 0) = W_R(\boldsymbol{r},t\le 0) = W_A(\boldsymbol{r},t\le 0) = 0. \tag{5.13}$$

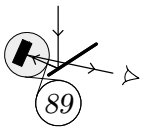

5.3.1 Discretization

Because our system is a slab in the xy-plane illuminated by plane waves in the z-direction, we can omit the x and y dependence of the energy densities. This means we can retain only the partial derivative to z in the gradients in Eqns. (5.4) to (5.7).

The resulting set of coupled partial differential equations can be solved numerically using a standard (forward Euler) discretization for the time derivative:

$$\frac{\partial f(z,t)}{\partial t} := \frac{f(z,t+\Delta t) - f(z,t)}{\Delta t} \tag{5.14}$$

and for the second order space derivative the straightforward discretization:

$$\frac{\partial^2 f(z,t)}{\partial z^2} := \frac{f(z+\Delta z,t) - 2f(z,t) + f(z-\Delta z,t)}{\Delta z^2}. \tag{5.15}$$

This discretization method has the advantage that it is simple and explicit, that is, the discretization of the space derivative depends only on $f(z,t)$ and not on $f(z,t+\Delta t)$. The disadvantage is that for small Δz, the time steps Δt have to be taken very small, to satisfy the stability criterion [4]:

$$\Delta t \leq \frac{\Delta z^2}{2D}. \tag{5.16}$$

The physical interpretation of this criterion is that, apart from a numerical factor, the time steps have to be smaller than the diffusion time across a distance Δz. The descretized set of equations is:

$$W_G(z,t+\Delta t) - W_G(z,t) = \Delta t\{D\frac{W_G(z+\Delta z,t)+W_G(z-\Delta z,t)-2W_G(z,t)}{\Delta z^2}$$
$$-\sigma_{abs} v[N_t - N_1(z,t)]W_G(z,t) + \ell^{-1} I_G(z,t)\} \tag{5.17}$$

$$W_R(z,t+\Delta t) - W_R(z,t) = \Delta t\{D\frac{W_R(z+\Delta z,t)+W_R(z-\Delta z,t)-2W_R(z,t)}{\Delta z^2}$$
$$+\sigma_{em} v N_1(z,t)W_R(z,t) + \ell^{-1} I_R(z,t)\} \tag{5.18}$$

$$W_A(z+\Delta z,t) - W_A(z,t) = \Delta t\{D\frac{W_A(z+\Delta z,t)+W_A(z-\Delta z,t)-2W_A(z,t)}{\Delta z^2}$$

$$+\sigma_{em} v N_1(z,t) W_A(z,t) + \frac{1}{\tau_e} N_1(z,t)\} \tag{5.19}$$

$$N_1(z+\Delta z,t) - N_1(z,t) = \Delta t\{\sigma_{abs} v[N_t - N_1(z,t)] W_G(z,t) \tag{5.20}$$

$$-\sigma_{em} v N_1(z,t)[W_R(z,t) + W_A(z,t)] - \frac{1}{\tau_e} N_1(z,t)\},$$

5.3.2 Backscattered flux

Solving the above set of partial differential equations numerically for practical values of σ_{abs}, σ_{em}, and τ_e at different pump intensities and values of ℓ, provides us with information about the spatial and temporal distribution of all relevant energy densities and the excitation level inside the sample. Also we can calculate the outgoing flux at either the front or rear interface of the slab, which is determined by the gradient of the energy density at the sample interface. For the outgoing probe flux at the front sample interface, we have:

$$W_R^{out}(t) \equiv A_s\, D\, \frac{\partial W_R(0,t)}{\partial z} = A_s\, D\, \frac{W_R(0,t)}{z_0}, \tag{5.21}$$

where A_s is the area of the sample surface. Here we have used that $W_R(z,t)$ is zero for $z = -z_0$.

In Fig 5.3 we have plotted the outgoing probe flux for a powdered Ti:sapphire sample (doping level 0.15 wt% Ti_2O_3) of 0.8 mm thickness and 4 mm diameter, with a transport mean free path $\ell = 40$ μm, for two pumping geometries. In the upper graph, the sample is pumped from one side with 14 ns pulses at 532 nm, with pulse energy 200 mJ. In the lower graph, the same total pump energy is incident on the sample, but now equally distributed over front and rear sample interface. The dotted lines indicate the incoming pump and probe pulses, and the dashed line denotes the outgoing probe flux without amplification. The latter is slightly lower than the incoming probe flux due to the finite sample thickness which allows some probe flux to disappear through the back sample interface. The ratio of the amplified to the unamplified outgoing probe flux indicates the average overall gain in the sample. Here the overall gain is 163% for single sided and 142% for double sided pumping.

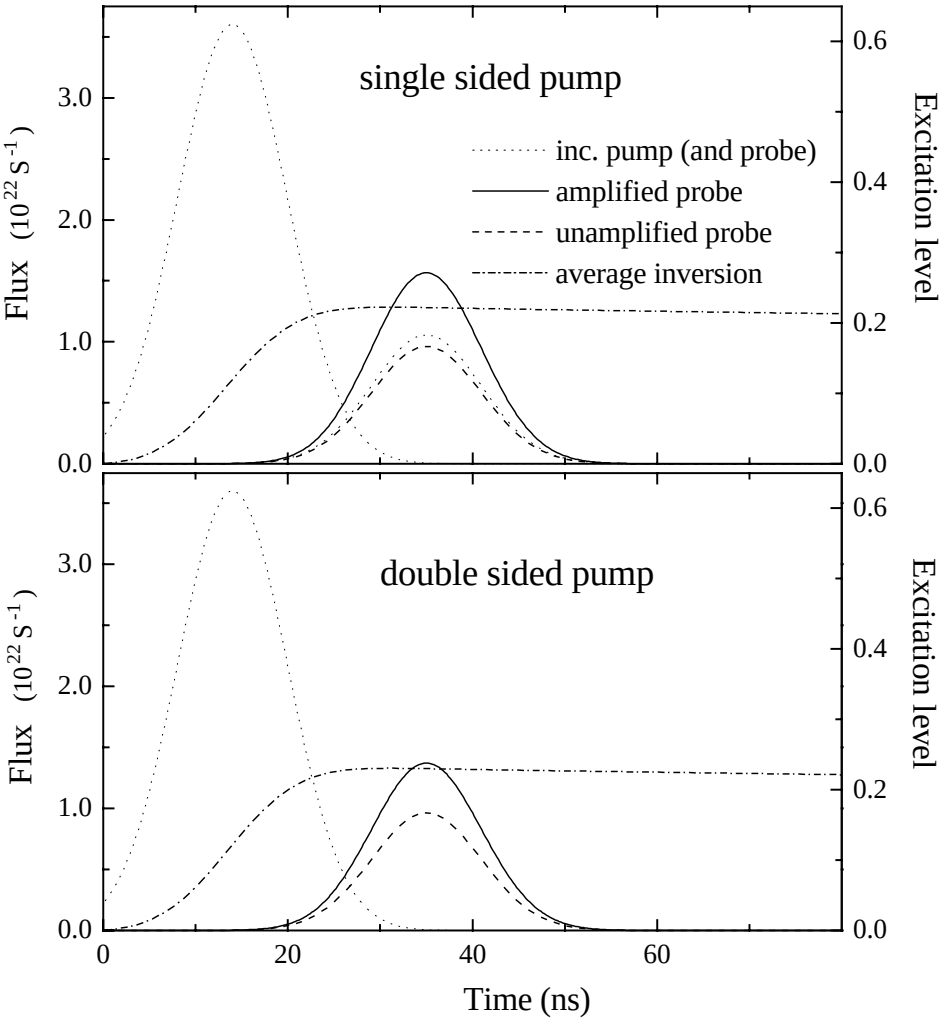

Figure 5.3: *Outgoing probe flux in backscattering for single sided and two sided pumping ($W_R^{out}(t)$) (solid line), for a powdered Ti:sapphire sample (doping level 0.15 wt% Ti_2O_3). Sample thickness: 0.8 mm, diameter: 4 mm, and transport mean free path: $\ell = 40$ μm. In the upper graph, the sample is pumped from one side with 14 ns pulses at 532 nm, with pulse energy 200 mJ. In the lower graph, the same pulse energy is distributed over both sample interfaces. The dashed line is the outgoing probe flux without amplification (i.e. without pump light). The dotted line is the incoming probe and pump flux, of which the latter is scaled by a factor 10^3. Also shown is the average excitation level in the sample defined as the ratio of the concentration of excited laser particles to the total concentration of laser particles (dash-dot).*

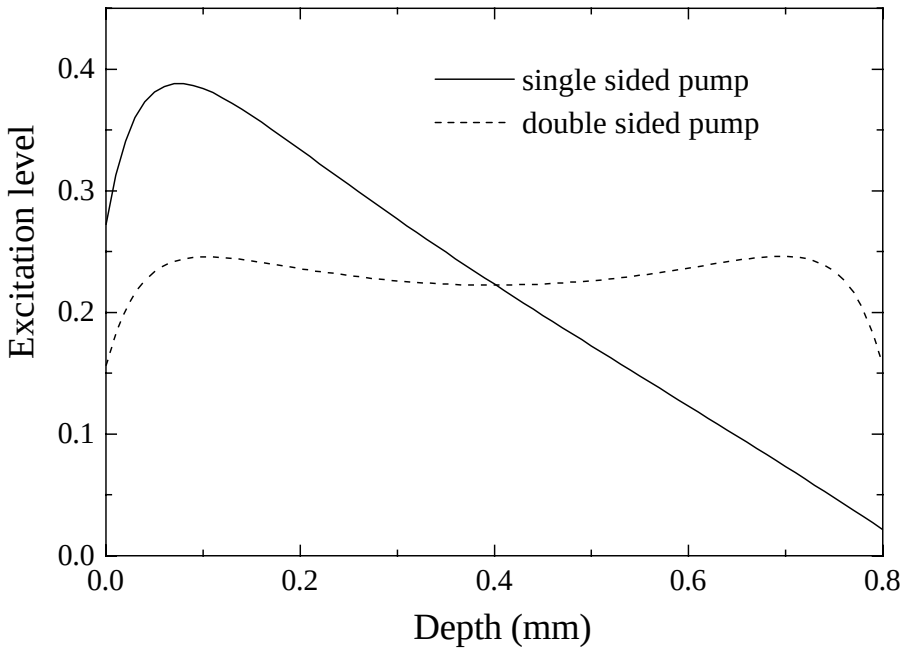

Figure 5.4: *Spatial profile of the excitation level just after the pump pulse, for single sided and two sided pumping, for the same sample and pump geometry as in Fig. 5.3. The excitation level for two sided pumping is nearly homogeneous, and its average is slightly larger than the average excitation level for single sided pumping.*

5.3.3 Spatial profile of the excitation level

The advantage of two sided pumping is that the resulting excitation level in the sample, and thereby the local gain, is nearly homogeneous. In Fig. 5.4, we have plotted the spatial profile of the excitation level just after the pump pulse for single and double sided pumping. The pump energy and the sample parameters are the same as in Fig. 5.3. We see that the excitation level drops almost linear with increasing z for the single sided case, whereas the excitation level becomes almost homogeneous if we pump from two sides. Also the average excitation level is somewhat higher for two sided pumping. Despite this fact, the average overall gain is smaller for two sided pumping, as we saw in Fig. 5.3. Apparently, in trying to obtain a large overall gain in backscattering, the excitation of the sample at small

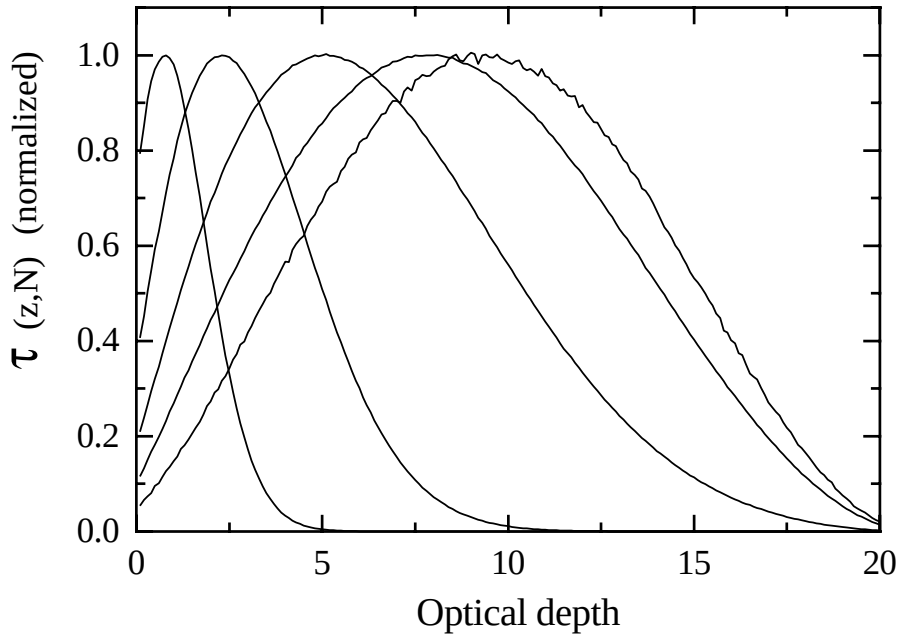

Figure 5.5: *Depth dependence of the residence time per order of scattering and per unit thickness $\tau(z, N)$, of light that eventually leaves the sample in backscattering. The curves were calculated with a Monte-Carlo simulation of a random walk in three dimensions for a slab with optical thickness 20 ℓ. Going from left to right the order of scattering (N) is 20, 100, 400, 1000, and $\geq$ 2500 [5]. In the limit to infinite order of scattering the profile is symmetric around the middle of the sample (optical depth 10), closely resembling the profile for $N \geq 2500$.*

depth is more important than the excitation of the deeper lying parts of the sample.

This can be explained if we consider the average residence time $\tau(z, N)$ of light in a layer at depth z in the sample, per order of scattering and per unit of thickness, defined by:

$$\tau_t \equiv \int \sum_{N=1}^{\infty} \tau(z, N)\, dz, \tag{5.22}$$

where τ_t is the total residence time of the light in the sample. In Fig. 5.5, we have plotted the depth dependence of $\tau(z, N)$, for different orders of scattering, for light that eventually leaves the sample in backscattering. Going from left to right, the order of scattering for each curve increases where the most right curve is almost equal to the limiting case of infinite order of scattering, which is symmetric around the middle of the sample. We see that even for very long (finite) paths that leave the sample in the backscattering direction, the light spends on average more time in the first half of the sample. This explains why the (inhomogeneous) excitation profile of Fig. 5.4 obtained with single sided pumping, yields a larger overall gain, although the average excitation level is lower than for two sided pumping.

5.3.4 Pulsed amplified spontaneous emission

If we look at the temporal behaviour of the excitation in Fig. 5.3, we see that after the pump pulse, the excitation level is constant over the time window in which the probe pulse is present. Here, the excited volume is below the critical volume V_{cr}. If we increase the pump flux and vary the sample thickness, we can reach the critical regime in which the system becomes unstable. In Fig. 5.6, we have plotted the temporal profile of the amplified spontaneous emission flux in backscattering ($W_A^{out}(t)$) during and just after the pump pulse, for various pump fluxes and sample thicknesses. Also plotted, is the pump flux and the temporal profile of the average excitation level. Going from left to right, the sample thickness increases, and going from bottom to top, the pump flux doubles in every graph. We see that at sufficiently large pump fluxes and (or) large enough sample thicknesses, the outgoing ASE flux is pulsed.

This pulsed behaviour originates from the combination of a diffusion process with a time-dependent gain. The relevant length scale to describe the amplification in the system, is the amplification length ℓ_{amp}. During the pump pulse, the following process takes place.

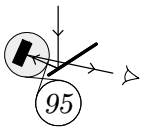

1. In the beginning of the pump pulse, the average amplification length in the medium decreases slowly due to the buildup of inversion. The time scale on which this buildup takes place is determined by the pump flux.

2. When ℓ_{amp} reaches a critical value (that is, when the critical thickness given by Ł$_{cr} = \pi\ell_{amp}$, becomes smaller than the sample thickness), the gain in the sample becomes larger than the loss through the boundaries. This leads to a large increase of the ASE energy density. The characteristic time scale corresponding to this buildup of ASE is ℓ_g/v, where ℓ_g is the gain length in the medium and v is the (transport) velocity of the light.

3. The situation that $\pi\ell_{amp} < L$ is unstable. The large ASE energy density will however de-excite the system, which leads to an increase of ℓ_{amp}. This increase continues as long as the large ASE energy density is present. The characteristic time scale on which the ASE energy density diffuses out of the medium through the front or rear interface, is given by L^2/D.

4. The equilibrium situation would be reached when gain equals loss, i.e. when $\pi\ell_{amp} = L$. However, if the buildup of a new inversion is slow compared to L^2/D, ℓ_{amp} will become larger than L and the process starts all over again.

This process leads to (transient) oscillations in the outgoing ASE flux. Damping of the oscillations occurs due to the fact that the increase of ℓ_{amp} in step 3 is opposed by re-excitation due to the presence of pump light. The system reaches therefore after a few oscillations the equilibrium situation $\pi\ell_{amp} = L$.

In Fig. 5.6, the pump flux and the sample thickness is varied. We see that for larger pump fluxes (going from bottom to top in the graph), the oscillations start earlier and are more rapid, which is due to a more rapid decrease of ℓ_{amp}. We also see that at larger pump fluxes, the equilibrium state is reached earlier. This is due to a larger damping of the oscillation in step 3. At extremely large pump fluxes, no pulsed output is observed because the oscillations become overdamped.

Upon increasing the sample thickness L (going from left to right in the graph), the oscillations also start earlier because the situation $\pi\ell_{amp} < L$ is reached at larger values of ℓ_{amp}. The value of ℓ_{amp} determines ℓ_g via $\ell_{amp} = \sqrt{\ell\,\ell_g/3}$. The gain length ℓ_g is inversely proportional to the excitation level, so the obtained excitation level is in principle inversely proportional to the square of the sample thickness. (At large sample thicknesses, the spatial profile of the pump energy density starts to play a role. The pump light does not penetrate into the deepest layers of the sample due to absorption, and the sample is therefore effectively thinner than L.) Be-

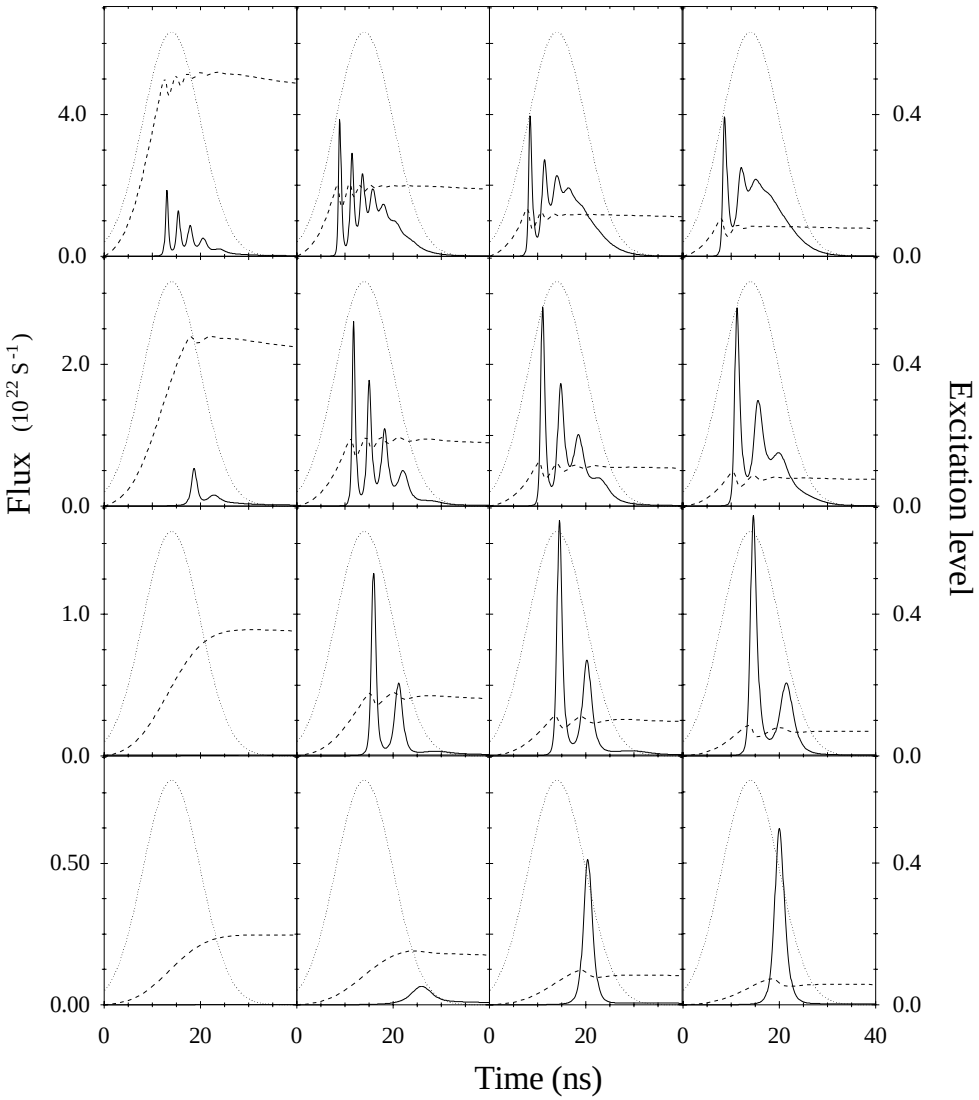

Figure 5.6: *Temporal profiles of the amplified spontaneous emission flux in backscattering from a powdered Ti:sapphire sample (doping level 0.15 wt% Ti_2O_3), transport mean free path $\ell = 100\ \mu m$, for different sample thicknesses and average pumping fluxes. The pulse duration of the pump pulse is 14 ns. Also plotted, is the temporal profile of the excitation level (dashed) and the pump flux (scaled by a factor $4{\cdot}10^3$) (dotted). Sample diameter 4 mm. Going from left to right, the thickness of the sample increases in each graph with one mm, starting from 1 mm, and going from bottom to top, the average pump flux doubles in every graph, starting from $1.25{\cdot}10^7\ Js^{-1} \mathrel{\widehat{=}} 3.4{\cdot}10^{25}$ photons per second.*

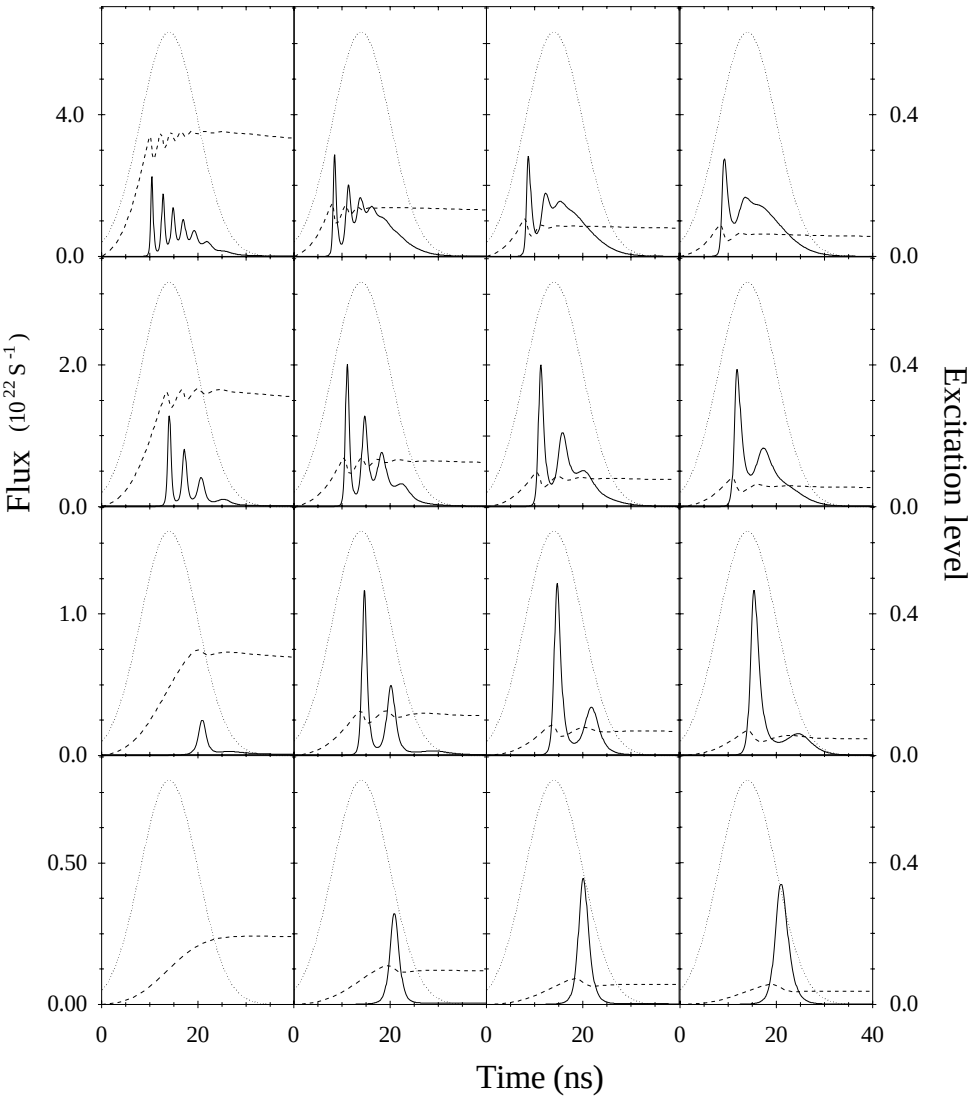

Figure 5.7: *Same as in Fig. 5.6, but for a half as long transport mean free path:* $\ell = 50\ \mu m$.

cause the characteristic time scale for the buildup of ASE is ℓ_g/v, and the timescale for the diffusion out of the sample is L^2/D, oscillations become slower at larger sample thickness. This again leads to the fact that the equilibrium state is reached earlier.

In Fig. 5.7, the same graph is plotted as in Fig. 5.6 but now for a half as long transport mean free path ℓ. Because ℓ_{amp} is proportional to the square root of ℓ, a decrease of ℓ leads to an earlier onset of the oscillations. This again leads to larger values of ℓ_g and correspondingly smaller values of the excitation level. Due to a larger ℓ_g and a smaller diffusion constant ($D = \frac{1}{3}v\ell$), the oscillations are slower and the equilibrium state is reached earlier.

Concluding we can say, that powdered laser materials can show a pulsed output depending on various experimental parameters. This pulsed behaviour is due to the combination of a diffusion 'loss' process and a time-dependent gain process. The consequence for realizing amplifying random media is, that the pump parameters must be chosen with care. Largely increasing the pump flux does not necessarily lead to a considerably larger gain coefficient in the medium.

5.4 Random lasers

The output of an amplifying random medium can show characteristics that are very similar to laser action. The output can be spectrally narrow and pulsed. It is tentative to call this system a random laser, however one has to be careful. It is important to distinguish three different regimes of multiple scattering with gain, depending on the strength of the scattering.

Very weak scattering and gain

If the scattering is very weak, that is ℓ is of the order of the sample size, the role of the scatterers is to scramble the directionality of the light emitted by the laser material. If we pump a clear laser material in a certain geometry, ASE will build up in the direction of largest gain, which is generally the direction in which the excited region is most extended. This yields a directionality in the output of the system. Due to gain narrowing, the spectrum of ASE can be very narrow like the output of a laser. Also, due to the build up of ASE, the temporal behaviour of the emission can be very rapid. The pulse length of ASE can be much shorter than the lifetime of the excited state of the laser material, but is always equal to or larger than the pump pulse length. If one adds some scatterers to the clear laser material, the

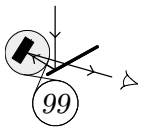

directionality of the ASE is scrambled, and in all directions the output will be narrow banded and will decay rapidly. In Ref. [6] this effect was mistakenly interpreted as random laser action (see Ref. [7]). If one monitors the emitted light in a direction in which the excited clear laser material shows no ASE, the introduction of some scatterers will result in a narrowing of the observed spectrum (see Fig. 5.8), and a shortening of the pulse length of the emission (see Fig. 5.9). In this regime of very weak scattering, the only role of the particles is to scramble the directionality of the ASE, which builds up (also in the absence of scatterers) in the excited laser material.

Weak scattering and gain

If the scattering is stronger so that ℓ is much smaller than the sample size but still larger than the wavelength, we are in the regime where the scatterers influence the spectrum of the output. In this regime, ASE builds up along random paths in the sample that are much longer than the direction in which the sample is most extended. This means that due to the scattering process, ASE can build up in a laser material that would show no ASE without scatterers. Here the scattering contributes to gain narrowing, because it largely increases the residence time of the light in the sample. This also leads to a pulsed output, as we found in section 5.3, and in this case the pulse duration of the ASE can be shorter than the pump pulse length. This pulsed output was also observed in Ref. [8], where the emission characteristics from powdered laser crystals were studied.

In the above described situation of weak scattering with gain, the scattering process induces a narrow spectrum and pulsed output. Therefore it is tempting to call this effect random laser action. However, to achieve laser action, some feedback mechanism is required. In a laser, the cavity mirrors provide this feedback mechanism. Due to this feedback, lasing only occurs in the spatial *modes* allowed by the cavity. In the weak scattering regime, the light waves perform a random walk without returning to a specific scatterer, so there is no feedback.

Strong scattering and gain

The feedback mechanism which is essential for a laser oscillator, could be provided by recurrent scattering events that occur, as we have shown in chapter 4, in the strong scattering regime for $k\ell \lesssim 10$. If the amplification along a recurrent light path would be strong enough, these recurrent (loop type) paths could serve as ring cavities for the light. In that case the system would lase in the modes allowed by these random ring cavities. This we

would call random laser action.

If we consider a system in which the amplification does not take place inside the particles but in between two scattering events (e.g. a medium that consists of TiO_2 particles suspended in a laser dye solution), the waves do not have to return to a specific scatterer to attain optical feedback. The criterium for a feedback mechanism then becomes whether waves return to a certain position in the amplifying medium surrounding the scatterers.

From an experimental point of view, it is difficult to obtain strong scattering and amplification. One option would be to dope TiO_2 particles with e.g. a Rhodamine laser dye. The disadvantage of such a system is that the lifetime of the excited state is very short (see section 5.2), and experiments have to be performed with picosecond time resolution. Another option is to mix a strongly scattering medium like TiO_2 powder with powdered Ti:sapphire. In that case however, the presence of Ti:sapphire particles reduces the scattering strength compared to a pure TiO_2 powder.

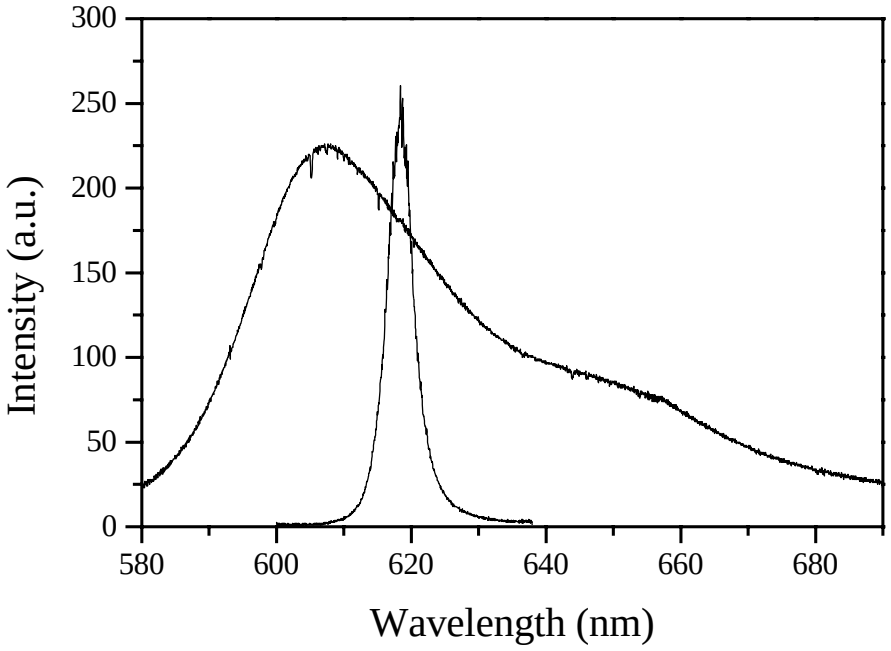

Figure 5.8: *Emission spectrum of a* $2.5 \cdot 10^{-3}$ *M solution of Rhodamine 640 perchlorate in methanol pumped by 3 mJ (10 ns) pulses at 532 nm. Pump beam diameter 1.5 mm. The broad spectrum corresponds to the (spontaneous) emission from the front window of the dye cell whereas the narrow spectrum corresponds to the emission (ASE) from the* side *windows. The same narrow spectrum is observed from both the front and side windows if a small concentration of* TiO_2 *particles (about* 10^{10} cm^{-3}*) is added, making the solution somewhat turbid.*

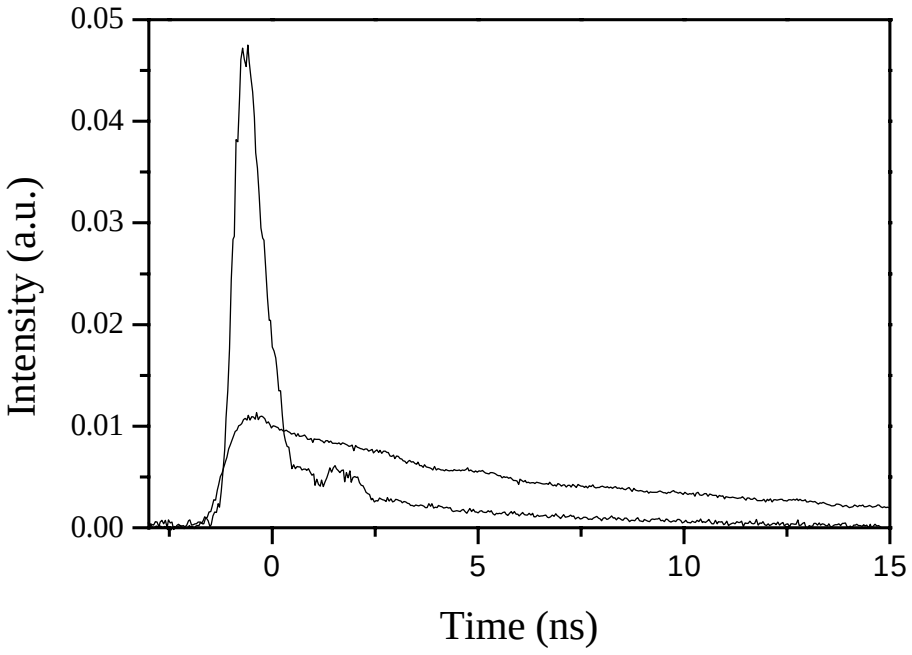

Figure 5.9: *Temporal emission of a $2.5 \cdot 10^{-3}$ M solution of rhodamine 640 perchlorate in methanol pumped with 58 μJ (30 ps) pulses at 532 nm. The slowly decaying peak corresponds to the spontaneous emission from the front window whereas the short peak corresponds to the emission (ASE) from the side windows. If about 10^{10} cm^{-3} TiO_2 particles are added, the short peak is observed in all directions. The length of the short peak is determined by the time resolution of the detector which is about 1 ns. The rapid structure following the short peak is a common artifact from ringing in the fast detection system.*

References and notes

[1] Note that the term photon is used to denote a classical energy packet and does not refer to a quantization of the light field.

[2] M.P. van Albada, B.A. van Tiggelen, A. Lagendijk, and A. Tip, Phys. Rev. Lett. **66**, 3132 (1991).

[3] A. Bott and W. Zdunkowski, J. Opt. Soc. Am. **A4**, 1361 (1987).

[4] W.H. Press, B.P. Flannery, S.A. Teukolsky, and W.T. Vetterling, *Numerical Recipies* (Cambridge University Press, 1989).

[5] The last curve (for $N \geq 2500$) is the summation of $\tau(z, N)$ over $N = 2500 \ldots \infty$.

[6] N.M. Lawandy, R.M. Balachandran, A.S.L. Gomes, and E. Sauvain, Nature **368**, 436 (1994).

[7] D.S. Wiersma, M.P. van Albada, and A. Lagendijk, Nature **373**, 203 (1995).

[8] C. Gouedard, D. Husson, C. Sauteret, F. Auzel, and A. Migus, J. Opt. Soc. Am. B **10**, 2358 (1993).

Chapter 6

Experiments on random media with gain

6.1 Introduction

The availability of amplifying random media as described in chapter 5, allows to study multiple scattering (interference) phenomena in active media. The experimental studies on multiple light scattering so far, have been restricted mostly to passive and linear random media. One nonlinear experimental study was performed on powdered $LiNbO_3$ crystals [1], where spatial correlations of second harmonic waves were studied. This system was nevertheless still a passive medium.

Much interest is shown recently in performing coherent experiments on active, amplifying random media. In a recent paper by Lawandy et al. laser effects were reported from suspensions of latex microspheres in laser dye solutions [2], but the reported phenomenon is not induced by scattering (see section 5.4). Recently it was shown by Gouedard et al. that powdered laser crystals can serve as incoherent quasi monochromatic light sources [3]. No coherent multiple scattering experiments have been performed yet on amplifying random media.

The behaviour of an amplifying random medium is expected to be different from that of an (absorbing) passive one. Since the amplification along a light path depends on the path length, the overall scattering properties depend strongly on the sample size. As explained in section 5.1.1, there is for instance a critical sample size, above which the intensity diverges and the system becomes unstable. In that sense, multiple light scattering with gain is similar to neutron scattering in combination with nuclear fission [4].

In this chapter, we will discuss experiments on laser speckle and coherent backscattering from an amplifying random medium. Both experiments, are a demonstration of the combination of a multiple scattering interference effect with optical amplification.

6.2 Laser speckle

When coherent laser light is scattered by a random collection of particles or even a rough surface, the angular dependence of the scattered intensity shows strong fluctuations known as laser speckle [5]. These fluctuations are of the order of the average scattered intensity, and at some angles the scattered intensity is truly zero. This effect is due to interference between (multiply) scattered waves.

A speckle pattern that is recorded in transmission from a random collection of particles, is very sensitive to the relative positions of the particles. The pattern changes completely if the particles move over a distance much smaller than the wavelength. The change of phase of a scattered wave is due to the motion of all particles from which this wave is scattered. If a wave is scattered by N particles, its phase will change significantly if each particle moves over a distance of only 1/N times the wavelength. This effect is used to study the motion of particles on a length scale much smaller than the wavelength, in a technique called 'Diffusing-Wave Spectroscopy' [6].

One can model a random sample as a waveguide that couples incident waves from incoming modes α and α' to outgoing modes β and β'. For a random sample, a mode is a solid angle containing one coherence area (i.e. one speckle spot). The intensity transmission coefficient from incoming mode α to outgoing mode β is denoted by $T_{\alpha\beta}$. The correlation between the intensities in different modes is given by: $C_{\alpha\beta\alpha'\beta'} = \langle \delta T_{\alpha\beta}\, \delta T_{\alpha'\beta'} \rangle$ with $\delta T_{\alpha\beta} = (T_{\alpha\beta} - \langle T_{\alpha\beta} \rangle)/\langle T_{\alpha\beta} \rangle$, where angular brackets denote an average over different configurations of the sample. The correlator $C_{\alpha\beta\alpha'\beta'}$ consists of three terms describing short range, long range, and 'infinite range' correlations [7]. We will not discuss these correlations in this thesis.

If one wants to study the mode properties of an amplifying medium —for instance, if one wants to realize and study a 'random laser'— it is important that the particles are stationary over a length scale much smaller than the wavelength. One can expect that the large intensities required to excite the laser material, will locally heat up the sample and induce structural changes that average out the speckle pattern.

6.2.1 Experimental configuration and results

The outline of the setup is relatively simple. A powdered Ti:sapphire sample is pumped with intense pulses from a frequency doubled Nd:YAG laser (wavelength 532 nm, pulse duration 14 ns, repetition rate 10 Hz). With a time delay of 14 ns after the pump pulse, a low intensity probe pulse is incident on the sample (wavelength 780 nm, pulse duration 14 ns, pulse energy 85 μJ). The transmitted probe light is recorded with an optical fiber (core diameter 50 μm) at a distance of 40 cm from the sample, which corresponds to a solid angle of detection of 125 μrad. The scattered intensity at a fixed position is recorded while the sample rotates. This way, both the incoming and outgoing angle are varied at the same time [8]. This is a 'one mode in, one mode out' type of experiment, because the light is incident in one direction, and the solid angle of detection is smaller than the size of one speckle spot.

The diameter of the probe beam is about 200 μm. Pump and probe beam are incident on the same side of the sample. The sample has a slab geometry with a thickness of about 100 μm, and consists of powdered Ti:sapphire (doping level 0.15 wt% Ti_2O_3). The particles are strongly polydisperse and have an average diameter of 10 μm. The preparation of the samples is described in section 6.3.1.

The pulse energy of the pump light was varied between 0 and 100 mJ, and the diameter of the pump beam was varied between 4 and 6 mm. The pump beam was blocked at every second shot and the probe signal obtained this way without pump light, was averaged separately to serve as a reference measurement. The detected probe signal was averaged over 25 laser shots. In Fig. 6.1, the transmitted probe intensity is plotted versus the rotation angle of the sample. The solid line corresponds to a pump energy of 98 mJ, at a beam diameter of 7.5 mm, which corresponds to a pump intensity of $1.6{\cdot}10^{11}$ J/m^{2}s. The dotted line is the reference measurement without pump light. The overall gain (i.e. the average gain over all angles) of the measurement with pump light is 18 %. We see that the introduction of gain does not change the observed pattern to a large extend. This behaviour is found for various measurements at low pump intensities. If we decrease the diameter of the pump beam to 5 mm at the same pulse energy (corresponding to a pump intensity of $2.4{\cdot}10^{11}$ J/m^{2}s), the observed pattern changes completely (see Fig. 6.2). This pump intensity is close to the damage threshold of the sample, which lies about a factor 2 - 3 above this intensity.

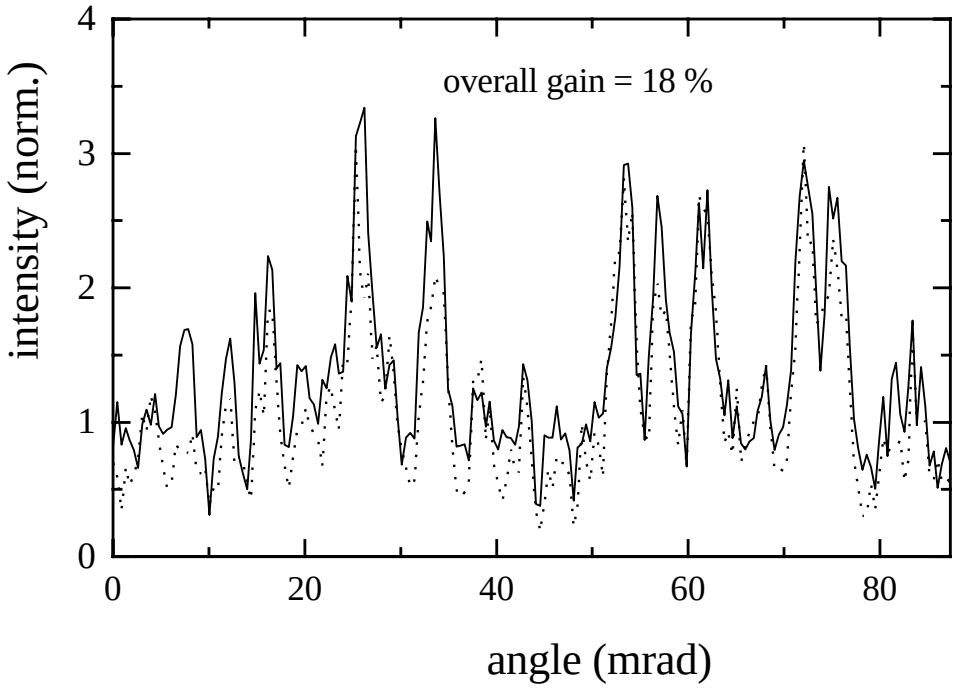

Figure 6.1: *Normalized transmitted intensity in a solid angle of 125 μrad, from a powdered Ti:sapphire sample, versus rotation angle of the sample. Sample thickness 100 μm. The solid line corresponds to a pump intensity of* $1.6{\cdot}10^{11}$ J/m^2s. *The dotted line is a reference measurement without pump light.*

6.2.2 Interpretation

From the data, we can draw the following conclusions. We find that a speckle pattern persists at modest pump intensities. This means that the sample is stationary over at least the timespan required to record one of the (about 5 mrad broad) peaks in Fig. 6.1, which is about 50 seconds. Only if the intensity is increased close to the damage threshold of the sample, the structure of the speckle pattern changes. This is likely to result from changes in the sample geometry due to heating of the sample. It is interesting to note however, that the amplitude of the fluctuations decreases only slightly. The intensity is averaged over 25 laser shots, which covers a timespan of 5 seconds. (Because the pump light is blocked every second shot, the effective repetition rate is 5 Hz.) If the observed fluctuations would be due to different configurations of the sample at every shot (i.e.

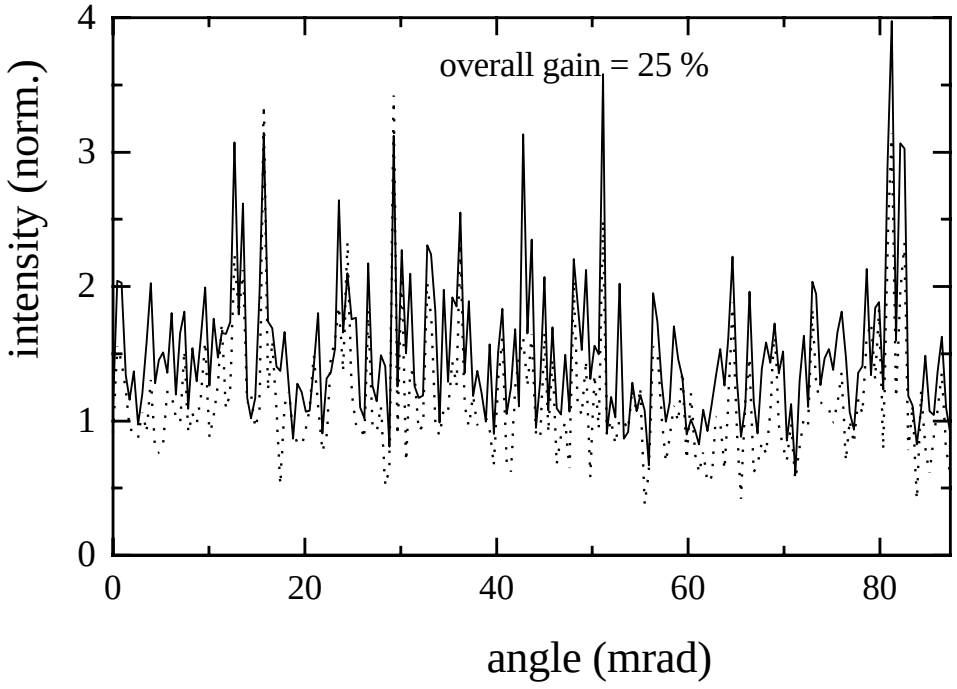

Figure 6.2: *Same as Fig. 6.1 at a larger pump intensity of 2.4· 10^{11} J/m^2s*

in case the single shot heating is large enough to change the positions of the scatterers at every shot), the amplitude of the fluctuations would be of the order of $1/\sqrt{25} = 0.2$. Also at high pump intensities, the observed fluctuations are much larger. This means that, if the observed effect is due to heating, the sample configuration changes over a timescale larger than a few seconds. We can conclude that it is possible to study one mode of an amplifying random medium, using modest pump intensities. At high pump intensities it is difficult to distinguish between effects from an increased gain and heating effects, because a speckle patterns is very sensitive to a small movement of the scatterers. An alternative would be to study speckle in a single shot experiment, in which the whole speckle pattern is recorded at once with e.g. a CCD camera.

6.3 Coherent backscattering

As explained in chapter 2, coherent backscattering is a general interference effect for waves which are backscattered from a random medium. It leads to a cone of enhanced backscattering in and around the exact backscattering direction, which usually has a width of the order of a few mrad. Coherent backscattering is an example of a multiple scattering interference effect. It is of particular interest because the (top of the) backscattering cone is due to very long light paths that have penetrated deep into the sample. Theoretically, paths of infinite length contribute to the cusp in the top of the backscattering cone. In practice, features due to $> 10^4$ scattering events are experimentally accessible. Because very long light paths contribute to the top of cone, we expect coherent backscattering to be strongly influenced by gain.

In the following, we will describe coherent backscattering experiments on samples of powdered Ti:sapphire. We found in chapter 5, that such samples can yield a (relatively large) gain of more than 150 %. Also we will show how diffusion theory can be used to calculate the angular dependence of the backscattered light from an amplifying random medium.

6.3.1 Samples

The samples consist of powdered Ti:Sapphire crystals. These powders were prepared by grinding Ti:Sapphire laser rods [10] for about 5 min. in a planetary micromill. The samples are strongly polydisperse with an average particle size of 10 μm. The (transport) mean free path ℓ was varied between 18 and 40 μm, by using both dry Ti:sapphire powders and suspensions of Ti:sapphire powder in water. The samples have a slab geometry, with thickness 1 mm and diameter 15 mm. The powders and suspensions are contained in a sample cell with a thick (1 cm) slightly wedged window, anti-reflection coated on the front side. Great care was taken to prepare the samples as clean as possible, because we found that any impurity that absorbs light at the pump wavelength, causes the sample to 'explode'. That is, the single shot heating of the sample around an impurity is large enough to cause serious structural damage to the sample. The long term heating of the sample due to the intense pump light was however less than 10 K.

6.3.2 Setup

The outline of the setup is drawn in Fig. 6.3. The Ti:Sapphire is optically pumped through the front sample interface with a frequency doubled

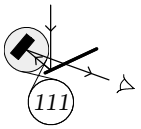

Nd:YAG laser (wavelength 532 nm) with pulse energies varying between 0 and 190 mJ. After a time delay of 14 ns, the green pump pulse is followed by a low intensity red probe pulse (wavelength 780 nm). The beams coincide spatially on the sample surface and both have a diameter of 5 mm. The angular distribution of the scattered probe light is recorded using the off-centered rotation setup as described in chapter 3. In this setup, an optical fiber and a photo multiplier tube are used to record the scattered probe light. The probe light is linearly polarized and both the polarization conserving and reversing channel have been monitored.

To record a backscattering cone, an average must be taken over many configurations of the sample, to eliminate the spatial speckle pattern which is always formed if a coherent beam is scattered from a (stationary) sample. To that end, the sample is rotated slowly around its axis. Because we use a pulsed probe beam with a pulse duration of 14 ns, the sample is almost completely stationary over the time window of one probe pulse. This means that the average over different sample configurations is performed with the repetition rate of the probe, which is 10 Hz. If we follow the rule of thumb that the relative fluctuations on the signal due to speckle are of the order of $N^{-1/2}$, with N the number of sample realizations, we have to average over $N = 10000$ probe shots to obtain a speckle noise level of 1 %. This leads to measurement times in the order of hours, to record a backscattering cone. To be able to correct for artifacts from e.g. cumulative heating of the sample or long term drift, the pump beam is blocked at every other shot. This way, the sample is pumped just before every second probe pulse only. The detected signals from even and odd probe pulses are averaged separately, so one experimental run yields one backscattering cone with gain, and one reference cone without gain.

The setup has to be aligned such that an angular scan passes through the top of the backscattering cone, which requires an accuracy of about 100 μrad both in the plane of the angular scan and perpendicular to it. This alignment is more difficult using pulsed light at a low repetition rate, which is also due to the large number of probe pulses over which one has to average. To facilitate this procedure, a CCD array is mounted close to the optical fiber (see Fig. 6.3). The CCD signal is stored and averaged over several frames. Alignment of the top of the cone on the center of the CCD array is considerably easier than alignment of the top on the head of the optical fiber. After alignment on the CCD array, the setup can be rotated over a (known) angle such that the top of the backscattering cone is aligned on the fiber. The CCD array could not be used to record backscattering cones with gain, because for these measurements, the detector must be gated on a nanosecond timescale (see below).

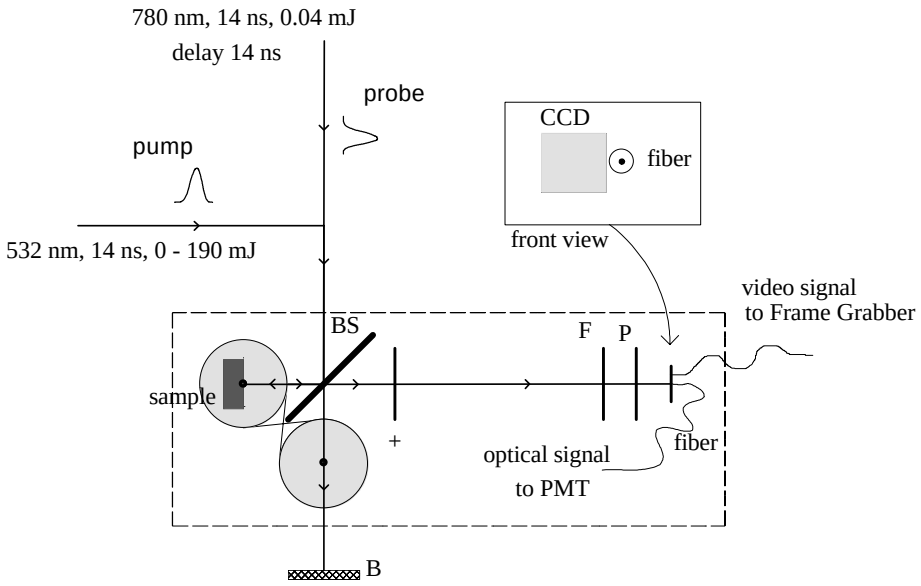

Figure 6.3: *Setup to record coherent backscattering from amplifying random media. A high intensity pump pulse (wavelength 532 nm, pulse duration 14 ns, repetition rate 5 Hz) with pulse energy 0-190 mJ, and low intensity probe pulse (wavelength 532 nm, pulse duration 14 ns, repetition rate 10 Hz) with pulse energy 40 μJ, are incident on the sample. Time delay between pump and probe: 14 ns. Pump and probe have a diameter of 5 mm, and overlap spatially on the sample. The principle used to record the angular distribution of the scattered probe is the same as described in Fig. 3.2. A CCD camera is mounted close to the detection fiber to facilitate the alignment. (Legend: BS: beam splitter, B: beam dump, F: narrow band filter with transmission wavelength 780 $\pm$ 5 nm, P: polarizer.)*

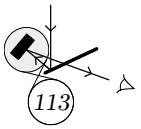

A problem that arises in scattering experiments on pumped laser materials, is that one has to distinguish between the scattered probe light and (amplified) spontaneously emitted light. Usually the bandwidth of the probe light is (much) smaller than the spectral width of the spontaneous emission. Therefore, a narrow band interference filter at the wavelength of the probe light is mounted in front of the detector. Furthermore, the time dependence of probe light and (amplified) spontaneous emission is usually very different. If the excited region in the sample is much smaller than the critical volume (see section 5.3), the characteristic time of the (amplified) spontaneous emission is close to the lifetime of the excited state of the laser material. The lifetime of the excited state of Ti:Sapphire is 3.2 μs. By monitoring the scattered light only during a limited time window of a few nanoseconds, the fraction of detected (amplified) spontaneous emission becomes negligible. This was done electronically by storing the oscilloscope trace of the PMT signal, and subsequently averaging the signal over the time window of 14 ns in which the probe is present.

6.3.3 Results

In Fig. 6.4, backscattering cones are shown as recorded for the same sample at different pump energies. The probe was linearly polarized and the polarization conserving channel was monitored. The solid line is a theoretical curve calculated with diffusion theory. We will describe this calculation in the next section. We see that the overall scattered intensity increases with pump energy. The pump energies for these data were 0, 165, and 190 mJ, which yields an overall gain of resp. 0, 36, and 71 %. We also see that the shape of the cone changes: upon increasing the gain, the top of the backscattering cone sharpens. This sharpening becomes even more apparent if the y-axis is scaled such that the background levels coincide, which is shown in Fig. 6.5. From Fig. 6.5 we also see that the enhancement factor is essentially independent of the gain.

In Fig. 6.6, the backscattering cone is shown from the same sample as in Fig. 6.4, monitoring the polarization reversing channel. We see that in the polarization reversing channel even without gain, the enhancement factor of the backscattering cone of these samples is too small to distinguish a cone from the diffuse background.

6.3.4 Interpretation

The narrowing of the top of the backscattering cone in the polarization conserving channel, can be understood if one realizes that the shape of

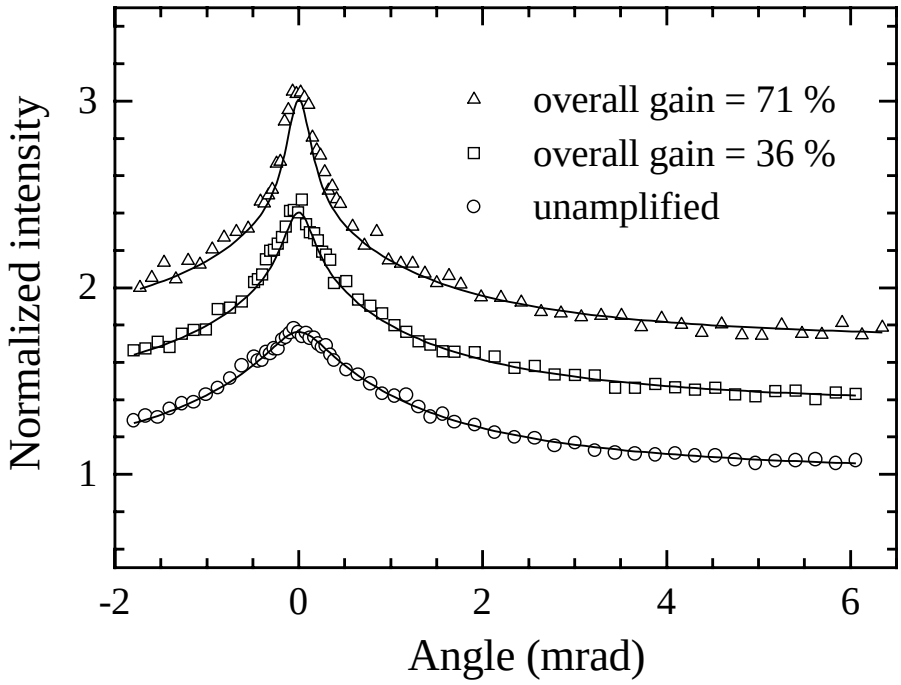

Figure 6.4: *Three backscattering cones in the polarization conserving channel from the same sample at different pump energy. Sample: 30 % Ti:Sapphire particles (10 μm) in water, transport mean free path: 40 μm. The overall gain of 0 %, 36 %, and 71 %, corresponds to pump energies: 0 mJ, 165 mJ, and 190 mJ. The intensity is normalized to the diffuse background at zero gain. Solid lines: calculated curves based on diffusion theory. Upon increasing the gain, the overall intensity increases and the top of the cone sharpens.*

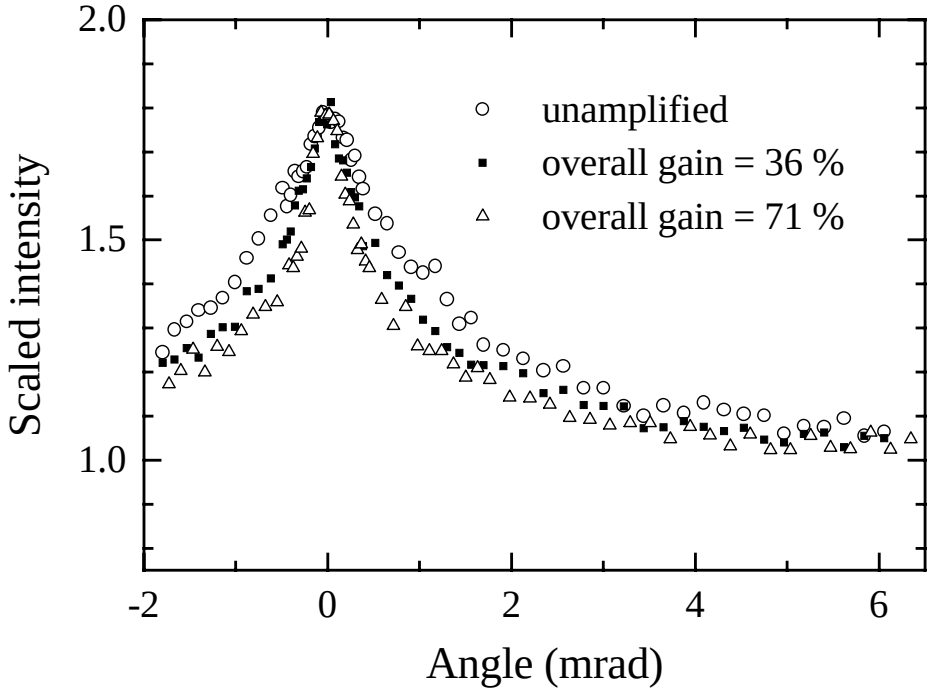

Figure 6.5: *Same backscattering cones as in Fig. 6.4 but y-axis scaled such that background levels coincide. One can see that the top of the cone sharpens and that the enhancement factor is essentially independent of the gain.*

the cone reflects the path length distribution in the sample. The angular range of the interference contribution to the backscattering cone from a certain light path, is inversely proportional to the distance between begin and end point of this path. The average distance between begin and end point, increases (on average) with the path length. The wings of the cone are therefore mostly due to contributions from short paths. As we approach the top of the cone, interference contributions from successively longer paths add to the intensity. In exact backscattering all paths contribute to the backscattering cone. Because the amplification along a path depends exponentially on its length, the introduction of gain will mainly affect the very central region of the backscattering cone. Both the very central region of the backscattering cone and the diffuse background will be amplified, while the wings of the cone are hardly affected. This leads to a sharpening of the top of the cone. Note that the backscattering cone

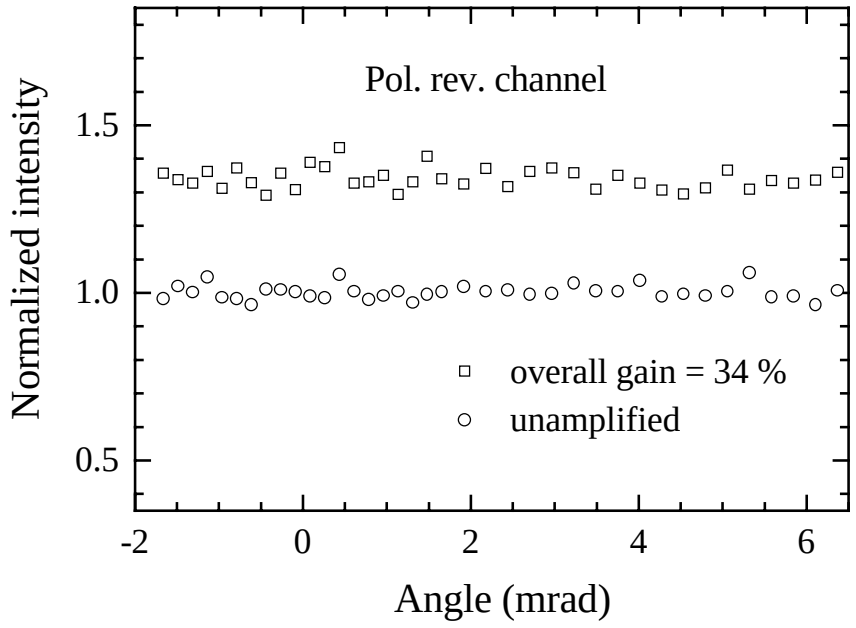

Figure 6.6: *Backscattering (cones) in the polarization reversing channel from the same sample at different pump energy. Sample: 30 % Ti:Sapphire particles (10 μm) in water, transport mean free path: 40 μm. The overall gain of 0 % and 34 % corresponds to pump energies of: 0 mJ and 165 mJ. The intensity is normalized to the diffuse background at zero gain. We see that for these samples the enhancement factor is too small to yield an observable backscattering cone.*

is superimposed on an (almost) angular independent diffuse background to which all light paths contribute.

As explained in section 2.5, the backscattering cone is a consequence of reciprocity. By the introduction of gain, reciprocity could be broken, which would lower the enhancement factor of the backscattering cone. After amplification of a pulse in part of the sample, the probed region is partly de-excited and the counterpropagating pulse will probe this region in a different state. For pulse durations comparable to the residence time of the light in the sample, this could affect reciprocity. In our system we do not expect this effect to occur, as the pulse duration by far exceeds the residence time and the pulse energy is low enough to leave the sample in almost the same state (there is no saturation of the gain at increasing probe energy). This is consistent with our observation that the enhancement

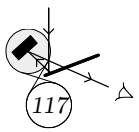

factor is essentially independent of the gain (Fig. 6.5).

In the polarization reversing channel, the backscattering cones from our samples did not exhibit a significant enhancement factor (Fig. 6.6). In the polarization reversing channel, correlation between the amplitudes and phases of counterpropagating waves diminishes with increasing order of scattering [11]. Coherent backscattering in this channel is due to low order scattering (short paths). Depending on the phase function of the scatterers, the enhancement factor ranges from 1.0 to about 1.2. We expect this enhancement factor to decrease with gain because long path contributions are only present in the background and not in the cone. Apparently our samples exhibit an enhancement factor smaller than 1.05, which does not allow to measure this dependence of the enhancement factor on gain.

6.3.5 Theory

In chapter 3, we found that the backscattering cone calculated in the diffusion approximation, provides a very good description of coherent backscattering from passive random media. In the following we will use diffusion theory to calculate the backscattered intensity from an amplifying random medium. We start from the stationary diffusion equation with gain [4,12]:

$$\tfrac{1}{3}\ell^2 \nabla^2_{\boldsymbol{r}_1} F(\boldsymbol{r}_1, \boldsymbol{r}_2) + \ell\kappa_g F(\boldsymbol{r}_1, \boldsymbol{r}_2) = -\delta(\boldsymbol{r}_1 - \boldsymbol{r}_2). \tag{6.1}$$

Here $F(\boldsymbol{r}_1, \boldsymbol{r}_2)$ is the intensity Green's function, κ_g is the gain coefficient in the medium, and ℓ is the (transport) mean free path. We assume κ_g to be position-independent.

If we use a slab geometry, the appropriate boundary condition is $F(\boldsymbol{r}_1, \boldsymbol{r}_2) = 0$ in planes at distance z_0 on both sides of the slab, with $z_0 \approx 0.71\ell$ [13]. In the conventional way of solving a diffusion equation with these boundary conditions (used in e.g. Ref. [14] to calculate the backscattering cone from a passive random medium with a slab geometry), the diffusion propagator $F(\boldsymbol{r}_1, \boldsymbol{r}_2)$ is first calculated for an infinite medium. Subsequently, the boundary conditions for the slab are fulfilled by multiple reflections of $F(\boldsymbol{r}_1, \boldsymbol{r}_2)$ in 'mirror planes' on both sides of the slab [15]. (These 'mirror planes' are also referred to as 'trapping planes'.) This procedure can not be followed for an amplifying medium, because the diffusion propagator $F(\boldsymbol{r}_1, \boldsymbol{r}_2)$ for an infinite amplifying random medium, diverges for $|\boldsymbol{r}_1 - \boldsymbol{r}_2| \rightarrow \infty$. Because we have to calculate the angular dependence of the backscattered intensity, we wish to perform a Fourier transform of the

form:

$$F(\boldsymbol{q}_\perp, z_1, z_2) = \int F(\boldsymbol{r}_1, \boldsymbol{r}_2) e^{i\boldsymbol{r}_\perp \cdot \boldsymbol{q}_\perp} d\boldsymbol{r}_\perp, \tag{6.2}$$

with $\boldsymbol{r}_\perp = \boldsymbol{r}_{1\perp} - \boldsymbol{r}_{2\perp}$ perpendicular to z, where the slab is oriented in the xy-plane. Here $\boldsymbol{q}_\perp$ is the perpendicular component of the outgoing wavevector. The integral has to be performed over the whole surface of the slab, and diverges because $F(\boldsymbol{r}_1, \boldsymbol{r}_2)$ diverges for $\boldsymbol{r}_\perp \to \infty$.

The solution to this problem is to perform the Fourier transformation on the original diffusion equation (6.1), before the boundary conditions are applied. The diffusion equation then reads:

$$\tfrac{1}{3}\ell^2 \left(\frac{\partial^2}{\partial z_1^2} - q_\perp^2 \right) F(\boldsymbol{q}_\perp, z_1, z_2) + \ell \kappa_g F(\boldsymbol{q}_\perp, z_1, z_2) + \delta(z_1 - z_2) = 0. \tag{6.3}$$

The boundary condition now is: $F(\boldsymbol{q}_\perp, z_1, z_2) = 0$ for $z_2 = -z_0$ and $z_2 = L + z_0$, and for every z_1. Solving Eq. (6.3) with this boundary condition we find:

$$F(\boldsymbol{q}_\perp, z_1, z_2) = F(\boldsymbol{q}_\perp, z_s, z_d) = \frac{3\cos(\beta(L - z_s)) - 3\cos(\beta(L + 2z_0 - |z_d|))}{2\ell^2 \, \beta \sin(\beta(L + 2z_0))}, \tag{6.4}$$

where $z_s \equiv z_1 + z_2$, $z_d \equiv z_1 - z_2$, L is the slab thickness, and

$$\beta \equiv \sqrt{\ell_{amp}^{-2} - q_\perp^2}, \tag{6.5}$$

with ℓ_{amp} the amplification length in the medium. The amplification length is defined as the (rms) average distance over which the intensity is amplified in the medium by a factor e^{+1}.

From Eq. (6.4) we can see that $F(\boldsymbol{q}_\perp, z_1, z_2)$ becomes unstable (that is diverges for small angles) for $L + 2z_0 \geq L_{cr} = \pi \ell_{amp}$, where L_{cr} is the critical thickness. In practice, if we try to make the amplifying region in a slab of disordered laser material thicker than L_{cr}, the gain will saturate close to $L = L_{cr}$, which provides an upper limit for the intensity.

With the solution for the diffusion propagator $F(\boldsymbol{q}_\perp, z_1, z_2)$ for a slab geometry, we can calculate the backscattering cone in the same way as was described in section 2.4 for a passive random medium. From Eq. (2.47), we can derive the following expression for the bistatic coefficient describing

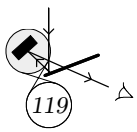

the backscattering cone:

$$\gamma_c(\theta_s) = \frac{1}{\ell}\int_0^L \int_{z_d}^{2L-z_d} F(\boldsymbol{q}_\perp, z_1, z_2)\cos(z_d\eta)e^{-uz_s}dz_s dz_d, \tag{6.6}$$

where $\eta \equiv k_0(1-\mu_s)$, $u \equiv \frac{1}{2}\kappa_e(1+\mu_s^{-1})$, and $\mu_s = \cos(\theta)$ with θ is the angle of the outgoing wavevector $\boldsymbol{k_2}$ relative to the z-axis. Here κ_e is the extinction coefficient given by $\kappa_e = \ell_s^{-1} - \ell_g^{-1}$, where ℓ_s is the scattering mean free path and ℓ_g is the gain length in the medium. The incoming wavevector is taken along the z-axis.

The integrals in Eq. (6.6) can be performed explicitly using the intensity propagator from Eq. (6.4). The result is:

$$\gamma_c(\theta_s) = \frac{3e^{-uL}}{2\ell^3\beta\sin[\beta(L+2z_0)]}\frac{1}{(\beta^2+\eta^2+u^2)^2-(2\beta\eta)^2}\times \tag{6.7}$$

$$\begin{aligned}
&\big[2(\beta^2+\eta^2+u^2)\cos(2\beta z_0)\cos(L\eta) - 4\beta\eta\sin(2\beta z_0)\sin(L\eta)\\
&\quad +2\frac{\beta}{u}(-\beta^2+\eta^2-u^2)\sin(\beta(L+2z_0))\sinh(uL)\\
&\quad +2(\beta^2-\eta^2-u^2)\cos(L\eta) - 2(\beta^2+\eta^2+u^2)\cos(\beta(L+2z_0))\cosh(uL)\\
&\quad +4\beta u\sin(\beta L)\sinh(uL) + 2(-\beta^2+\eta^2+u^2)\cos(\beta L)\cosh(uL)\big]\,.
\end{aligned}$$

In this expression, η, u, and β depend on the scattering angle θ. For small angles, this solution agrees with the results of Ref. [16], in which coherent backscattering from an amplifying medium was calculated, but in which an unnecessary approximation was made which makes their result only valid for the central region around the cusp of the cone. For passive media, usually the limit $L \to \infty$ is taken to obtain a much simpler expression. For amplifying media this is impossible due to the divergence of the intensity for $L > L_{cr}$.

It is instructive to compare the backscattering cone with gain to the cone from a passive medium. To that end, we can look at the parameter β defined in Eq. (6.5). We see that β is real valued only for small angles, that is for:

$$q_\perp = k_0\sin(\theta) \le \ell_{amp}^{-1}. \tag{6.8}$$

Otherwise, β is purely imaginary. In that case, the trigoniometric functions in Eq. (6.4) become hyperbolic functions and $F(\boldsymbol{q}_\perp, z_1, z_2)$ attains the form

of the diffusion propagator for a passive medium. This means that only for small angles, gain will affect the backscattering cone. This is consistent with our observations in the previous section. Note that light paths with a distance d between begin and end point, yield an interference contribution to the backscattered intensity with characteristic angular extent $\theta = (k_0 d)^{-1}$. With Eq. (6.8) we see, that the angular range in which the affect of gain is observed, corresponds to the angular extent of interference contributions from paths with $d > \ell_{amp}$.

The backscattering cone is superimposed on an angle-independent background. This background consists of a diffusive term γ_ℓ and contributions from paths that have no counterpropagating counterpart like single scattering. From Eq. (2.47), we have the following expression for the bistatic coefficient describing the diffuse background:

$$\gamma_\ell(\theta_s) = \frac{1}{\ell}\int_0^L\int_{z_d}^{2L-z_d} F(\boldsymbol{q}_\perp{=}0, z_1, z_2) e^{-\frac{1}{2}\kappa_e z_s(\mu_s^{-1}+1)} e^{-\frac{1}{2}\kappa_e z_d(\mu_s^{-1}-1)} dz_s dz_d. \tag{6.9}$$

The integrals in this expression can be performed explicitly using intensity propagator from Eq. (6.4) at $\boldsymbol{q}_\perp = 0$. The result is:

$$\gamma_\ell(\theta_s) = \frac{3}{2\ell^3\beta\sin(\beta(L+2z_0))} \frac{Z_1(1+e^{-2\,uL}) + Z_2(1-e^{-2\,uL}) + Z_3 e^{-L(v+u)}}{u[(u^2+\beta^2)^2 + v^2(2\beta^2 - 2u^2 + v^2)]} \tag{6.10}$$

with

$$Z_1 = u\,(v^2 - u^2 - \beta^2)\cos[\beta(L+2z_0)] + u\,(u^2 - v^2 - \beta^2)\cos(\beta L) \tag{6.11}$$

$$+2uv\beta\sin[\beta(L+2z_0)] + uv\beta\,\frac{v^2+\beta^2-3u^2}{u^2+\beta^2}\sin(\beta\,L),$$

$$Z_2 = v\,(u^2 - v^2 - \beta^2)\cos[\beta(L+2z_0)] + 2u^2\beta\sin(\beta\,L) \tag{6.12}$$

$$-\beta\,(u^2+v^2+\beta^2)\sin[\beta(L+2z_0)] + u^2 v\,\frac{v^2-u^2+3\beta^2}{u^2+\beta^2}\cos(\beta\,L),$$

and

$$Z_3 = 2u\,(v^2 - u^2 + \beta^2) + 2u\,(u^2 - v^2 + \beta^2)\cos(2z_0\,\beta) - 4uv\beta\sin(2z_0\,\beta). \tag{6.13}$$

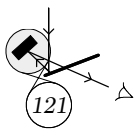

In this expression, the angular dependence is determined by the parameters: $u = \frac{1}{2}\kappa_e(\mu_s^{-1}+1)$, $v = \frac{1}{2}\kappa_e(\mu_s^{-1}-1)$, and $\beta = \sqrt{\ell_{amp}^{-2} - q_\perp^2}$, with $\mu_s = \cos(\theta)$. Again, due to the divergence of the intensity for $L > L_{cr}$, one can not take the limit $L \to \infty$ to simplify the above expression.

We define the overall gain Ξ, as the average over all angles of the ratio of the backscattered intensity to the backscattered intensity without amplification. Because the angular extent of the backscattering cone is very small compared to 2π, we can write the overall gain as:

$$\Xi \; = \frac{\gamma_\ell(\theta_s = 0, \ell_{amp})}{\gamma_\ell(\theta_s = 0, \ell_{amp} \to \infty)}. \tag{6.14}$$

This relation allows us to determine the average amplification length ℓ_{amp}, from the increase of the backscattered intensity.

Comparing data and theory

The total backscattered intensity is given by the sum of the diffuse background described by γ_ℓ, the backscattering cone described by γ_c, and a contribution from single scattering and possible experimental stray light. Over the angular range of the experimental backscattering cones shown in the previous section, γ_ℓ is nearly angle-independent. If we assume the single scattering and possible stray light to follow the same weak angular dependence as γ_ℓ, we can use equation 3.1 for the total intensity.

The solid lines in Fig. 6.4, are the calculated backscattered intensities found by using Eqs. (6.7) and (6.10) in Eq. (3.1). The mean free path ℓ for this sample and the enhancement factor E were inferred from the zero gain experiment (bottom curve). The overall gain Ξ was determined from the increase of the diffuse background intensity (measured at large angles) [17]. From the overall gain, the gain coefficient κ_g was calculated using Eq. (6.14). The gain coefficient is the only parameter that varies between the three curves in Fig. 6.4. The general agreement between data and theory is very good.

At large sample thicknesses, the calculated curves are slightly narrower than the measured ones. This effect becomes clear for large gain using optically thick samples (see Fig. 6.7). The effect is due to the spatial inhomogeneity of the inversion. The samples were pumped from the front side, so the gain decreases with increasing depth. Using the theory of section 5.3, we can calculate the spatial profile on the gain coefficient for our sample

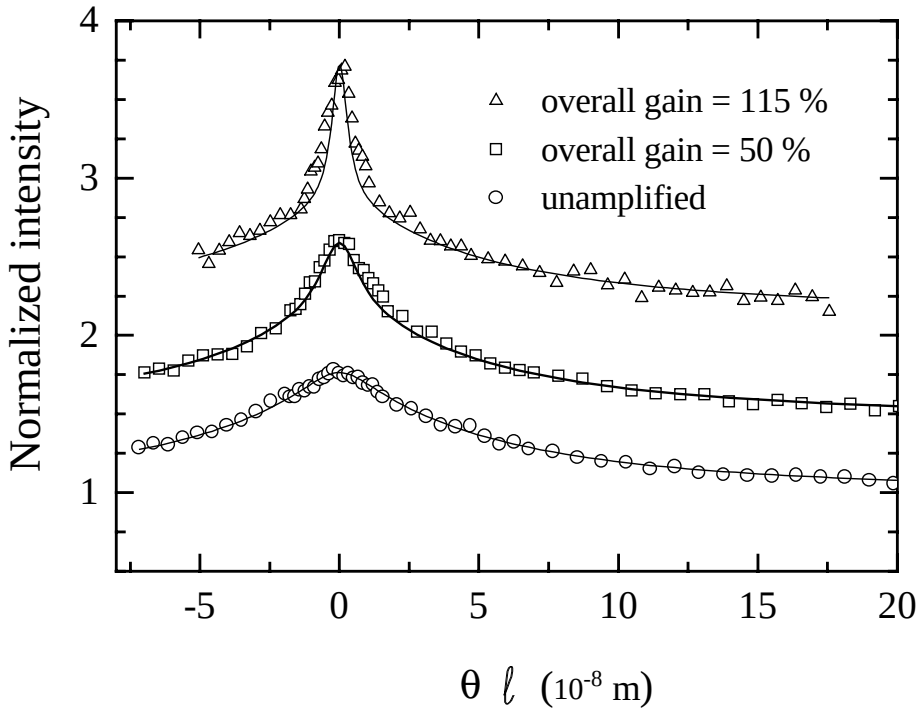

Figure 6.7: *Backscattered intensity from different samples, versus $\theta\ell$, with θ the scattering angle relative to backscattering and ℓ the transport mean free path. Going from bottom to top, the transport mean free path of the samples is resp. 40, 40, and 28 μm, and the pump energy is resp. 0, 180, and 180 mJ. The intensity is normalized to the diffuse background at zero gain. Solid lines: calculated curves based on diffusion theory. Because the calculation of the backscattering cone assumes constant gain, it overestimates the contributions from the longer (deeper penetrating) paths, resulting in a somewhat narrower cone.*

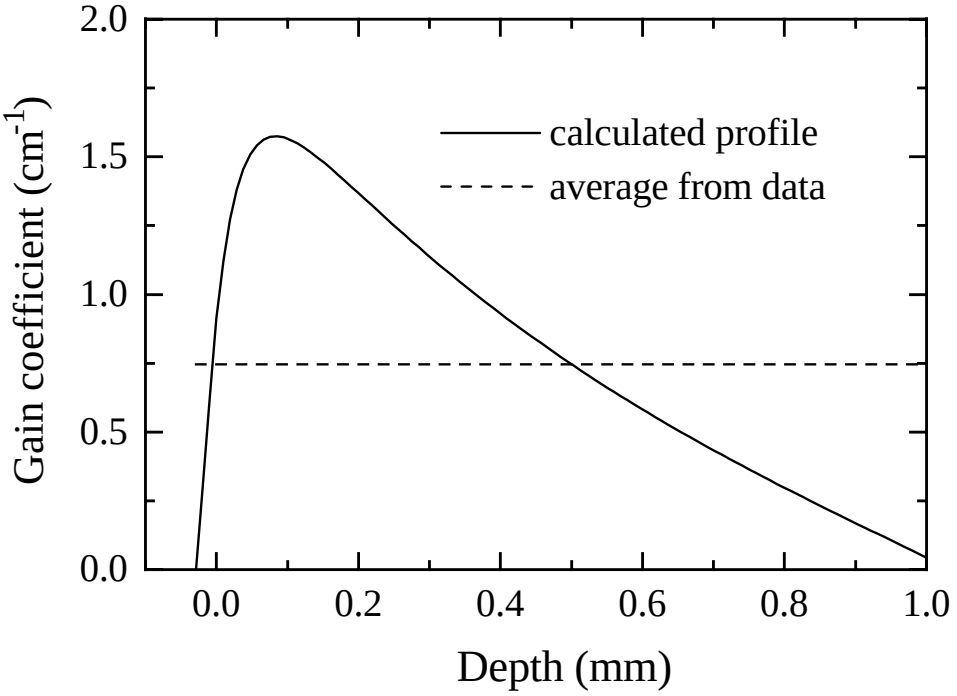

Figure 6.8: *Spatial profile of the gain coefficient κ_g, calculated numerically as described in section 5.3, for the sample and pump energy of the upper curve in Fig. 6.7. The dashed line is the average value of κ_g, determined from the data.*

and pump parameters. The results are shown in Fig. 6.8. The calculated backscattering cones assume a position-independent gain coefficient κ_g, which is determined from the measured overall gain. This average value of κ_g, as determined for the data of the upper backscattering cone in Fig. 6.7 is 0.746 cm^{-1}. We have denoted this value in Fig. 6.8 by a dashed line. Note that this value agrees well with the average of the calculated spatial inversion profile.

Longer light paths penetrate deeper into the sample. Because κ_g is smaller than its average value at large depths, the assumption of a position-independent κ_g leads to an overestimation of the contribution from longer light paths to the overall gain. For the calculation of the backscattering cone, this results in too narrow cones. As we saw in section 5.3, a more homogeneous gain could be obtained by pumping the sample from two

sides, which leads however to a somewhat smaller average gain.

6.4 Discussion

We have demonstrated the effect of gain on the multiple scattering interference phenomenon coherent backscattering. In future experiments, it is interesting to study the combination of amplification with very strong scattering. We saw in chapter 4, that for very strong scattering recurrent scattering becomes important. If gain lengths of the order of the scattering mean free path could be achieved, the importance of recurrent scattering could be enhanced due to gain. If the amplification along a recurrent light path is strong enough, this recurrent path could form a 'random ring cavity' along which laser action could set in. Another interesting experiment would be, to study the effect of gain on the diffusion constant in a random medium. If recurrent scattering becomes more important, the diffusion constant could decrease upon the introduction of gain.

To obtain strong scattering with amplification is difficult from an experimental point of view. A very interesting system would be a random collection of mono-disperse titanium dioxide particles (which scatter very strongly), doped with laser dye. The technological developments on realizing such particles are promising.

References and notes

[1] J.F. de Boer, A. Lagendijk, R. Sprik, and S. Feng, Phys. Rev. Lett. **71**, 3947 (1993).

[2] N.M. Lawandy, R.M. Balachandran, A.S.L. Gomes, and E. Sauvain, Nature **368**, 436 (1994).

[3] C. Gouedard, D. Husson, C. Sauteret, F. Auzel, and A. Migus, J. Opt. Soc. Am. B **10**, 2358 (1993).

[4] B. Davison and J.B. Sykes, *Neutron Transport Theory* (Oxford University Press, 1958).

[5] *Laser Speckle and Related Phenomena*, *Topics in Applied Physics* ***9***, edited by J.C. Dainty (Springer, Berlin, 1984).

[6] D.J. Pine, D.A. Weitz, P.M. Chaikin, and E. Herbolzheimer, Phys. Rev. Lett. **60**, 1134 (1988).

[7] S. Feng, C. Kane, P.A. Lee, and A.D. Stone, Phys. Rev. Lett. **61**, 834 (1988).

[8] This type of experiment can be used to record the short range angular correlation function [9].

[9] J.H. Li and A.Z. Genack, Phys. Rev. E **49**, 4530 (1994).

[10] Ti:Sapphire crystals were obtained from Single Crystal Technology B.V. Enschede.

[11] M.P. van Albada and A. Lagendijk, Phys. Rev. B **36**, 2353 (1987).

[12] V.S. Letokhov, Sov. Phys. JETP **26**, 835 (1968).

[13] H.C. van de Hulst, *Multiple Light Scattering* (Dover, New York, 1980).

[14] M.B. van der Mark, M.P. van Albada, and A. Lagendijk, Phys. Rev. B **37**, 3575 (1988).

[15] M.N. Barber and B.W. Ninham, *Random and Restricted Walks*, (Gordon and Breach, New York, 1970).

[16] A. Yu. Zyuzin, Europhys. Lett. **26**, 517 (1994).

[17] Here we assume that the amplification of the measured background intensity, is completely determined by γ_ℓ. This means that we assume that the single scattering (and stray light) contributions to the background are amplified by the same factor as γ_ℓ. If part of these contributions is not amplified, κ_g will be slightly underestimated.

Appendix A

List of symbols

Throughout this thesis we use Heaviside-Lorentz units. These are rationalized Gaussian units and yield elegant an simple equations. (See J.D. Jackson,*Classical Electrodynamics*, *Appendix on Units and Dimensions* (Wiley, New York, 1975).) They also avoid wandering factors of 4π. Both ϵ_0 and μ_0 are equal to 1. To convert any equation to SI units, simply replace $\mathbf{E}(\boldsymbol{r})$ by $\sqrt{4\pi\epsilon_0}\,\mathbf{E}(\boldsymbol{r})$ and $\epsilon(\boldsymbol{r})$ by $\epsilon(\boldsymbol{r})/\epsilon_0$, with $\epsilon_0 = 10^7/4\pi c_0^2$ $(A^2 s^4 kg^{-1} m^{-3})$.

Notation	**Explanation**	**Introduction**
σ_s	scattering cross section	Eq. (1.1)
σ_t	cross section for radiation pressure	sec. 1.1.1
σ_{abs}	absorption cross section	sec. 1.1.1
σ_{em}	emission cross section	sec. 5.2.1
σ_e	extinction cross section	Eq. (1.2)
ℓ_s	scattering mean free path	sec. 1.1.2
ℓ	transport mean free path	Eq. (1.6)
ℓ_{abs}	absorption mean free path	Eq. (1.7)
ℓ_i	inelastic mean free path	sec. 1.1.2
ℓ_{amp}	amplification mean free path	Eq. (5.1)
ℓ_g	gain mean free path	sec. 5.1.1
ℓ_e	extiction mean free path	sec. 1.1.2
$\kappa_\times$	reciprocal of $\ell_\times$	sec. 1.1.2

a	diameter of a scatterer	sec. 1.1.3
D	diffusion constant	sec. 2.2
c_0	vacuum velocity of light	sec. 2.3.2
c	phase velocity of light in a medium	sec. 5.3
v	transport velocity of light in a medium	sec. 2.2
γ	bistatic coefficient	Eq. (2.34)
Γ	total vertex	Eq. (2.31)
	(all vertices depend on $\boldsymbol{r}_1 \ldots \boldsymbol{r}_4$.)	
U	irreducible vertex	sec. 2.3.2
R	reducible vertex	sec. 2.3.2
S	single scattering vertex	sec. 2.4
C	most-crossed vertex	sec. 2.4
L	ladder vertex	sec. 2.4
$\boldsymbol{\mathcal{C}}$	complementary vertex	sec. 4.5
	(generalized most-crossed)	
$\boldsymbol{\mathcal{R}}$	same as R	sec. 4.5
$\boldsymbol{\mathcal{S}}$	recurrent vertex	sec. 4.5
	(generalized single scattering)	
α	polarizability	sec. 1.1.1
$\epsilon(\boldsymbol{r})$	dielectric constant	Eq. (2.3.1)
$V(\boldsymbol{r})$	scattering potential	Eq. (1.10)
$E(\boldsymbol{r}, t)$	electric field	sec. 1.1.1
$I(\boldsymbol{r}, t)$	intensity	Eq. (1.4)
$W_{G,R,A}$	energy density (pump,probe,ASE)	sec. 1.2
$P(\boldsymbol{r}, t)$	electric polarization	Eq. (2.22)
$G(\boldsymbol{r}_1, \boldsymbol{r}_2)$	total amplitude Green's function	Eq. (2.16)
$G(\boldsymbol{r}_1 - \boldsymbol{r}_2)$	averaged total amplitude Green's function	sec. 2.3.1
$G_0(\boldsymbol{r}_1, \boldsymbol{r}_2)$	empty space amplitude Green's function	Eq. (2.12)
$F(\boldsymbol{r}_1, \boldsymbol{r}_2)$	intensity propagator	Eq. (2.3)
$t(\boldsymbol{r}_1, \boldsymbol{r}_2)$	single particle t-matrix	sec. 2.3.1
$\mathbf{T}^{(2)}(\boldsymbol{r}_1, \boldsymbol{r}_2)$	two particle t-matrix	Eq. (4.12)

Appendix B

Feynman notation

In this thesis the following drawing convention for Feynman scattering diagrams is used:

○	=	Scattering potential $-\alpha_0 k^2 \delta(\boldsymbol{r} - \boldsymbol{r}_i)$
×	=	Single particle t-matrix
———	=	Bare Green's function $G_0(\boldsymbol{r}_1, \boldsymbol{r}_2)$
═══	=	Dressed Green's function $G(\boldsymbol{r}_1, \boldsymbol{r}_2)$
·····	=	Connection between identical scatterers

Most of the work in this thesis is also published in:

Chapter 3:
D.S. Wiersma, M.P. van Albada, and A. Lagendijk, *An Accurate Technique to Record the Angular Distribution of Backscattered Light*, Rev. of Scient. Instr. **66**, November issue (1995).

D.S. Wiersma, M.P. van Albada, and A. Lagendijk, in *Advances in Optical Imaging and Photon Migration*, (Washington, 1994).

D.S. Wiersma, M.P. van Albada, and A. Lagendijk, *Precise Weak Localization Experiments in Random Structures*, in *Progress in Electromagnetic Research* (Kluwer, Dordrecht, 1994).

Chapter 4:

D.S. Wiersma, M.P. van Albada, B.A. van Tiggelen, and A. Lagendijk, *Experimental Evidence for Recurrent Multiple Scattering Events of Light in Disordered Media*, Phys. Rev. Lett. **74**, 4193 (1995).

B.A. van Tiggelen, D.S. Wiersma, and A. Lagendijk, *Self-consistent Theory for the Enhancement Factor in Coherent Backscattering*, Euro Phys. Lett. **30**, 1 (1995).

Chapter 5:
D.S. Wiersma, M.P. van Albada, and A. Lagendijk, *Random Laser?*, Nature **373**, 203 (1995)

D.S. Wiersma and A. Lagendijk, to be submitted to Phys. Rev. E. (1995).

Chapter 6:
D.S. Wiersma, M.P. van Albada, and A. Lagendijk, *Coherent Backscattering of Light from an Amplifying Random Medium*, Phys. Rev. Lett. **75**, 1739 (1995).

Summary

This thesis is concerned with the experimental and theoretical aspects of multiple scattering of light in both strongly scattering and amplifying random media. In chapter 2, an introduction to multiple light scattering theory is given. The theoretical concepts relevant for this thesis are explained and the backscattered intensity from a disordered medium with absorption is calculated explicitly. The bistatic coefficients describing coherent backscattering are presented in a form which allows for a comparison between the absorption case and the case of an amplifying random medium (treated in chapter 6).

In chapter 3, a new technique called 'off-centered rotation' is described to perform coherent backscattering experiments. This technique allows for recording the shape of the backscattering cone in a reliable and accurate way. The scanning range is about 500 mrad which includes exact backscattering, and the angular resolution is 50-100 μrad. This means the ratio between angular resolution and scanning range is of the order 1:10,000. We have used this technique to record backscattering cones from various samples in the weak scattering regime. It allowed us to record the theoretical enhancement factor of two in the helicity conserving polarization channel. The shape of the cone was compared with the theoretical expressions from diffusion theory and with the exact scalar solution. Very good agreement with diffusion theory was found for various measurements.

In chapter 4, light scattering from very strongly scattering samples is studied. By performing coherent backscattering experiments, experimental evidence is found for recurrent scattering of light waves. The availability of the technique of off-centered rotation allows for a determination of the enhancement factor versus the (scaled) scattering mean free path. We find an enhancement factor of 2.00 ± 0.01 in the weak scattering regime. At very strong scattering (i.e. for $k\ell_s < 10$), the enhancement factor is found to drop below 2.00. This deviation is interpreted as a manifestation of recurrent scattering. A calculation on the enhancement factor including recurrent scattering from two particles, confirms this interpretation.

In chapter 5, amplifying random media are discussed. We go into the experimental considerations on realizing such media. Different laser materials and excitation schemes are discussed and results on powdered ruby and Ti:sapphire crystals are given. We find that with powdered Ti:sapphire, amplifying random samples can be realized with transport mean free paths down to 20 μm and gain lengths of the order of 10 mm. We examine the theoretical aspects of amplifying random media by solving numerically the set of diffusion and rate equations describing light propagation in a powdered laser crystal. Under certain conditions, the spontaneously emitted light from such a medium is found to exhibit a pulsed behaviour. Finally, random laser action is discussed.

In chapter 6, experiments are described on amplifying random media. We have recorded laser speckle patterns from pumped Ti:sapphire powders. We find that upon increasing the gain the speckle pattern persists but changes. Furthermore, a study on coherent backscattering from an amplifying random medium is presented. We find that the central region of the backscattering cone narrows down upon increasing the gain, due to the increased importance of the longer light paths. The enhancement factor remains unchanged. Also a calculation is performed on coherent backscattering from an amplifying random medium in the diffusion approximation. Very good agreement between data and theory is found.

Samenvatting voor iedereen

Dit proefschrift gaat over licht in wanordelijke media. Een voorbeeld van een wanordelijk medium is dichte mist. Het licht van bijvoorbeeld de koplamp van een auto wordt in dichte mist diffuus: de lichtstralen die door de koplamp worden uitgezonden worden op een willekeurige manier van richting veranderd door de waterdruppels. Deze richtingsverandering noemen we verstrooiing. In dichte mist zal het licht vele malen verstrooid worden. Een ander voorbeeld van een wanordelijk medium is witte verf. Witte verf bestaat uit een willekeurige opeenstapeling van kleine korreltjes die, net als water druppels, het licht verstrooien.

Je kunt je afvragen hoe licht zich voortplant in een wanordelijk medium zoals mist. Als je op een kleine schaal kijkt, is dit een zeer ingewikkeld probleem: een afzonderlijke lichtstraal wordt vele malen van richting veranderd door de grote hoeveelheid waterdruppels. Op grote schaal lijkt het probleem echter heel simpel: het licht vormt gewoon een diffuse 'gloed'. Er is echter meer aan de hand. Omdat licht zich gedraagt als een golf kan er namelijk interferentie optreden. Wat is interferentie ?

Interferentie is een effect dat kan optreden voor elk soort golf, zoals licht, geluid, radiogolven of golven in het water, en ontstaat als twee of meer golven bij elkaar komen. Als er in een concertzaal (met een te droge akoestiek) op twee fluiten precies dezelfde toon gespeeld wordt, dan hangt wat je hoort af van waar je zit in de zaal. Hoe de geluidsgolven van de twee fluiten optellen, hangt namelijk af van hun onderlinge 'fase'. Als de beide golven net dezelfde beweging maken als ze elkaar tegen komen, werken ze samen en ontstaat er een sterkere beweging. De golven zijn dan 'in fase' en de interferentie is constructief. Het totale geluid dat je dan hoort is heel hard. Als ze daarentegen net een tegengestelde beweging maken heffen ze elkaar op. Ze zijn dan 'uit fase' met elkaar en de interferentie heet destructief. Je hoort in dat geval helemaal niets. Als je door de concertzaal loopt, kom je afwisselend op plaatsen waar de golven constructief optellen en waar ze elkaar uitdoven, en je hoort het geluid dus harder en zachter worden.

Interferentie kan ook optreden voor lichtgolven. Stel, we nemen een scherm met twee nauwe spleten erin, en belichten dat aan de achterkant met een zaklamp. De spleten zijn vergelijkbaar met de fluiten in het bovenstaande voorbeeld voor geluidsgolven. Beide spleten zullen aan de voorkant van het scherm lichtgolven uitzenden. Net als bij de fluiten zal op verschillende plaatsen het licht constructief of destructief interfereren. Als je het licht dat van de twee spleten afkomt op een wit stuk papier laat vallen, zie je lichte en donkere lijnen, corresponderend met de plaatsen waar de lichtgolven respectievelijk constructief optellen of elkaar opheffen. Bovendien, als je de spleten verder van elkaar brengt komen de lichte en donkere lijnen dichter bij elkaar en omgekeerd. Dit is een beroemd experiment dat voor het eerst uitgevoerd is door Thomas Young (1773–1829).

Interferentie van licht treedt ook op als het licht verstrooid wordt in bijvoorbeeld mist of witte verf. Een belangrijk voorbeeld daarvan is 'coherente terugverstrooiing'. Als we met bijvoorbeeld een halogeen spotje van een afstand schijnen op een wit geverfde muur, dan zal de witte verf het licht in alle richtingen verstrooien: vanaf iedere plaats in de kamer zie je een lichte plek op de muur. Als je echter precies op de plaats van het spotje zou kunnen gaan staan, zou je iets bijzonders zien. Voor het licht dat van de muur terug naar het halogeen spotje wordt verstrooid, treedt er namelijk constructieve interferentie op. In de richting terug naar het spotje (genoemd de 'terugstrooirichting'), wordt er meer licht verstrooid dan in alle andere richtingen. Waar komt dit effect vandaan ?

Laten we eens twee punten beschouwen in het belichte oppervlak van de verf. Er is licht dat op het ene punt invalt, en na een wanordelijke wandeling door de verf vanaf het andere punt weer naar buiten komt. Er is echter ook licht dat precies het omgekeerde doet. Als het licht in beide gevallen hetzelfde pad afgelegd heeft, is het als het naar buiten komt nog steeds in fase. De twee punten op het oppervlak kan je dan vergelijken met de twee spleten in het experiment van Young. Het licht dat van deze twee punten afkomt zal ook lichte en donkere strepen geven. Ieder stel punten in het belichte oppervlak van de verf geeft een dergelijk streeppatroon. Het totale verstrooide licht is dus de som van een heleboel streeppatronen, die variëren van heel fijn tot heel grof. Net als in het experiment van Young, wordt de afstand tussen de strepen in een patroon bepaald door de afstand tussen de twee punten in het belichte oppervlak, en de afstand tussen die twee punten hangt natuurlijk weer samen met de weg die het licht door het medium heeft gevolgd. Alle streeppatronen hebben echter één ding gemeen: in de richting terug naar het halogeen spotje vind je altijd een *lichte* streep. Daarom is de hoeveelheid licht die in die richting wordt verstrooid groter dan de hoeveelheid licht in andere richtingen. Om

coherente terugverstrooiing waar te nemen is lastig, omdat je de verstrooide hoeveelheid licht wilt meten op de plaats van de lichtbron (het spotje) en dicht daaromheen. Hoe je dat toch nauwkeurig kunt doen is beschreven in hoofdstuk 3.

Laten we het eens zwart-wit zien. Als licht op een voorwerp valt, kan het behalve verstrooid ook geabsorbeerd worden. Als al het licht geabsorbeerd wordt, is een voorwerp zwart. Als het gedeeltelijk geabsorbeerd en gedeeltelijk verstrooid wordt, dan is een voorwerp grijs. Als er helemaal geen absorptie optreedt, dan is een voorwerp perfect wit. In het dagelijks leven echter absorberen alle voorwerpen tenminste een klein beetje.

In dit proefschrift worden twee soorten wanordelijke media onderzocht. Het eerste is een medium dat verstrooit en waarin het omgekeerde van absorptie plaatsvindt: versterking. Wat gebeurt er als de hoeveelheid licht *meer* in plaats van minder wordt bij verstrooiing aan een voorwerp? Het voorwerp is dan pas echt wat men altijd met wasmiddelen claimt te bereiken: witter dan wit! In het eerste deel van hoofdstuk 5 wordt uitvoerig ingegaan op het maken van een dergelijk medium. Ik gebruik daartoe een kristal van het materiaal titaan-saffier dat ook gebruikt wordt voor een laser. Dergelijke kristallen zijn in staat om licht te versterken, hetgeen ook het principe is waar een laser op berust. Om dit kristal licht te laten versterken moet het eerst 'opgeladen' worden met een sterke lichtpuls. Als er daarna een tweede (zwakkere) puls op het verpoederde kristal valt, zal deze tweede puls zowel verstrooid als versterkt worden. Nadat het mogelijk was om een versterkend wanordelijk medium te maken, ben ik experimenten met dergelijke media gaan doen, waaronder metingen aan coherente terugverstrooiing. Deze metingen met de bijbehorende theorie staan beschreven in hoofdstuk 6.

Om meer inzicht te krijgen in het gedrag van versterkende wanordelijke media, heb ik numerieke berekeningen aan een dergelijk medium gedaan. Het is bijvoorbeeld interessant om te kijken wat er gebeurt als er in het opgeladen medium zoveel versterking plaatsvindt dat er per seconde meer licht ontstaat dan dat er weg kan stromen. Dan wordt de hoeveelheid licht zeer snel erg groot. Deze situatie kan echter niet onbeperkt blijven bestaan, en als het medium 'leeg' is neemt de hoeveelheid licht weer snel af. Dit proces kan zich een aantal malen herhalen als het medium steeds weer opnieuw opgeladen wordt, en het resultaat is dat het medium gepulst licht uitzendt. Dit staat beschreven in hoofdstuk 5. Aan het einde van dat hoofdstuk wordt ook besproken in hoeverre dit systeem gezien kan worden als een 'wanordelijke laser'.

Behalve versterkende media heb ik ook zeer sterk verstrooiende media bestudeerd. Een sterk verstrooiend medium is een medium waarin een licht-

straal zeer vaak achter elkaar verstrooid wordt. De lichtstraal kan zich dus steeds maar over zeer kleine afstanden vrij voortplanten voordat hij alweer van richting wordt veranderd. Die afstand waarover een lichtstraal zich gemiddeld vrij kan voortplanten in een medium, wordt de 'verstrooiings-vrijeweglengte' genoemd. De verstrooiings-vrijeweglengte geeft dus de mate aan waarin een medium verstrooit. Merk op dat een *kleine* verstrooiings-vrijeweglengte een *grote* mate van verstrooiing betekent.

Als nu een medium zo sterk verstrooit dat de verstrooiings-vrijeweglengte van dezelfde orde van grootte wordt als de golflengte van het licht, ontstaat er een vreemde situatie. Een lichtgolf kan zich dan niet eens meer vrij voortplanten over de afstand van één golflengte. In deze situatie zou er wat genoemd wordt 'Anderson lokalisatie' op kunnen treden. Dit is een interferentie-effect waarnaar al een tijd gezocht wordt. Door de zeer sterke verstrooiing zou al het licht langs gesloten paden ('lussen') gaan lopen en daarmee in het medium opgesloten (gelokaliseerd) zijn. Door coherente terugverstrooiing van een sterk verstrooiend medium te bestuderen, hebben we experimenteel bewijs gevonden dat er licht langs gesloten paden kan gaan lopen. Dit wordt beschreven in hoofdstuk 4.

Wat in de nabije toekomst interessant kan zijn, is de combinatie van zeer sterke verstrooiing met versterking. Ten gevolge van versterking worden lange paden in een medium belangrijker: hoe langer een pad, hoe groter de totale versterking langs het pad is. Door zeer sterke verstrooiing en versterking te combineren zou het effect van de gesloten paden misschien zo belangrijk kunnen worden dat Anderson lokalisatie van licht optreedt.

Dankwoord

Allereerst wil ik mijn promotor Ad Lagendijk heel hartelijk bedanken omdat hij me aan de ene kant een enorme vrijheid en vertrouwen gegeven heeft om mijn eigen weg te gaan, en aan de andere kant me daarbij altijd gesteund heeft als ik daarom vroeg. Om verder te komen in het onderzoek was alles mogelijk. Toen ik je om middernacht probeerde te bereiken omdat ik iets leuks gemeten had, belde je me 10 min. later vol interesse vanuit Parijs terug terwijl je volgens mij nog niet eens je jas uit had. Jouw enthousiasme voor de natuurkunde vind ik heel inspirerend. Een van de dingen die ik van je geleerd heb tijdens de vele uren waarin je met mij en Marco een aantal boeken hebt doorgenomen, is op welke mooie manier veel zaken in de natuurkunde samenhangen.

Ook mijn co-promotor Meint van Albada wil ik hartelijk bedanken. Ik heb veel geleerd van jouw kijk op een experiment waarbij je altijd de kern van de zaak naar boven wist te halen. Je vasthoudendheid en enthousiasme om problemen volledig te doorgronden heb ik altijd erg gewaardeerd. Verder sprak jouw werkwijze waarbij niet de glans maar wel de functionaliteit van de apparatuur de doorslaggevende factor tot aanschaf was mij erg aan. Ons uitstapje om een YAG-laser uit Orsay te halen vond ik dan ook heel leuk.

Erik-Jan Kossen wil ik bedanken voor alle technische steun. Je was altijd zeer betrokken bij de experimenten en bereid om snel problemen aan te pakken. Toen de voeding van de Argon laser was ontploft hebben we samen nog de hele avond transistors zitten solderen. Nogmaals bedankt daarvoor.

Ook Rob Kemper wil ik bedanken voor zijn technische steun. Als ik weer eens een raar component zocht, wist jij altijd wel ergens een laatje te vinden waarvan iedereen verder al lang vergeten was dat er het betreffende onderdeel in lag.

Daan Frenkel wil ik bedanken voor het gebruik van de computers in zijn groep en voor het niet boos worden toen er een 'automatische werker' een hele ochtend zijn bureau ingepikt had. Je inspirerende lezingen waren verder altijd voor mij het hoogtepunt van de colloquium cyclus op Amolf.

I would like to thank Thièry Lehoux and Yves Potiron of Quantel France in Paris, who helped me out when one of my YAG-rods had a burn. You stayed on a free afternoon, so I could come by with the laser oscillator before the holiday started.

Mijn moeder wil ik bedanken omdat ze me altijd gestimuleerd heeft om te gaan studeren en me daarbij ook steeds gesteund heeft. Wat het thuis vroeger ook erg leuk maakte was dat alles kon dat je creatief of leerzaam vond. De opgedane handigheid van alle hobbies is nu bij het experimenteren goed van pas gekomen.

Maarten Hagen wil ik bedanken voor het gebruik van zijn computer om de videocamera in mijn opstelling uit te lezen. Je hebt me ook goed geholpen bij het schrijven van de juiste acquisitie programma's.

Bart van Tiggelen wil ik bedanken voor de mooie berekeningen aan 'recurrent scattering' en voor alle discussies die we daarover hebben gevoerd. Ook bedankt voor de constructieve kritiek die je gegeven hebt op het theoretische gedeelte van hoofdstuk 4.

Bart Noordam heeft me goed geholpen met het bouwen van een gepulste dye laser. Ook bedankt voor het lenen van de juiste optica daarvoor. Verder wil ik Anton Buyzerd en Raluca Constantinescu bedanken voor hun Ti:saffier laserstaaf die ik mocht verpulveren.

Het Amolf is een inspirerende omgeving waar veel samengewerkt wordt, en iedereen altijd bereid is je te helpen of vragen te beantwoorden. Ik wil een aantal mensen met wie ik veel te maken heb gehad expliciet bedanken, namelijk: David van Coevoorden, Adriaan Tip, Rob Uiterlinden, Frans Vitalis, Saskia Windhouwer, Wim van der Zande, Piet Kea, Huib Bakker, Els Ruscaa-Steunebrink, Ilja Stavenuiter, Raluca Constantinescu, Trees zur Kleinsmiede-van Dongen, Marianne ter Stroot-Schouw, Maarten Hagen, Willem-Jan Huisman, Henk Dekker, Idsard Attema, Mischa Bonn, Marc-Paul de Boer, Klaas-Jan van Druten, Marcel Lankhuyzen, Ben v.d. Linden v.d. Heuvell, Harm Geert Muller, Rutger Vrijen, Eloy Wouters, en Mark Brongersma. De mensen van de groep van Jaap Boon wil ik verder bedanken voor het gebruik van het chemisch laboratorium, en hun assistentie bij het bereiden van mijn samples.

I wish to thank Lucia Mariotto for her loving care during the writing of part of my thesis in Verona. Your creative, enthusiastic, and curious way of living your life, is very inspiring. La tua presenza nella mia vita heeft een grote waarde voor mij.

Bart Broers wil ik bedanken voor alle gedreven discussies zowel over natuurkunde als over bijvoorbeeld biedsystemen. Jouw scherpe blik wist vaak de essentie van een probleem te raken. Ik heb bovendien erg genoten van de zomerschool met jou op Kreta, waar we bijna de hele natuurkunde gevat hebben in gitaarsnaren.

Edwin Brouwer van de firma Melles Griot wil ik bedanken voor het belangstellende meedenken met onze experimenten. Als ik weer eens iets 'eigenlijk de volgende dag nodig had', wist je altijd wel een manier te vinden om dat voor elkaar te krijgen.

John en Jaqueline wil ik bedanken voor alle vegetarische satés-meerhoek met rijst en een gekookt eitje. Het was heel fijn om af en toe bij jullie even 'op te laden'.

De UvA-groep was voor mij altijd een goede plek voor om met mensen te discussiëren over lichtverstrooiing en aanverwante zaken. Rik, Johannes, Mischa, Mark, Mark, Peter, Rudolf en Willem Bos, bedankt voor jullie enthousiasme en hulp. Mischa wil ik verder bedanken voor de samenwerking bij het zoeken naar diffusieconstantes met versterking.

Marina wil ik, ditmaal niet op haar eigen verzoek, heel erg bedanken voor met name alles. Op een indirecte manier heb je meer aan dit boekje bijgedragen dan je misschien zelf zou denken.

Christiaan Alofs wil ik bedanken voor zijn steun met name tijdens de laatste fase van het schrijven van mijn proefschrift. Je hulp als paranimf bij het regelen van alle zaken rondom mijn (en Marco's) promotie heb ik zeer gewaardeerd. Verder heb ik veel gehad aan je kritisch en helder commentaar op de één na laatste versie van mijn proefschrift.

Vorrei ringraziare Sandro Etalle per avermi convinto che fare parapendio di Domenica é molto bello. Molte grazie anche per avermi supportato in entrambe i nostri mondi.

Ondanks dat Bas Bijvoet bedankt wil worden voor verder helemaal niets, wil ik hem bedanken voor ondermeer het feit dat, ondanks zijn niet aflatende enthousiasme tijdens het experimenteren om de gehele opstellen te verbouwen, ik niet de optische tafel een kwart slag gedraaid terugvond bij terugkeer uit Italië, en desalniettemin hij daar leuke meetingen mee had gedaan en deed. Ook bedankt voor het kritisch lezen van en zeer bruikbaar commentaar leveren op mijn proefschrift.

Marco, zonder jou had mijn promotietijd er heel anders uitgezien. Ze

Druk: drukkerij Sigma B.V.
Lithografie: R & H grafipartners